

AD-A069 003

CASE WESTERN RESERVE UNIV CLEVELAND OHIO DEPT OF MET--ETC F/G 11/2
USE OF NUCLEARMICROANALYSIS. PART I. PROTON ACTIVATION STUDIES --ETC(U)
AUG 78 A R COOPER, A H HEUER, L D MAJOR F33615-74-C-4029

AFML -TR-78-119-PT-1

NL

UNCLASSIFIED

1 of 2
AD
A069003



AFML-TR-78-119

LEVEL *II*

Chw

AD A069003

USE OF NUCLEAR MICROANALYSIS

Part I — Proton Activation Studies of the Thermal Oxidation of Silicon

A. R. COOPER

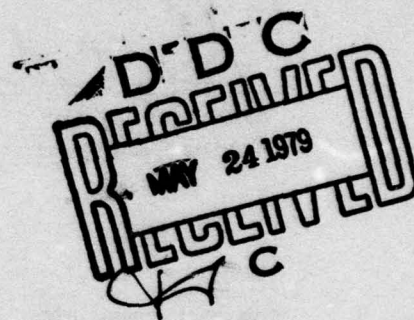
A. H. HEUER

L. D. MAJOR, Jr.

*CASE WESTERN RESERVE UNIVERSITY
CLEVELAND, OHIO 44106*

AUGUST 1978

**TECHNICAL REPORT AFML-TR-78-119, Part I
Final Report, October 1973 — June 1977**



DDC FILE COPY

Approved for public release; distribution unlimited.

**AIR FORCE MATERIALS LABORATORY
AIR FORCE WRIGHT AERONAUTICAL LABORATORIES
AIR FORCE SYSTEMS COMMAND
WRIGHT-PATTERSON AIR FORCE BASE, OHIO 45433**

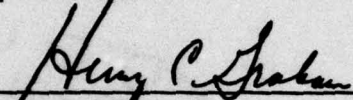
79 05 18 119

NOTICE

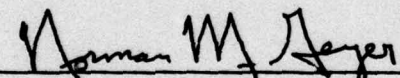
When Government drawings, specifications, or other data are used for any purpose other than in connection with a definitely related Government procurement operation, the United States Government thereby incurs no responsibility nor any obligation whatsoever; and the fact that the government may have formulated, furnished, or in any way supplied the said drawings, specifications, or other data is not to be regarded by implication or otherwise as in any manner licensing the holder or any other person or corporation, or conveying any rights or permission to manufacture, use, or sell any patented invention that may in any way be related thereto.

This report has been reviewed by the Information Office (IO) and is releasable to the National Technical Information Service (NTIS). At NTIS, it will be available to the general public, including foreign nations.

This technical report has been reviewed and is approved for publication.


HENRY C. GRAHAM
Project Engineer

FOR THE COMMANDER


NORMAN M. GEYER
Acting Chief
Processing & High Temperature Materials Branch
Metals and Ceramics Division

"If your address has changed, if you wish to be removed from our mailing list, or if the addressee is no longer employed by your organization please notify AFML/ILM, W-PAFB, OH 45433 to help us maintain a current mailing list".

Copies of this report should not be returned unless return is required by security considerations, contractual obligations, or notice on a specific document.

SECURITY CLASSIFICATION OF THIS PAGE (When Data Entered)

REPORT DOCUMENTATION PAGE		READ INSTRUCTIONS BEFORE COMPLETING FORM	
1. REPORT NUMBER (18) AFML TR-78-119	2. GOVT ACCESSION NO.	3. RECIPIENT'S CATALOG NUMBER	
4. TITLE (and Subtitle) (6) USE OF NUCLEAR MICROANALYSIS • PART I. PROTON ACTIVATION STUDIES OF THE THERMAL OXIDATION OF SILICON	5. TYPE OF REPORT & PERIOD COVERED (9) Final Report. 1 Oct 73-30 Jun 77		
6. AUTHOR(s) (10) A.R./Cooper, A.H./Heuer Leslie Dean /Major, Jr	8. CONTRACT OR GRANT NUMBER(s) (15) F33615-74-C-4p29 new		
7. PERFORMING ORGANIZATION NAME AND ADDRESS Case Western Reserve University Department of Metallurgy & Materials Sci. Cleveland, Ohio 44106	10. PROGRAM ELEMENT, PROJECT, TASK AREA & WORK UNIT NUMBERS (16) 23062302 (17) P3		
11. CONTROLLING OFFICE NAME AND ADDRESS Air Force Materials Laboratory (LLM) Air Force Wright Aeronautical Laboratories (AFSC) Wright-Patterson AF Base, Ohio 45433	13. NUMBER OF PAGES (11) Aug 1978 183		
14. MONITORING AGENCY NAME & ADDRESS (if different from Controlling Office) (12) 183A	15. SECURITY CLASS. (of this report) Unclassified		
16. DISTRIBUTION STATEMENT (of this Report) Approved for public release; distribution unlimited. 61102F			
17. DISTRIBUTION STATEMENT (of the abstract entered in Block 20, if different from Report)			
18. SUPPLEMENTARY NOTES			
19. KEY WORDS (Continue on reverse side if necessary and identify by block number) Silicon Silicon dioxide, amorphous Thermal Oxidation Oxygen Diffusion Proton Activation Mechanism of oxidation Exchange			
20. ABSTRACT (Continue on reverse side if necessary and identify by block number) The mechanism of the thermal oxidation of silicon in dry oxygen has been investigated using the direct observation of nuclear reactions. It has been found that the rate controlling process is the transport of molecular oxygen through the silica scale with exchange occurring between the permeating oxygen and the network oxygen.			

DD FORM 1 JAN 73 1473 EDITION OF 1 NOV 65 IS OBSOLETE

SECURITY CLASSIFICATION OF THIS PAGE (When Data Entered)

405 321 Gm

FOREWORD

This report describes part of the study conducted at Case Western Reserve University, Cleveland, Ohio under Contract F33615-74-C-4029.

The work reported herein was performed during the period 1 October 1973 to 30 June 1977. The contract monitor was Dr. Henry C. Graham, Acting Chief, Processing and High Temperature Materials Branch. The report is essentially the Masters Thesis of Leslie Dean Major, Jr.

The authors wish to thank Dr. Walter W. Lindstorm and Prof. Philip R. Bevington for their assistance.

This report is the first of two part series dealing with the application of nuclear microanalysis for studying oxidation and nitrogen diffusion.

ACCESSION for	
NTIS	Write Section <input checked="" type="checkbox"/>
DDC	Buff Section <input type="checkbox"/>
UNANNOUNCED	<input type="checkbox"/>
DISSEMINATION	
DISTRIBUTION/AVAILABILITY CODES	
SPECIAL	
A	

TABLE OF CONTENTS

SECTION	PAGE
I. Introduction	1
II. Literature Survey	3
2.1 Theories of Oxidation	3
2.1.1 Linear Oxidation Kinetics	3
2.1.2 Parabolic Oxidation Kinetics	3
2.1.3 Linear-Parabolic Oxidation Kinetics.	5
2.1.4 Wagner's Theory of High Tempera- ture Oxidation	12
2.1.5 Logarithmic Oxidation Kinetics	19
2.2 Silicon Oxidation Kinetics	21
2.3 Silicon Oxidation Mechanisms	24
2.4 Oxygen Diffusion in Fused Silica	33
2.5 Charged Particle Activation Analysis by Direct Nuclear Reactions	38
2.5.1 General	38

SECTION	TABLE OF CONTENTS (Continued)	PAGE
II.	2.5.2 Single-spectrum Proton Activation Analysis	
	Utilizing the $^{18}\text{O}(\text{p},\alpha)^{15}\text{N}$ Reaction	40
III	Mechanistic Models	46
	3.1 Introduction	46
	3.2 Oxidation Controlled by the Transport of Molecular Oxygen	50
	3.2.1 General	50
	3.2.2 Case I: The Rate of Permeation Much Greater than the Rate of Exchange	51
	3.2.3 Case II: Rate of Permeation Less than the Rate of Exchange	53
	3.2.4 Case III: Relative Rates of Permeation and Exchange are Intermediate to Cases I and II.	55
	3.3 Oxidation Controlled by the Transport of an Ionic Species	60
	3.3.1 Case IV: Ionic Transport of Oxygen	60
	3.3.2 Case V: Ionic Transport of Silicon	60
IV	Experimental Procedure	63
	4.1 Samples	63
	4.2 Thermal Oxidations	63
	4.2.1 Oxidation Apparatus and General Procedures	63
	4.2.2 Kinetic Oxidation Experiments	66
	4.2.3 Tracer Experiments	66
	4.3 Charged Particle Activation Analysis	67
	4.3.1 Sample Preparation and Positioning	67
	4.3.2 Alpha Particle Measurement and Recording	68
	4.3.3 The Activation Experiment	69
	4.3.4 Current Integrator Calibration	72

SECTION

TABLE OF CONTENTS (Continued)

PAGE

V	Data Analysis	74
	5.1 Current Integrator Calibration	74
	5.2 MCA Calibration	74
	5.2.1 Ta ₂ ¹⁸ O ₅ Calibration	74
	5.2.2 ZnF ₂ Calibration	75
	5.2.3 MCA Calibration Channel, MCA Dispersion, and Spreading Function	75
	5.2.4 Pulser Calibration	76
	5.3 Fitting the Alpha Spectra	76
	5.3.1 General	76
	5.3.2 Kinetic Oxidation Fits	79
	5.3.3 Mechanistic Oxidation Fits	80
VI	Results and Discussion	81
	6.1 Kinetic Experiments	81
	6.2 "Marker" Experiments	99
VII	Suggestions for Future Work	117
	7.1 Kinetic Oxidations	117
	7.2 Mechanistic Oxidations	117
	7.3 Experimental Procedure	118
	7.4 Data Reduction	118

APPENDIX

A	Range-Energy Curves for Protons and Alphas on Ta ₂ O ₅ , ZnF ₂ , and SiO ₂ and Kinematics of the ¹⁸ O(p,α) ¹⁵ N, ¹⁹ F(p,α) ¹⁶ O, and ¹⁹ F(p,α ₁) ¹⁶ O* Nuclear Reactions . .	119
---	--	-----

TABLE OF CONTENTS (Continued)

APPENDIX

PAGE

B Procedure used to fit Mechanistic Oxidation Samples.....	134
C Mechanistic Oxidation Alpha Spectra Fits.....	150
References.....	155
Bibliography.....	159

8.2.1 Data Calibration	75
8.2.2 MCA Calibration Channel, MCA Dispersion and Spreading Function	75
8.2.3 Pulse Calibration	75
8.2.4 Fitting the Alpha Spectra	75
8.2.5 General	75
8.2.6 Kinetic Oxidation Fits	75
8.2.7 Mechanistic Oxidation Fits	80
VI Results and Discussion	81
6.1 Kinetic Experiments	81
6.2 "Marker" Experiments	89
VII Suggestions for Future Work	117
7.1 Kinetic Oxidations	117
7.2 Mechanistic Oxidations	117
7.3 Experimental Procedure	118
7.4 Data Reduction	118

A Range-Energy Curves for Protons and Alphas on $^{18}O_2$, ^{18}O , and ^{16}O and Kinematics of the $^{18}O(p,\alpha)^{15}N$, $^{18}O(p,\alpha)^{15}N$, and $^{18}O(p,\alpha)^{15}N$ Nuclear Reactions. . . 119

LIST OF ILLUSTRATIONS

Figure		Page
1	The linear oxidation equation expressing oxide thickness, y , as a function of time, t	4
2	The parabolic oxidation equation expressing oxide thickness, y , as a function of time, t	6
3	The model for linear-parabolic oxidation kinetics...	7
4	The limiting cases for linear-parabolic oxidation...	10
5	The linear-parabolic oxidation equation and its two limiting forms.....	13
6	The logarithmic oxidation equation expressing the oxide thickness, y , as a function of time, t	20
7	The initial and final distributions of radio-antimony found by Atatta (18) at 1193°K.....	26
8	The fundamental infrared absorption bands of silica which show appreciable isotopic shift. Curve (1) is for a sample of Si^{18}O_2 , and curve (2) is for a sample of Si^{16}O_2	27
9	A schematic representation of Jorgensen's (13) modified marker experiment.....	29
10	A schematic arrangement showing the experimental arrangement used by Jorgensen for studying the effect of an electric field on the oxidation of silicon.....	31
11	Oxygen-18 diffusivities in fused silica.....	35
12	Depth-energy relationships in the experiments.....	43
13	Absolute cross section of $^{18}\text{O}(p,\alpha)^{15}\text{N}$ reaction as a function of incident energy ($\psi=165^\circ$).....	44

LIST OF ILLUSTRATIONS (Continued)

FIGURE		PAGE
14	Expected cation (M^*) and anion (X^*) tracer distributions in the scale under conditions (a) and (b), respectively, where the cation is the diffusing component. The corresponding distributions in situations where the anion is the mobile species are indicated by (c) and (d), respectively (50).....	48
15	Case I: The rate of permeation much greater than the rate of exchange.....	52
16	Case II: The rate of permeation less than the rate of exchange.....	54
17	Case III: The relative rates of permeation and exchange are intermediate to Cases I and II at various oxide thicknesses (a) $y=y_i$; (b) $y=1.25y_i$; (d) $y=1.75y_i$; (e) $y=2.0y_i$	56
18	Case IV: The ionic transport of oxygen.....	61
19	Case V: The ionic transport of silicon.....	62
20	Schematic diagram of the oxidation apparatus.....	64
21	Schematic of the scattering chamber and magnetic spectrometer.....	70
22	Schematic of electronic circuitry.....	71
23	Schematic used to calibrate the current integrator..	73
24	Graph used to calibrate MCA.....	77
25	Pulser calibration run.....	78
26	The measured silica scale thickness squared as a function of time at $1091 \pm 5^\circ\text{K}$	82
27	The measured silica scale thickness squared as a function of time at $1200 \pm 5^\circ\text{K}$	83
28	The measured silica scale thickness squared as a function of time at $1337 \pm 5^\circ\text{K}$	84
29	The measured silica scale thickness squared as a function of time at $1473 \pm 5^\circ\text{K}$	85
30	Graph of the parabolic rate constant as a function of reciprocal temperature.....	86

LIST OF ILLUSTRATIONS (Continued)

FIGURE		PAGE
31	Fit of sample S-10-1, 0.66 μ thick, at an incident proton energy of 750 KeV.....	90
32	The effect of changing the proton stopping power by $\pm 10\%$	93
33	The effect of changing the alpha stopping power by $\pm 10\%$	94
34	The effect of increasing both the proton and alpha stopping powers by 10%.....	95
35	The effect of increasing the proton stopping power by 10% while decreasing the alpha stopping power by 10%.....	96
36	The effect of decreasing both the proton and alpha stopping powers by 10%.....	97
37	The effect of decreasing the proton stopping power by 10% while increasing the alpha stopping power by 10%.....	98
38	Initial fit of sample S-5-3 at an incident proton energy of 750 KeV.....	101
39	Final fit of sample S-5-3 at an incident proton energy of 750 KeV.....	103
40	The experimental alpha spectrum for sample S-4-1 at an incident proton energy of 750 KeV.....	104
41	The experimental alpha spectrum for sample S-5-1 at an incident proton energy of 750 KeV.....	105
42	Concentration versus depth profile for sample S-4-1 oxidized at 1473 $\pm 5^\circ$ K.....	107
43	Concentration versus depth profile for sample S-4-2 oxidized at 1412 $\pm 5^\circ$ K.....	108
44	Concentration versus depth profile for sample S-4-3 oxidized at 1295 $\pm 5^\circ$ K.....	109
45	Concentration versus depth profile for sample S-4-4 oxidized at 1171 $\pm 5^\circ$ K.....	110

LIST OF ILLUSTRATIONS (Continued)

FIGURE

- B - 1 Assumed concentration profile 1 for sample S-5-3
- B - 2 Comparison of experimental data with predicted spectra using assumed concentration profile 1 for sample S-5-3 at 750 KeV
- B - 3 Comparison of experimental data with predicted spectra using assumed concentration profile 1 for sample S-5-3 at 800 KeV
- B - 4 Assumed concentration profile 2 for sample S-5-3
- B - 5 Comparison of experimental data with predicted spectra using assumed concentration profile 2 for sample S-5-3 at 750 KeV
- B - 6 Comparison of experimental data with predicted spectra using assumed concentration profile 2 for sample S-5-3 at 800 KeV
- B - 7 Assumed concentration profile 3 for sample S-5-3
- B - 8 Comparison of experimental data with predicted spectra using assumed concentration profile 3 for sample S-5-3 at 750 KeV
- B - 9 Comparison of experimental data with predicted spectra using assumed concentration profile 3 for sample S-5-3 at 800 KeV
- B - 10 Assumed concentration profile 4 for sample S-5-3
- B - 11 Comparison of experimental data with predicted spectra using assumed concentration profile 4 for sample S-5-3 at 750 KeV
- B - 12 Comparison of experimental data with predicted spectra using assumed concentration profile 4 for sample S-5-3 at 800 KeV
- B - 13 Assumed concentration profile 5 for sample S-5-3
- B - 14 Comparison of experimental data with predicted spectra using assumed concentration profile 5 for sample S-5-3 at 750 KeV
- B - 15 Comparison of experimental data with predicted spectra using assumed concentration profile 5 for sample S-5-3 at 800 KeV

LIST OF ILLUSTRATIONS (Continued)

FIGURE

- | | |
|----------------|---|
| C ₁ | Fit of Sample S-4-1 at an incident proton energy of 750 KeV |
| C ₂ | Fit of Sample S-4-1 at an incident proton energy of 800 KeV |
| C ₃ | Fit of Sample S-5-1 at an incident proton energy of 750 KeV |
| C ₄ | Fit of Sample S-5-1 at an incident proton energy of 800 KeV |

LIST OF TABLES

TABLE		PAGE
1	The Linear and Parabolic rate constant expressed as a function of water content in the ambient and orientation according to Irene.....	22
2	Oxygen-18 Diffusivities in fused silica	34
3	Q values for nuclear reactions induced by protons and deuterons on some light isotopes.....	39
4	Correlation of the measured thickness and the estimated thickness, using the color chart given by Pliskin and Conrad.....	88
A-1	Range-Energy Curve for Protons on Ta ₂ O ₅ ..	120
A-2	Range-Energy Curve for Alphas on Ta ₂ O ₅ ...	121-122
A-3	Kinematics of the ¹⁸ O(p,α) ¹⁵ N reaction...	123
A-4	Range-Energy Curve for Protons on ZnF ₂ ...	124
A-5	Range-Energy Curve for Alphas on ZnF ₂	125-126
A-6	Kinematics of the ¹⁹ F(p,α) ¹⁶ O reaction...	127
A-7	Kinematics of the ¹⁹ F(p,α ₁) ¹⁶ O* reaction.	128
A-8	Range-Energy Curve for Protons on SiO ₂ ...	129-130
A-9	Range-Energy Curve for Alphas on SiO ₂	131-133

LIST OF SYMBOLS

SYMBOL	MEANING	PAGE FIRST USED
a_i	Activity of species i	16
A	$2D(\frac{1}{k_s} + \frac{1}{K})$	11
B	$\frac{2DC_e}{N_1}$	11
c_{eq}	$c_1 z_1 = c_2 z_2 $	17
c_i	Concentration of species i	14
C	Concentration	8
C'	Interstitial solubility of oxygen in silica	37
C''	Concentration of oxygen incorporated in the silica	37
C_e	Concentration of oxygen in the bulk gas	7
C_i	Concentration of oxygen in the oxide at the metal-oxide interface	7
C_o	Concentration of oxygen in the oxide at the oxide-gas interface	7

LIST OF SYMBOLS (Continued)

SYMBOL	MEANING	PAGE FIRST USED
$C(x_i)$	Concentration in oxygen-18 fraction at x_i	42
d	Deuteron	39
D	Diffusivity	8
D_{eff}	Effective diffusivity	37
e	Electronic charge	14
eV	Electron Volt	21
$E_p(x)$	Proton energy at depth x	41
$E_p(0)$	Proton energy at surface	41
$E_\alpha(x,x)$	Energy of alpha created by proton of $E_p(x)$ at a depth x	41
$E_\alpha(x,0)$	Energy of alpha created by proton of $E_p(x)$ at surface	42
i	Channel number	42
J	Flux of oxygen	5
k	Boltzmann's Constant	18
k_p	Parabolic rate constant	5
k_r	Rational rate constant	17

LIST OF SYMBOLS (Cont'd)

SYMBOL	MEANING	PAGE FIRST USED
k_s	Chemical reaction rate constant	8
k_L	Linear rate constant	3
K	Surface-exchange coefficient	8
K_1	Exchange coefficient	51
KeV	Kiloelectron volts	44
L	Volume number density of oxygen atoms	42
M_N	Mass of a nitrogen-15 nucleus	41
M_p	Mass of a proton	41
M_α	Mass of an alpha particle	41
MCA	Multichannel Analyzer	69
MeV	Megaelectron volts	39
\dot{n}_{eq}	Number of equivalents per area per second	14
\dot{n}_i	Number of moles per area per second	14
N_i	Number of counts in channel i in undistorted spectra	42

LIST OF SYMBOLS (Cont'd)

SYMBOL	MEANING	PAGE FIRST USED
$[N_i]$	Number of counts in channel i in distorted spectra	45
N_0	Avogadro's Number	14
N_1	Number of oxygen per unit volume of oxide	9
p	Proton	39
P	Pressure	50
$P(E_i, E_j)$	Probability function that an alpha particle which under ideal conditions would be recorded in channel i will be recorded in channel j	45
Q	Energy equivalence of the mass difference between reactant and product nuclei	38
Q^*	Activation energy	34
Q_{obs}	Observed charge	74
Q_{true}	True charge collected	74
R	Gas constant	16
S	Solubility	50
t	Time	3
t_i	Transference number of species i	14

LIST OF SYMBOLS (Cont'd)

SYMBOL	MEANING	PAGE FIRST USED
T	Temperature	16
v_i	Drift velocity of species i	14
x	Depth from sample surface	41
x_i	Mean depth	42
y	Oxide thickness	3
y_i	Initial oxide thickness	11
z_i	Valence of species i	14
Z	Atomic number	38
a	Area	14
Γ	Integrated proton flux	42
α	Alpha particle	39
β_i	Mobility of species i	8
Δx_i	Depth interval with mean depth x_i	42
$\Delta\Omega$	Solid angle of observation	42
κ	Electrical conductivity	14

LIST OF SYMBOLS (Cont'd)

SYMBOL	MEANING	PAGE FIRST USED
λ	Wave length	27
μ_i	Chemical potential of species i	8
$\sigma(x_i)$	Differential cross section at x_i	42
τ	$\frac{y_i^2 + Ay_i}{B}$	11
ϕ	Local electrical potential	14
χ^2	Chi square	79
χ_r^2	Reduced chi square	79
ψ	Laboratory angle of detection	41

SUMMARY

Both the kinetics and the mechanism of the thermal oxidation of silicon in "dry" oxygen have been investigated utilizing the $^{18}\text{O}(p,\alpha)^{15}\text{N}$ nuclear reaction. The oxygen-18 concentration profiles were determined by a trial and error deconvolution procedure of the recorded alpha spectra.

The kinetic measurements indicate that in the temperature range investigated, 1089^{+5}K to 1473^{+5}K , the parabolic rate constant could be expressed as

$$k_p = [(7.5^{+3.0}) \times 10^{-10} \exp - (\frac{1.08^{+0.09}\text{eV}}{kT})] \frac{\text{cm}^2}{\text{sec}}$$

It was found that there was good agreement between the silica scale thickness as measured by the single spectrum proton activation technique and the estimated scale thickness using interference colors.

The rate controlling process in the thermal oxidation of silicon in the temperature range 1171^{+5}K to 1473^{+5}K was determined by successive isotopic oxidation studies to be the transport of molecular oxygen through the adherent silica scale. The exchange process between the permeating oxygen and the network oxygen previously reported by Ligenza and Spitzer was confirmed. It was found that the kinetics of the exchange and permeation processes have different temperature dependences and that the kinetics of the two processes are approximately

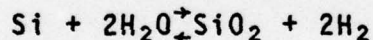
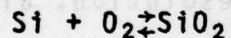
equal at 1325°K. At temperatures in excess of 1325°K the exchange kinetics exceed the permeation kinetics.

The combined results of the kinetic and mechanistic studies confirm the theory set forth by Meek to explain the diffusion of oxygen in vitreous silica. It was found that the diffusivity governing the transport of molecular oxygen through thermally formed silica, as calculated from the parabolic rate constant, was in agreement with the diffusivity measured by Norton in his permeation experiment. It was also possible to calculate an approximate diffusivity based on the decrease in oxygen-18 content of the silica scales during the isotopic oxidation experiments. The calculated isotopic diffusivity was found to be approximately equal to the diffusivity measured by Williams in his exchange experiments.

SECTION I

INTRODUCTION

The mechanism of the thermal oxidation of silicon is of general scientific interest and of specific interest to both the planar device industry and the glass industry. The formation of a thin layer of silicon dioxide on silicon wafers is of importance in the masking and surface passivation of planar silicon devices. These oxide layers can be formed by various methods, for example deposition by a vapor-phase reaction, electro-chemical oxidation (anodization), plasma reaction, or thermal oxidation by one of the following reactions:



In industrial applications silicon dioxide layers are most frequently formed by thermal oxidation.

The glass industry is interested in the mechanism of the thermal oxidation of silicon in the hope that it will lead to an understanding of the diffusion

of oxygen fused silica. An understanding of oxygen diffusion in fused silica can lead to a better understanding of many physical properties such as optical absorption, viscosity, and electrical conductivity. In this study it will be shown that the thermal oxidation of silicon is governed by the diffusion of molecular oxygen through the silica scale.

Because the adherent oxide scales formed on silicon are very thin, traditional tools for studying oxidation processes, such as weight gain, inert markers, and optical microscopy, are difficult to apply. Ellipsometry has proven to be effective in making kinetic measurements, but is not effective in determining reaction mechanisms. A modification of the single spectrum proton activation technique (1), originally developed at Case Western Reserve University to study oxygen diffusion in oxide ceramics, was used. This technique, because of its sub-micron resolution, allows determination of both the kinetics and mechanism of the reaction.

SECTION II

LITERATURE SURVEY

2.1 Theories of Oxidation

2.1.1 Linear Oxidation Kinetics

Linear oxidation kinetics hold when the rate of oxidation is constant, or

$$\frac{dy}{dt} = k_L \quad (1)$$

$$y = k_L t + \text{constant}$$

where k_L is the linear rate constant, y is the scale thickness and t is time. See Figure 1. An example (2) of systems exhibiting this type of kinetics is when the oxidizing environment can reach the metal surface through cracks or pores in the oxide coating.

2.1.2 Parabolic Oxidation Kinetics

If the oxide scale formed is protective, a diffusion process through the scale will control the oxidation kinetics and parabolic behavior will be observed. Here the rate of scale formation will be inversely proportional to the scale thickness.

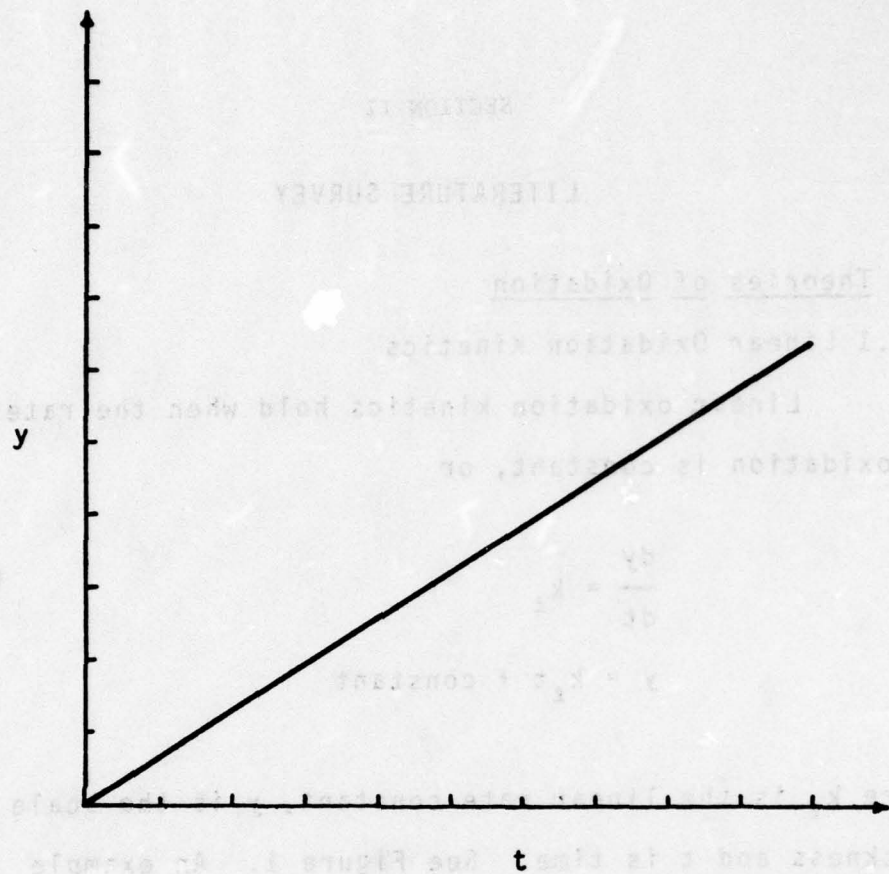


Figure 1. The linear oxidation equation expressing oxide thickness, y , as a function of time, t .

$$\frac{dy}{dt} = \frac{k_p}{y} \quad (2)$$

$$y^2 = 2k_p t + \text{constant}$$

See Figure 2.

2.1.3 Linear-Parabolic Oxidation Kinetics

The linear-parabolic oxidation kinetics are derived here for the case where the oxidation reaction takes place at the metal-oxide interface (3,4). A similar derivation could be presented for the case where metal diffuses through the scale and the reaction takes place at the oxide-gas interface.

If oxidation is to occur, the incoming oxygen must undergo three processes, which are illustrated in Figure 3. These steps are:

- 1) The transport of the oxygen from the bulk gas to the oxide-gas interface.
- 2) The diffusion of the oxygen as an ion, atom, or molecule across the existing oxide layer.
- 3) The reaction of the oxygen with the metal at the metal-oxide interface.

The fluxes J_1 , J_2 , and J_3 correspond to the three processes in the oxidation process and can be expressed as follows. The flux of oxygen from the bulk gas to the oxide-gas interface, J_1 , is given by:

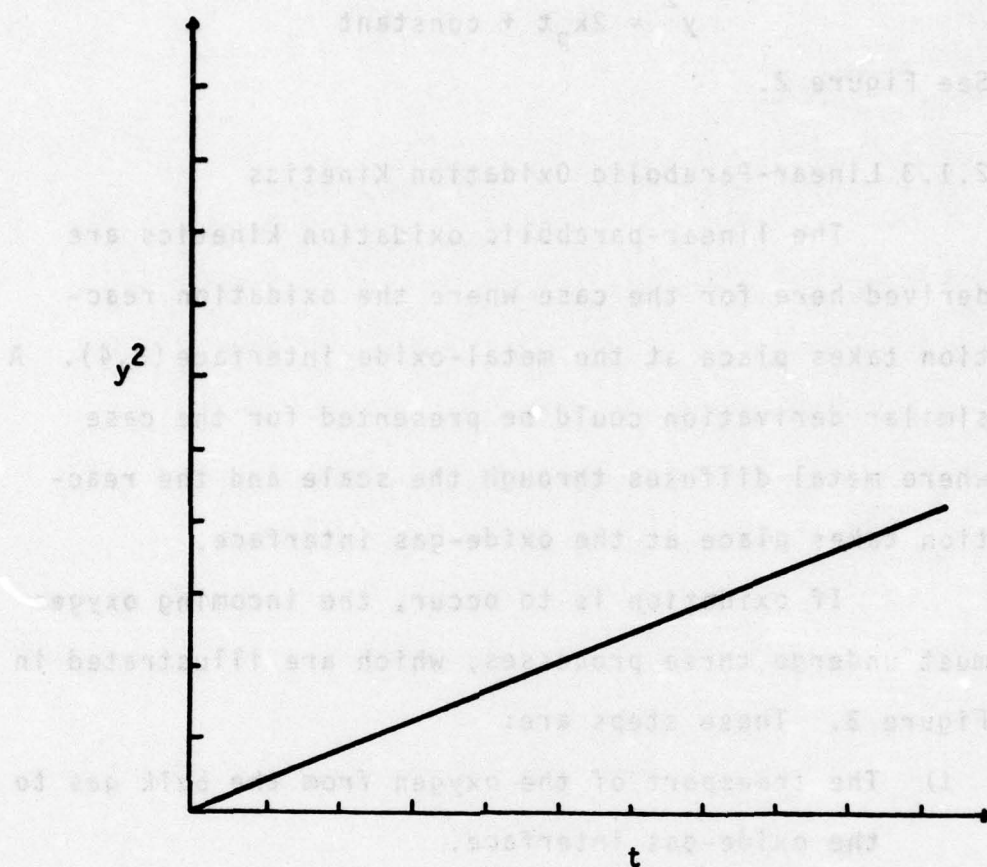


Figure 2. The parabolic oxidation equation expressing oxide thickness, y , as a function of time.

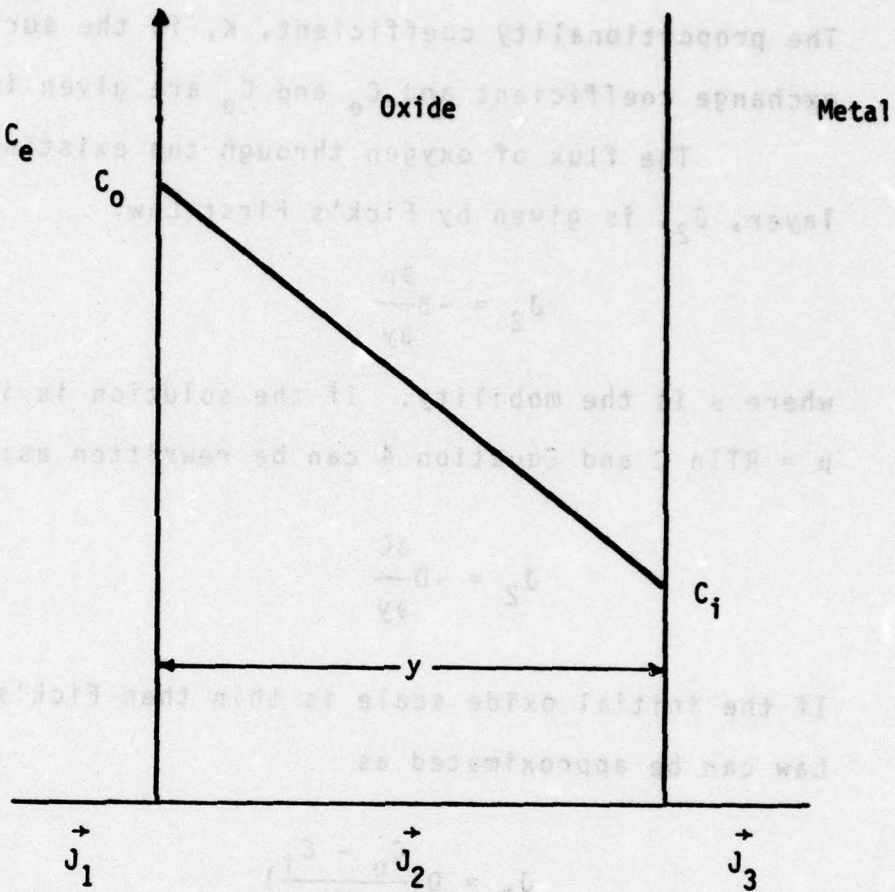


Figure 3. The model for linear-parabolic oxidation kinetics.

$$J_1 = K(C_e - C_o) \quad (3)$$

The proportionality coefficient, K , is the surface-exchange coefficient and C_e and C_o are given in Figure 3.

The flux of oxygen through the existing oxide layer, J_2 , is given by Fick's First Law:

$$J_2 = -\beta \frac{\partial \mu}{\partial y} \quad (4)$$

where β is the mobility. If the solution is ideal then $\mu = RT \ln C$ and Equation 4 can be rewritten as:

$$J_2 = -D \frac{\partial C}{\partial y} \quad (5)$$

If the initial oxide scale is thin then Fick's First Law can be approximated as

$$J_2 = D \left(\frac{C_o - C_i}{y} \right) \quad (6)$$

The flux corresponding to the reaction at the metal-oxide interface, J_3 , is equal to the reaction rate constant, k_s , times the concentration of oxygen at the interface:

$$J_3 = k_s C_i \quad (7)$$

By definition of steady state, $J_1 = J_2 = J_3 = J$,

it is possible to solve for the two interfacial concentrations of oxygen:

$$C_i = \frac{C_e}{1 + \frac{k_s}{K} + \frac{k_s y}{D}} \quad (8)$$

and

$$C_o = \frac{(1 + \frac{k_s y}{D}) C_e}{1 + \frac{k_s}{K} + \frac{k_s y}{D}} \quad (9)$$

As D becomes small the limiting forms of Equations 8 and 9 are $C_i \rightarrow 0$ and $C_o \rightarrow C_e$ and the oxidation is diffusion controlled. In the other limit as D becomes large $C_i = C_o = C_e / (1 + k_s/K)$ and the oxidation process is reaction controlled. These two limits are shown schematically in Figure 4.

The rate of oxide growth is given by $N_1 \frac{dy}{dt}$, where N_1 is the number of oxygen molecules incorporated in a unit volume of oxide.

At steady state

$$N_1 \frac{dy}{dt} = J = \frac{k_s C_e}{1 + \frac{k_s}{K} + \frac{k_s y}{D}} \quad (10)$$

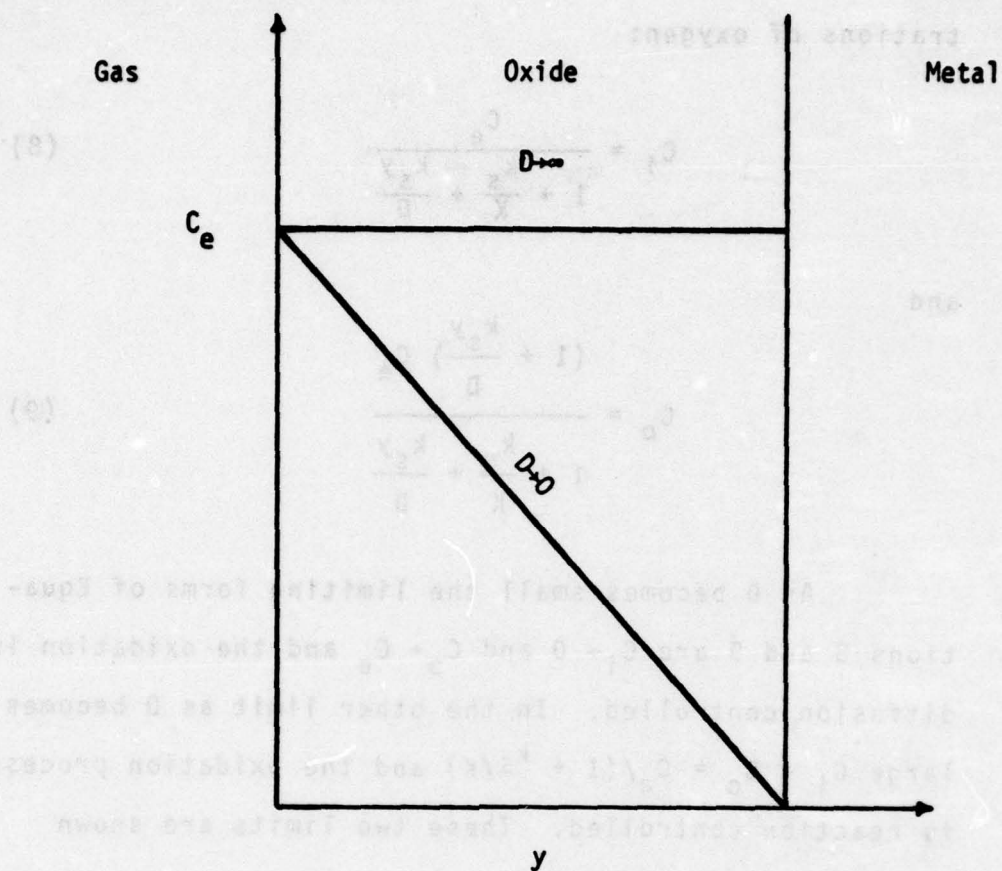


Figure 4: The limiting cases for linear-parabolic oxidation.

Applying the boundary condition that $y(0) = y_1$, where y_1 is the initial oxide thickness, and solving the differential equation the following is obtained

$$y^2 + Ay = B(t + \tau) \quad (11)$$

where

$$A = 2D \left(\frac{1}{k_s} + \frac{1}{K} \right) \quad (12a)$$

$$B = \frac{2DC_e}{N_1} \quad (12b)$$

and

$$\tau = \left(\frac{y_1^2 + Ay_1}{B} \right) \quad (12c)$$

Solving for the oxide thickness as a function of time yields

$$y = \frac{A}{2} \left\{ 1 + \left(\frac{t + \tau}{A^2/4B} \right) \right\}^{1/2} - \frac{A}{2} \quad (13)$$

Equation 11 reduces to linear oxidation kinetics at very short times, i.e., $(t + \tau) \ll A^2/4B$. The linear rate constant k_p is given by

$$k_l = \frac{B}{A} = \frac{k_s K C_e}{(k_s + K) N_1} \quad (14)$$

For long times, i.e., $t \gg A^2/4B$, Equation 11 reduces to parabolic oxidation kinetics with the parabolic rate constant being given by

$$k_p = B = \frac{2DC_e}{N_1} \quad (15)$$

Figure 5 shows a plot of the linear-parabolic oxidation kinetics.

2.1.4 Wagner's Theory of High Temperature Oxidation

Carl Wagner developed a theory of high temperature oxidation (5-9) in which the oxidation process is diffusion controlled, therefore leading to parabolic kinetics. Wagner assumes that positively charged metal ions, negatively charged nonmetal ions, and electrons are the only mobile species in the oxide and that the diffusion of neutral species can be neglected. If this is the case there are two limiting cases: (1) metal ions and electrons diffuse from the metal-oxide interface to the oxide-gas interface and (2) electrons diffuse from the metal-oxide interface to the oxide-gas interface while nonmetal ions diffuse in the opposite direction. If the diffusion of each the various species is independent of the others their drift velocity can be expressed as

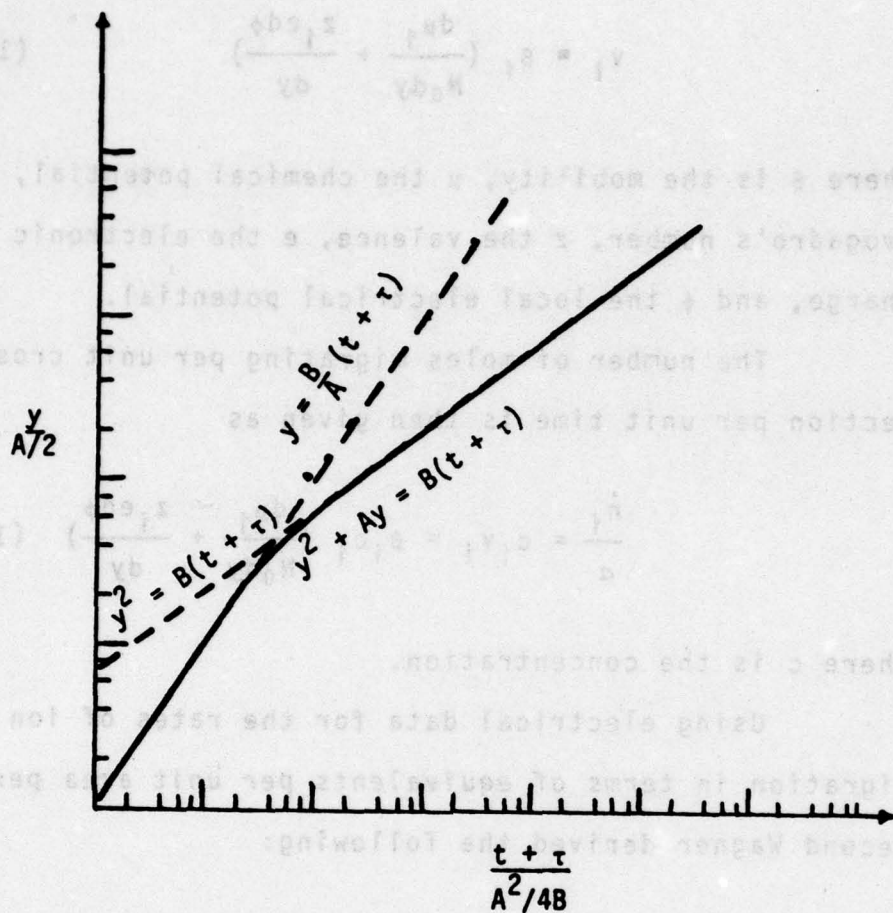


Figure 5: The linear-parabolic oxidation equation and its two limiting forms.

$$v_i = \beta_i \left(\frac{d\mu_i}{N_0 dy} + \frac{z_i e d\phi}{dy} \right) \quad (16)$$

where β is the mobility, μ the chemical potential, N_0 Avogadro's number, z the valence, e the electronic charge, and ϕ the local electrical potential.

The number of moles migrating per unit cross section per unit time is then given as

$$\frac{\dot{n}_i}{a} = c_i v_i = \beta_i c_i \left(\frac{d\mu_i}{N_0 dy} + \frac{z_i e d\phi}{dy} \right) \quad (17)$$

where c is the concentration.

Using electrical data for the rates of ion migration in terms of equivalents per unit area per second Wagner derived the following:

$$\frac{\dot{n}_{eq}}{a} = \left[\left(\frac{300}{96500} \right) N_0 e \frac{\mu_y''}{\mu_y'} \left(\frac{1}{|z_2|} \right) (t_1 + t_2) t_3 \kappa d \mu_y \right] \left(\frac{1}{a \Delta y} \right) \quad (18)$$

Here μ is the chemical potential of the nonmetal, μ_y' , the chemical potential of the nonmetal at the metal-oxide interface, μ_y'' , the chemical potential of the nonmetal at the oxide-gas interface, t the transference number, κ the electrical conductivity, a the area, and the subscripts 1, 2, and 3 refer to the metal

ions, nonmetal ions and electrons respectively. The part of Equation 18 in square braces can be set equal to the rational rate constant, k_r , for the oxidation reaction.

Assuming the transference number for electrons, t_3 , is approximately unity and using the definition of a transference number and Equation 17, one can solve for the electrical potential gradient:

$$\frac{d\phi}{dy} = \frac{d\mu_3}{N_0 e dy} \quad (19)$$

By combining Equation 17 and 19 it is now possible to solve for the number of moles of ions migrating per unit area per unit time:

$$\frac{\dot{n}_1}{\alpha} = \left(- \frac{\beta_1 C_1}{N_0} \right) \left(\frac{d\mu_1}{dy} + \frac{z_1 d\mu_3}{dy} \right) \quad (20a)$$

$$\frac{\dot{n}_2}{\alpha} = \left(- \frac{\beta_2 C_2}{N_0} \right) \left(\frac{d\mu_2}{dy} + \frac{z_2 d\mu_3}{dy} \right) \quad (20b)$$

If chemical equilibrium is to be maintained in the system then

$$\mu_M = \mu_1 + z_1 \mu_3 \quad (21a)$$

$$\mu_0 = \mu_2 + z_2 \mu_3 \quad (21b)$$

where the subscripts M and O refer to neutral metal and oxygen atoms respectively. By definition of the chemical potential in terms of activities, a ,

$$d\mu_M = RTd(\ln a_M) \quad (22a)$$

$$d\mu_O = RTd(\ln a_O) \quad (22b)$$

Combining Einstein's Equation relating mobility and the diffusivity of a species with Equations 20 and 21 the following are obtained:

$$\frac{\dot{n}_1}{a} = -D_1 c_1 \left(\frac{d \ln a_M}{dy} \right) \quad (23a)$$

$$\frac{\dot{n}_2}{a} = -D_2 c_2 \left(\frac{d \ln a_O}{dy} \right) \quad (23b)$$

If the oxide is stoichiometric the sum of the diffusivities will be essentially the same for all y 's. If Equations 23a and 23b are multiplied by $z_i dy$, added, and integrated over the thickness of the oxide the following is obtained:

$$\left(\frac{z_1 \dot{n}_1}{a} + \frac{z_2 \dot{n}_2}{a} \right) \Delta y = -z_1 c_1 \int_{a_M''}^{a_M'} D_1 d \ln a_M + |z_2| c_2 \int_{a_O''}^{a_O'} D_2 d \ln a_O \quad (24)$$

The activities can be related by

$$|z_2| d\ln a_M + z_1 d\ln a_O = 0 \quad (25)$$

and the rational rate constant expressed as either

$$k_r = c_{eq} \frac{a_O''}{a_O'} \left(\frac{z_1 D_1}{|z_2|} + D_2 \right) d\ln a_O \quad (26a)$$

or

$$k_r = c_{eq} \frac{a_M''}{a_M'} \left(D_1 + \frac{|z_2| D_2}{z_1} \right) d\ln a_M \quad (26b)$$

where $c_{eq} = c_1 z_1 = c_2 |z_2|$.

If the oxide is nonstoichiometric deviations can occur in four different ways. Excess metal can be accounted for by either cation interstitials and free electrons or anion vacancies and free electrons. A metal deficit can be accounted for by either cation vacancies and electron holes or anion interstitials and electron holes.

For the case of excess metal ions the rational rate constant can be expressed as

$$k_r = (1 + z_1) c_{eq} D_1' \left(1 - \frac{c_1(i)''}{c_1(i)'} \right) \quad (27)$$

where the subscript (i) refers to the interstitial

position and $D_1' = \left(\frac{c_1'(i)}{c_1} \right) \beta_1(i) kT$.

If there is a metal deficit, the rational rate constant is

$$k_r = (1 + z_1) c_{eq} D_1'' \left[1 - \left(\frac{p_{O_2}'}{p_{O_2}''} \right)^{1/8} \right] \quad (28)$$

where $D_1'' = \left(\frac{c_1''(i)}{c_1} \right) \beta_1(v) kT$ and the subscript (v) refers to vacant sites.

For the case of excess oxygen ions the rational rate constant is

$$k_r = (1 + |z_2|) c_{eq} D_2' \left[1 - \left(\frac{p_{O_2}'}{p_{O_2}''} \right)^{1/3} \right] \quad (29)$$

where $D_2' = \left(\frac{c_2''(i)}{c_2} \right) \beta_2(i) kT$.

In the case of an oxygen deficit the rational rate constant can be expressed as

$$k_r = (1 + |z_2|) c_{eq} D_2'' \left[1 - \left(\frac{p_{O_2}''}{p_{O_2}'} \right)^{1/6} \right] \quad (30)$$

$$\text{where } D_2'' = \left(\frac{c_2'(v)}{c_2} \right) \beta_2(v) kT.$$

2.1.5 Logarithmic Oxidation Kinetics

The logarithmic rate law can be stated as follows

$$\frac{1}{y} = Y - Z \log t \quad (31)$$

where Y and Z are related to the oxidizing pressure, the oxidizing temperature, a characteristic distance dependent on the contact potential difference (work function), and temperature, and a limiting thickness. See Figure 6.

Oxidation kinetics of this type are observed for many metals at low temperatures (e.g. aluminum at room temperature). A possible mechanism for this type of kinetics has been set forth by Cabrera and Mott (10-12). It is assumed that oxygen atoms are adsorbed on the surface of the oxide, which produces vacant energy levels for electrons. Electrons can now pass through the oxide layer from the metal to the oxygen atoms by either thermionic emission or tunnelling, to equalize the surface state levels and the Fermi energy of the metal. The electrons will then combine with the oxygen atoms at the surface, setting up a potential dif-

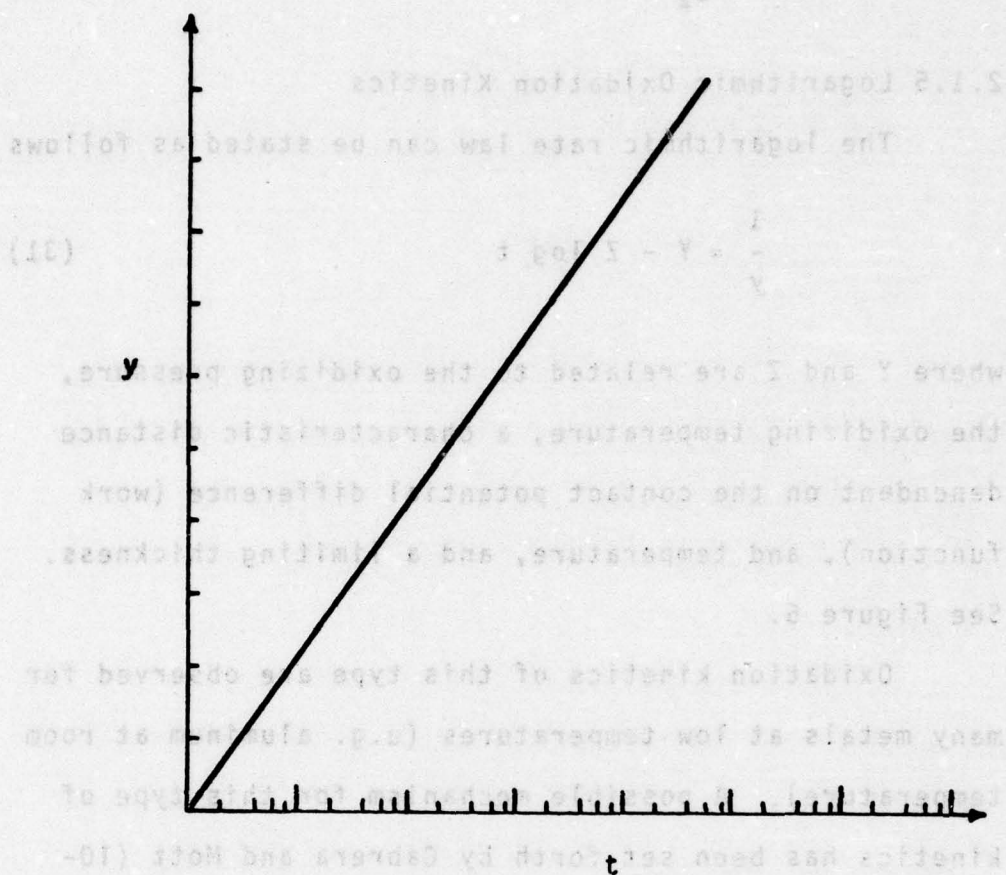


Figure 6: The logarithmic oxidation equation expressing the oxide thickness, y , as a function of time, t .

ference across the oxide on the order of one volt. It is then argued that this field will be strong enough to alter the activation barrier for diffusion of ions and charged defects.

2.2 Silicon Oxidation Kinetics

The kinetics of the thermal oxidation of silicon in dry oxygen obeys a linear-parabolic rate law (3,4, 13-17) with the initial linear portion corresponding to a thickness of approximately 230 Å (3,4).

The activation energy for the linear portion of the thermal oxidation reaction is 1.98 ± 0.02 eV (3,4, 17). However, there is a large discrepancy in the reported activation energy for the parabolic portion of the reaction. The experimentally determined activation energies for this portion of the reaction fall in two ranges, 1.27 ± 0.06 eV (3,4,14-16) and 1.80 ± 0.10 eV (17-19). The writer can see no correlation between the activation energy determined and any of the experimental parameters (e.g. temperature range, pressure range, crystal orientation, or type of oxidation).

It has been observed by Irene (17) that both the linear and parabolic rate constants increase with increasing water content in the ambient gas. See Table 1.

TABLE 1
THE LINEAR AND PARABOLIC RATE CONSTANT
EXPRESSED AS A FUNCTION OF WATER
IN THE AMBIENT AND ORIENTATION ACCORDING
TO IRENE (17)

TEMPER- ATURE (°C)	ORIEN TATION	H ₂ O in O ₂ (PPM)	k _l (A/min)	STAN DARD DEVI ATION	(A ² /k _p min)	STAN DARD DEVI ATION
800	(100)	<1	0.67	0.04	310	30
		~25	0.83	0.02	430	20
	(110)	<1	1.3	0.10	480	50
		~25	1.3	0.03	800	40
	(111)	<1	1.4	0.05	690	20
		~25	1.3	0.03	1,200	60
927	(100)	<1	5.3	0.20	2,700	100
		~25	5.3	0.30	4,300	260
	(110)	<1	11	0.90	3,600	150
		~25	8.3	0.60	5,300	250
	(111)	<1	8.9	0.20	5,300	110
		~25	9.7	0.60	6,900	290
996	(100)	<1	16	0.80	7,700	240
		~25	13	1.0	12,000	890
	(110)	<1	29	3.4	9,400	360
		~25	28	0.80	12,000	210
	(111)	<1	26	2.0	11,000	370
		~25	28	0.80	13,000	230

It has been reported by Deal (15) and Irene (17) that there is an orientation effect on the thermal oxidation of silicon. It can be seen from Irene's (17) data in Table 1 that the dependence of the linear rate constant on orientation is

$$(110) \geq (111) > (100)$$

Irene's rationalization of this is that the order and the magnitude of the rate constants are in agreement with the number of silicon to silicon bonds in each of these planes.

Irene (17) also reports that there is an orientation dependence of the parabolic rate constant which is

$$(111) > (110) \geq (100)$$

To date this dependence has not been explained since the orientation of the silicon should not effect the diffusion of oxygen through the silica scale forming on the surface of the crystal.

It has been reported by Deal (15) that the kinetics of thermal oxidation of silicon is independent of impurity type (phosphorus or boron dopants) and also of impurity concentration in the range of 0.001 to 50 ohm-centimeter. He also found that the properties of the oxide formed were independent of both impurity type and concentration.

2.3 Silicon Oxidation Mechanisms

Because of the parabolic behavior of the thermal oxidation of silicon it is generally agreed that the reaction, at least at long times and high temperatures, is controlled by the diffusion of either silicon ions, oxygen ions, oxygen atoms, or oxygen molecules (electron diffusion is not considered here because of the corresponding high transport number) through the silica scale. If we look at the activation energy of the parabolic portion of the rate constant, we find agreement between the activation energy of 1.27 electron volts (3,4,14-16) and the activation energy for oxygen diffusion in fused silica determined by Williams (20) and Norton (21) (See Section 2.4). This agreement indicates the possibility that the thermal oxidation of silicon is controlled by oxygen diffusion assuming these are the correct activation energies for oxidation and diffusion.

Studies of the oxygen partial pressure dependence of the thermal oxidation reaction have shown the linear rate constant to be pressure independent. It has been reported by Atalla (18) that the parabolic rate constant varies as the partial pressure of oxygen to the four-fifths power; however, Ligenza and Spitzer (22)

and Deal and Grove (4) reported the parabolic rate constant to be directly proportional to the oxygen partial pressure. This dependence is the same as that found for oxygen diffusion in fused silica (21) and indicates that transport occurs by the diffusion of neutral oxygen molecules.

Further confirmation that thermal oxidation occurs by the transport of oxygen rather than silicon was presented by Atalla (18). Silicon samples were partially oxidized and then a layer of radioactive antimony evaporated on the thermal silica scale. The oxidation was then continued and the samples analyzed for antimony. The radioactive antimony was found at the oxide-gas interface (See Figure 7) indicating oxygen diffusion to be the rate controlling process in the thermal oxidation of silicon.

Further confirmation that the oxidation reaction occurs at the silicon-silica interface was provided by the experiments of Ligenza and Spitzer (22). In their experiments silicon coupons were oxidized successively in oxygen-16 and oxygen-18 and the isotopic shift determined by the fundamental infrared absorption bands of silica which show appreciable isotopic shift. See Figure 8.

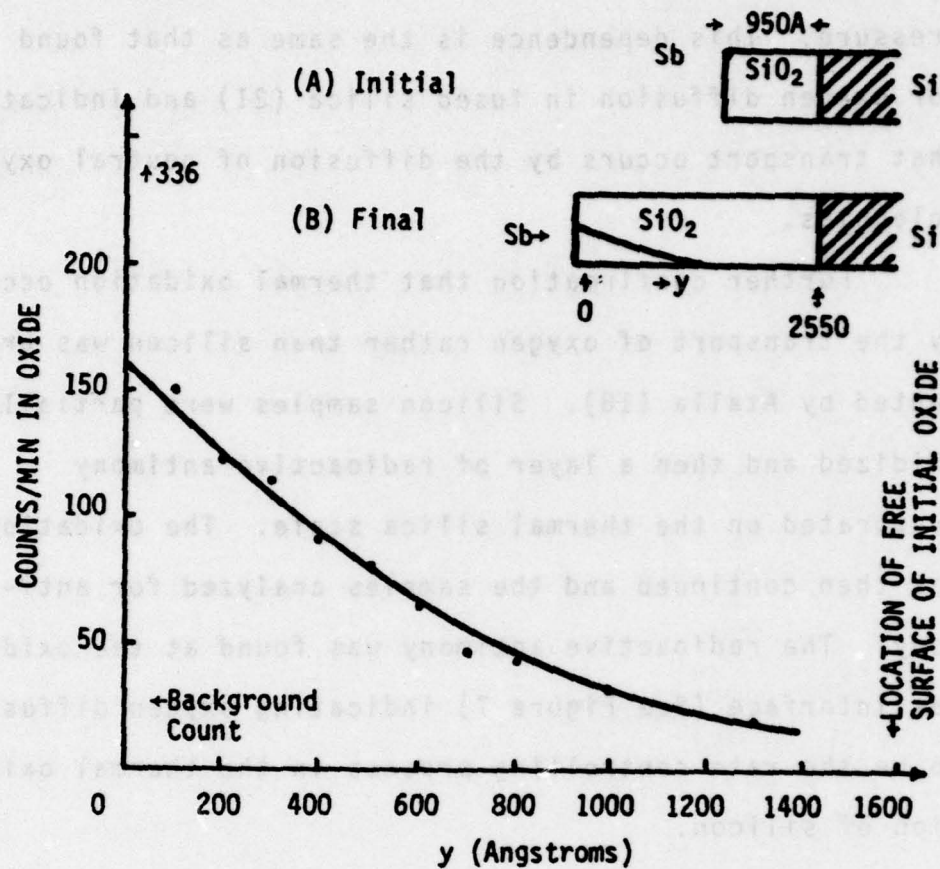


Figure 7: The initial and final distributions of radio-antimony found by Atatta (18) at 1193°K.

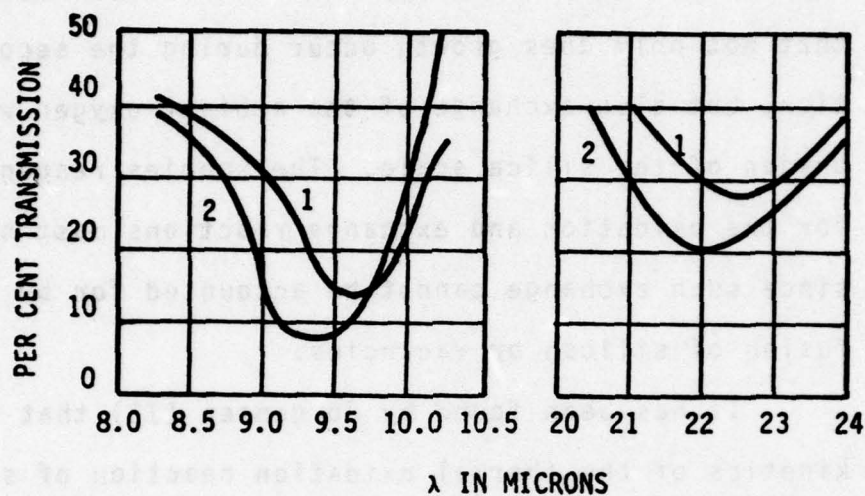


Figure 8: The fundamental infrared absorption bands of silica which show appreciable isotopic shift. Curve (1) is for a sample of Si^{18}O_2 , and curve (2) is for a sample of Si^{16}O_2 .

Ligenza and Spitzer found that if they oxidized a silicon coupon in oxygen-16 and then continued the oxidation in oxygen-18, almost the entire oxide scale was composed of oxygen-18. If the isotopic order was reversed, they found the silica to be almost entirely oxygen-16. It becomes apparent from these results that not only does growth occur during the second oxidation, but also exchange of the ambient oxygen with the oxygen of the silica scale. The species responsible for the oxidation and exchange reactions must be oxygen since such exchange cannot be accounted for by the diffusion of silicon or vacancies.

It has been found by Jorgensen (13) that the kinetics of the thermal oxidation reaction of silicon was controlled by the migration of an oxygen species and the kinetics could be effected by the application of an electric field. Jorgensen first performed a modified marker experiment in which he sputtered a thin strip of platinum onto a silicon wafer. A layer of silicon monoxide was evaporated on top of the silicon and platinum and then oxidized to silicon dioxide. (See Figure 9 for schematic of sample) The entire assemblage was then oxidized and the platinum marker located. It was found that the platinum was not located at the silicon-silica interface, implying that oxidation occurs by the migration of oxygen.

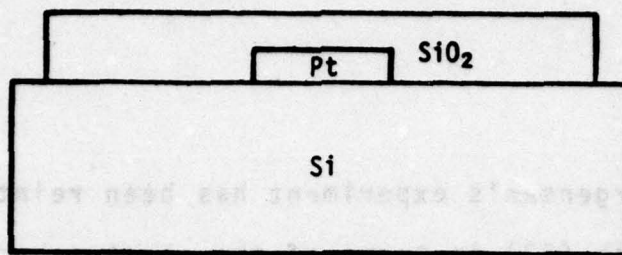


Figure 9. A schematic representation of Jorgensen's (13) modified marker experiment.

In a second experiment Jorgensen concluded that the rate controlling species in the oxidation reaction was oxygen ions. If the kinetics are controlled by the diffusion of a charged species then it should be possible to influence the reaction rate by the application of an electric field, while if a neutral species were migrating an electric field should have no effect on the kinetics. Jorgensen found that if he made the oxide-gas interface negative with respect to the metaloxide interface the reaction rate was increased, while if he made the oxide-gas interface positive with respect to the metaloxide interface he could either retard or completely stop the oxidation.

Jorgensen's experiment has been reinterpreted by Raleigh (23) in terms of the electrochemistry of the process. A schematic of the apparatus used in Jorgensen's experiment is shown in Figure 10. A porous platinum electrode was attached to each end of a partially oxidized single crystal of silicon and the assembly heated in an oxygen atmosphere. The rate of silica growth at each end of the sample was the monitored in the presence of an electric field (approximately 10^4 volts per centimeter across the silica) and in the absence of an electric field. Raleigh argues that the external application of an electric field by itself cannot provide a steady-state driving force for the oxidation reaction. This is because in any diffusion-controlled oxidation, the net process is required to be the transport of an electroneutral species (this does not rule out the transport of ions as long as charge neutrality is maintained) through the growing oxide scale.

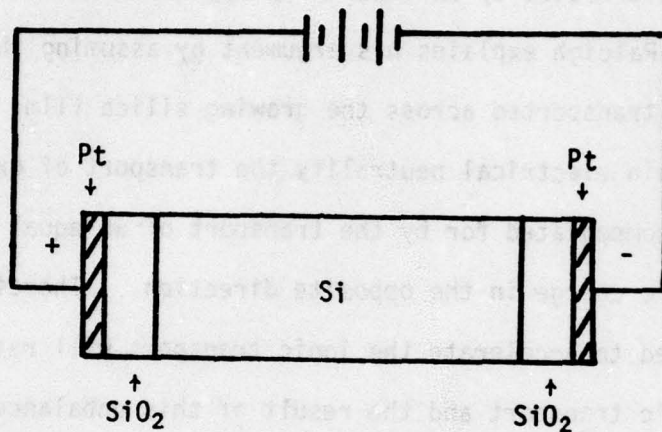


Figure 10. A schematic arrangement showing the experimental arrangement used by Jorgensen for studying the effect of an electric field on the oxidation of silicon.

He also argues that oxygen diffusion is the result of a chemical potential gradient which is fixed on both sides of the film and cannot be effected by an externally applied electric field.

Raleigh explains his argument by assuming that oxygen ions are transported across the growing silica film. In order to maintain electrical neutrality the transport of oxygen ions must be compensated for by the transport of an equal amount of electronic charge in the opposite direction. Therefore the field used to accelerate the ionic transport will retard the electronic transport and the result of this unbalanced transport will be the transport of unbalanced charge. In the steady-state the uncompensated charge will set up a field equal and opposite to the applied field which will tend to cancel it and return the system to the field state.

Raleigh concludes that the reason Jorgensen could influence the oxidation rate by the application of an electric field was in the use of a battery to apply the electric field. The battery circuit provided an external circuit for electronic flow, oxygen ion transport then required only ionic conductivity, allowing what may have been only a minor transport mechanism because of a low electronic conductivity to assume a major significance. This in essence set up an electrolysis cell.

2.4 Oxygen Diffusion in Fused Silica

There is a large variation in the diffusivities of oxygen reported in the literature (20, 21, 24, 25). The reported values of the pre-exponential term vary over seven orders of magnitude and the reported activation energies range from 1.17 electron volts per atom to 3.07 electron volts per atom. See Table 2 and Figure 11.

The two most commonly quoted values for oxygen diffusion in silica are those given by Williams (20):

$$D = 2.0 \times 10^{-9} \exp\left(-\frac{1.26}{kT}\right) \quad (32)$$

and Norton (21):

$$D = 2.88 \times 10^{-4} \exp\left(-\frac{1.17}{kT}\right) \quad (33)$$

TABLE 2. --Oxygen-18 diffusivities in fused silica.

Investigator	Temperature Range (°K)	D (cm ² /sec)	Q* (kcal/mole)
1. Hau1, Dumbgen	1173-1523	4.3×10^{-6}	56
2. Norton	1173-1373	2.88×10^{-4}	27
3. Sucov	1198-1498	1.5×10^{-2}	71
4. Williams	1123-1523	2.0×10^{-9}	29

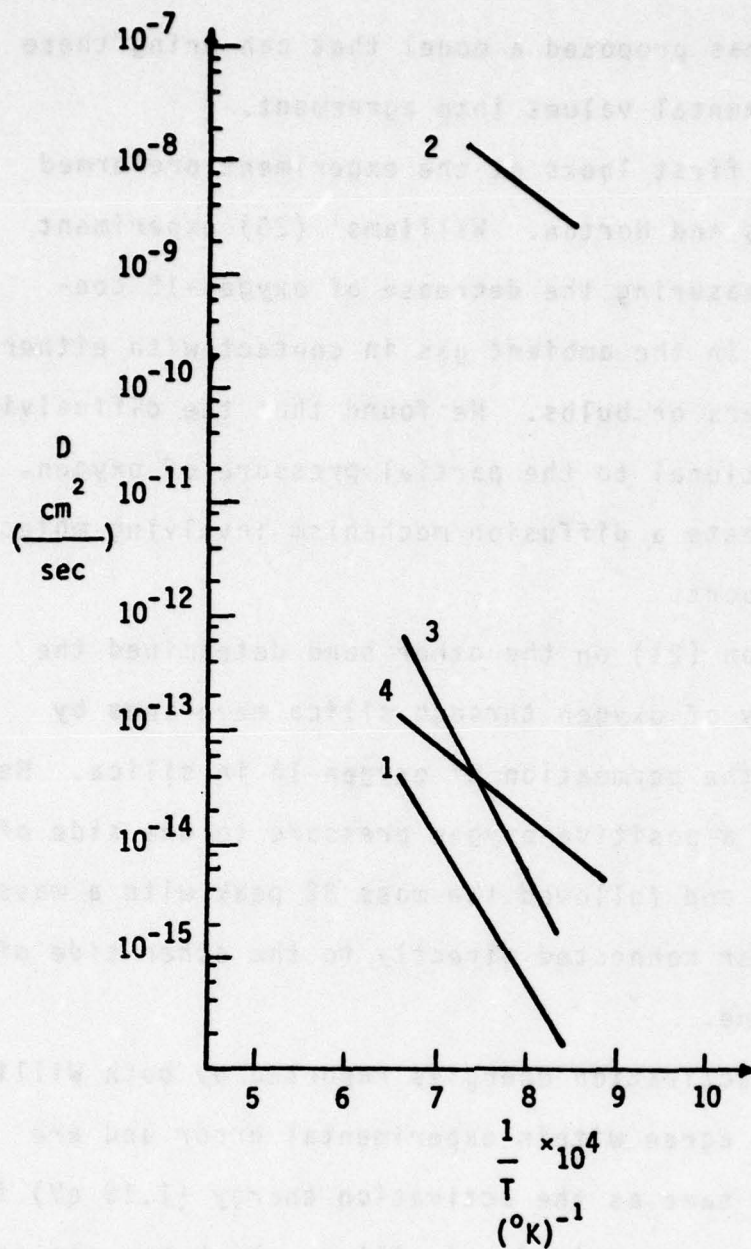


Figure 11: Oxygen-18 diffusivities in fused silica.

Meek (26) has proposed a model that can bring these two experimental values into agreement.

Meek first looks at the experiment performed by Williams and Norton. Williams' (20) experiment involved measuring the decrease of oxygen-18 concentration in the ambient gas in contact with either silica fibers or bulbs. He found that the diffusivity was proportional to the partial pressure of oxygen, which suggests a diffusion mechanism involving molecular transport.

Norton (21) on the other hand determined the diffusivity of oxygen through silica membranes by measuring the permeation of oxygen-16 in silica. Here he applied a positive oxygen pressure to one side of a membrane and followed the mass 32 peak with a mass spectrometer connected directly to the other side of the membrane.

The activation energies reported by both Williams and Norton agree within experimental error and are nearly the same as the activation energy (1.15 eV) for diffusion of argon in fused silica, which has the same size as an oxygen molecule (27). The result leads one to believe that the diffusing species are neutral oxygen molecules which pass through interstices in the silica network.

Meek feels that the tracer diffusivity as measured by an exchange experiment, such as Williams performed, is actually the diffusivity times the fraction of time the tracer is incorporated in the diffusing species, providing the exchange reaction is rapid and diffusion is the rate limiting process. The diffusivity as measured by Williams is then an effective diffusivity, D_{eff} , which is given by

$$D_{\text{eff}} = D \left(\frac{C'}{C'' + C'} \right) \quad (34)$$

or

$$D = D_{\text{eff}} \left(\frac{C'' + C'}{C'} \right) \quad (35)$$

where C' is the interstitial solubility of oxygen in silica and C'' is the concentration of oxygen incorporated in the silica. Equations 34 and 35 assume that diffusion is the rate limiting step and exchange between the diffusing oxygen and the network oxygen is rapid. This exchange reaction can also be used to explain the results previously reported by Hutchison (28) and Ligenza and Spitzer (22).

2.5 Charged Particle Activation Analysis by Direct Nuclear Reactions

2.5.1 General

The identification of light elements ($Z \leq 18$), which have been introduced in samples as tracers, impurities, and dopants, is easily accomplished by inducing nuclear reactions by charged particles (protons and deuterons). This type of analysis has been finding increasing use in the past ten years to study diffusion (1, 29-34), oxidation (35), electrochemical phenomena (36-39), etc. These procedures have the following properties (40):

- (a) Nuclear microanalysis is restricted to the first few microns of the sample.
- (b) With most of the reactions there is no natural background.
- (c) Most of the reactions have a high Q value¹ (see Table 3) which allows the use of low energy particles, thus reducing local heating of the target, and avoiding competing nuclear reaction (See (d)).
- (d) Coulomb barriers prevent the reaction of most nuclei larger than chlorine with the low energy particles

¹ The Q value of a reaction is the energy equivalent of the mass difference between the reactant and product nuclei.

TABLE 3. --Q values for nuclear reactions induced by protons and deuterons on some light isotopes.

Isotope	Q ₀ (MeV)	Isotope	Q ₀ (MeV)	Isotope	Q ₀ (MeV)
(p,α) reactions:					
⁷ Li	17.347	⁶ Li	4.02	⁹ Be	2.125
¹¹ B	8.582	¹⁰ B	3.970	³¹ P	1.917
¹⁹ F	8.119	³⁷ Cl	3.030	²⁷ Al	1.594
¹⁵ N	4.964	²³ Na	2.379	¹⁷ O	1.197
				¹⁰ B	1.147
(d,α) reactions:					
¹⁰ B	17.819	¹¹ B	8.022	³² S	4.890
⁶ Li	22.36	¹⁵ N	7.693	¹⁸ O	4.237
⁷ Li	14.163	⁹ Be	7.152	³⁰ Si	3.121
¹⁴ N(α ₀)	13.579	²⁵ Mg	7.047	¹⁶ O	3.116
¹⁹ F	10.038	²³ Na	6.909	²⁶ Mg	2.909
¹⁷ O	9.812	²⁷ Al	6.701	²⁴ Mg	1.964
¹⁴ N(α ₁)	9.146	²⁹ Si	6.012	²⁸ Si	1.421
³¹ P	8.170	¹³ C	5.167	¹² C	<0
(d,p) reactions:					
¹⁰ B	9.237	¹⁷ O	5.842	²⁶ Mg	4.212
²⁵ Mg	8.873	²⁷ Al	5.499	¹² C	2.719
¹⁴ N(p ₀)	8.615	²⁴ Mg	5.106	¹⁶ O	1.919
²⁹ Si	8.390	⁶ Li	5.027	¹⁸ O	1.731
³² S	6.418	²³ Na	4.734	¹⁴ N(p _s)	1.305
²⁸ Si	6.253	⁹ Be	4.585	¹¹ B	1.138
¹³ C	5.947	¹⁹ F	4.379	¹⁵ N	0.267
³¹ P	5.712	³⁰ Si	4.367	⁷ Li	<0

employed. This allows the determination of light elements in heavy substrates.

- (e) The nuclear reactions employed are very specific, in that two isotopes, even of the same element, react quite differently.
- (f) The results obtained are independent of the matrix in which the observed isotope is embedded, since the physical or chemical state of the nuclei does not effect the reaction yield.
- (g) The results are quantitative.
- (h) The method is essentially nondestructive.
- (i) The sensitivity is high in that as little as 10^{-12} grams of matter per square centimeter can be determined under ideal conditions.
- (j) Concentration versus depth relationships to tens of microns can be determined with sub-micron resolution by one of three methods:
 - (1) serial sectioning (30, 31, 34, 35), (2) resonance techniques (32, 41-44), and (3) single spectrum method (1, 30, 31, 35, 40).

2.5.2 Single-spectrum Proton Activation Analysis Utilizing the $^{18}\text{O}(p,\alpha)^{15}\text{N}$ Reaction (1,44)

If a solid containing a concentration gradient of

oxygen-18 is irradiated with a monoenergetic beam of protons and the energetic alpha particles simultaneously detected, it is a straightforward process to convert the alpha spectrum to a concentration versus depth profile. Since the $^{18}\text{O}(p,\alpha)^{15}\text{N}$ reaction is exoergic with a Q value of 3.98 MeV (see Table 3), each energetic alpha particle emitted can be associated with a given depth in the sample. A proton incident upon a sample with energy $E_p(0)$ will lose energy almost linearly as it traverses the sample and therefore at a depth x from the sample surface will have an energy $E_p(x)$. At some depth, x , the proton will react with an oxygen-18 nucleus producing an energetic alpha particle of energy $E_\alpha(x,x)$ which depends on $E_p(x)$ in the following way (45):

$$E_\alpha(x,x) = \left[\frac{(M_p M_\alpha E_p(x))^{1/2}}{M_\alpha + M_N} \cos \psi \pm \left\{ \frac{M_p M_\alpha E_p(x)}{(M_\alpha + M_N)^2} \cos^2 \psi + \frac{M_N Q + E_p(x)(M_N - M_p)}{M_\alpha + M_N} \right\}^{1/2} \right]^2 \quad (36)$$

Here M_p is the mass of a proton, M_α the mass of an alpha particle, M_N the mass of the residual nitrogen-15 nucleus, and ψ the laboratory angle of detection. The alpha par-

ticle will also be attenuated as it travels out of the sample and at the sample surface will have energy $E(x,0)$. As can be seen from Figure 12, there will be a one-to-one correlation between alpha energy and depth, if one knows the stopping power of the sample for protons and alphas, and a concentration versus depth profile is determined from the number of alpha particles of each energy detected. The number of counts in a given channel², N_i , where i refers to the channel number, is given by

$$N_i = L \lambda C(x_i) \sigma(x_i) \Delta x_i \Delta \Omega \quad (37)$$

Here L is the volume number density of oxygen atoms in the sample, λ the integrated proton flux, $C(x_i)$ the concentration in oxygen-18 fraction at mean depth x_i , $\sigma(x_i)$ the differential cross section at mean depth x_i (see Figure 13 for $\sigma(E_p)$), Δx_i the depth interval with mean depth x_i , and $\Delta \Omega$ is the solid angle of observation.

The number of counts determined by Equation 37 holds only for an ideal spectrum where there is no distortion. In actuality the spectrum recorded will be

². A channel is a segment of the multi-channel analyzer which records and stores the number of alpha particles detected in a given energy interval.

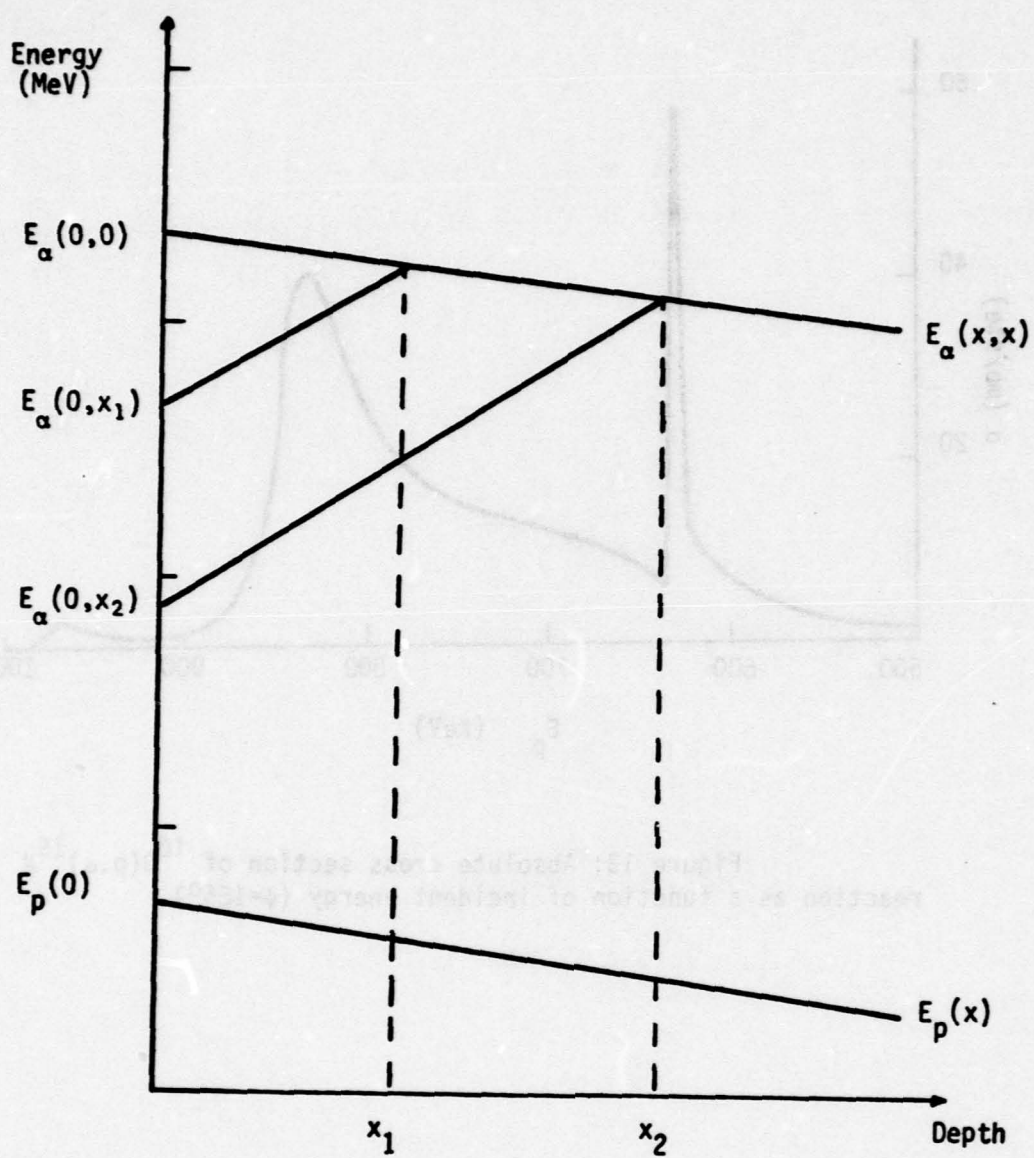


Figure 12: Depth-energy relationships in the experiments.

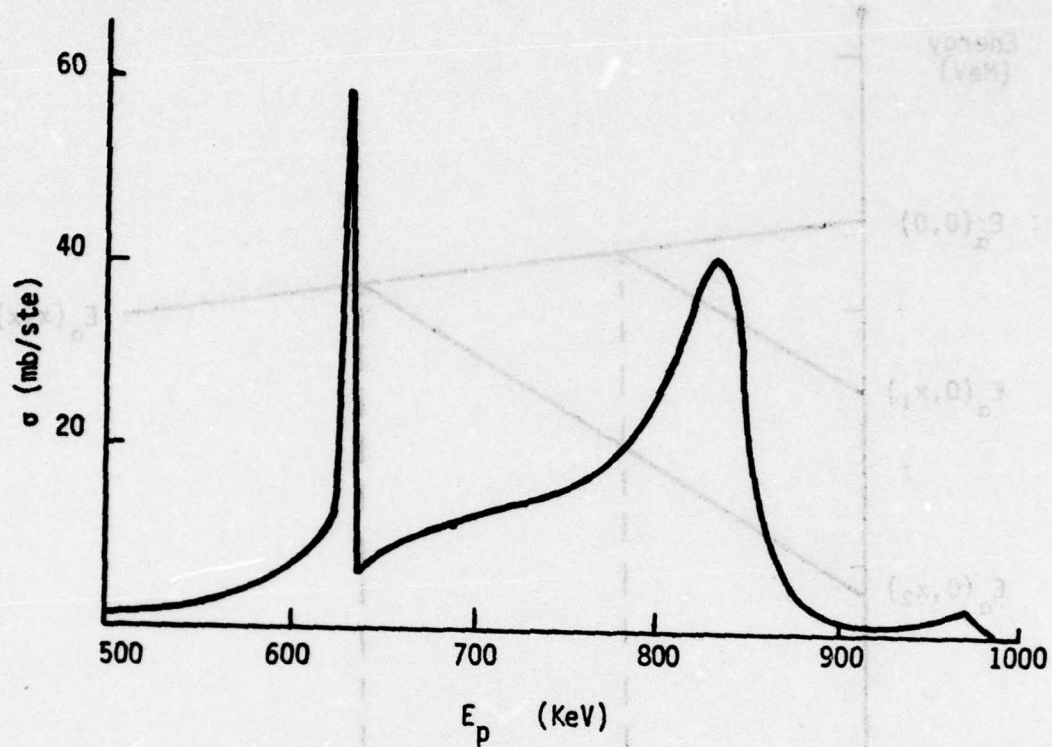


Figure 13: Absolute cross section of $^{18}\text{O}(p,\alpha)^{15}\text{N}$ reaction as a function of incident energy ($\psi=165^\circ$).

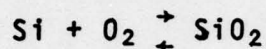
convoluted with a spreading function, $P(E_i, E_j)$, which is the probability that an alpha particle that should be recorded in channel i will be recorded in channel j . The distorted spectrum, $[N_i]$, will then be given by

$$[N_i] = \sum_j N_j P(E_i, E_j) \quad (38)$$

SECTION III MECHANISTIC MODELS

3.1 Introduction

The kinetics of the thermal oxidation reaction



will be controlled by either the outward diffusion of silicon ions or the inward diffusion of oxygen atoms, molecules, or ions. In order to determine the reaction mechanism it is necessary to perform a marker study.

Conventional marker studies of the Smigelskas and Kirkendall (46) type are difficult to perform in systems where there is good oxidation resistance due to the length of time required to grow an oxide scale of sufficient thickness. It has been estimated by Jorgensen (13) that this experiment on silicon would require 10^5 years using a wire marker 0.002 inch in diameter.

Another possible type of marker study is to mark the sample surface with implanted atoms (47-48). This method, however, can lead to erroneous results, since it must be assumed that such "marker" atoms are truly inert,

i.e., the implantation process does not affect the oxidation reaction, and the inert gas is immobile.

The best way to study the oxidation of an oxidation resistant material is to perform a tracer study similar to those performed by Bardeen, Brattain, and Shockley (49) and Holt and Himmel (50). In this type of study, an isotope of one of the reacting species is incorporated in the growing scale. By locating the isotope after the completion of oxidation it is possible to determine the reaction mechanism. Holt and Himmel (50) have presented the expected tracer distributions for the case where oxidation occurs by the transport of an ionic species and either the cation or anion is used as a tracer. These profiles are shown schematically in Figure 14.

Figures 14a and b show the expected tracer distribution if the oxidation reaction is controlled by the transport of metal ions from the metal-oxide interface to the oxide-gas interface with the reaction occurring at the oxide-gas interface. Figure 14a shows the tracer distribution if a radioactive cation is used as the tracer and Figure 14b the tracer distribution if a radioactive anion is used as the tracer. Figures 14c and d show the corresponding situation for the case where the oxidation reaction is controlled by the transport of an ionic oxygen species and the chemical reaction occurs at

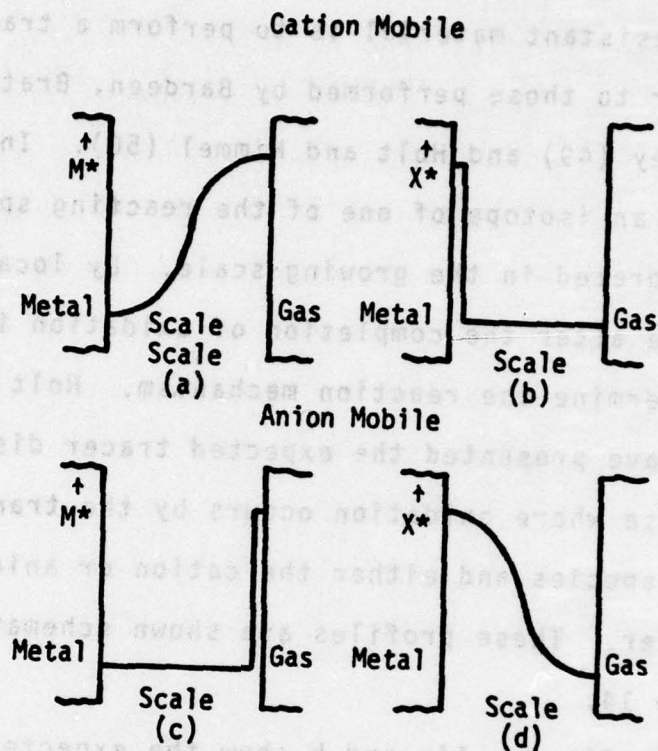


Figure 14: Expected cation (M^*) and anion (X^*) tracer distributions in the scale under conditions (a) and (b), respectively, where the cation is the diffusing component. The corresponding distributions in situations where the anion is the mobile species are indicated by (c) and (d), respectively (50).

the metal-oxide interface. Figure 14c shows the case if an isotope of the metal is used as the tracer and Figure 14d the case if an oxygen isotope is used as the tracer.

The profiles presented in Figures 14b and d cover the situation where the thermal oxidation of silicon is controlled by the transport of an ionic species through the adherent silica scale, but do not cover the possibility that the thermal oxidation is controlled by the transport of molecular oxygen through the silica scale as predicted in the literature. The problem is further complicated if the oxidation reaction involves an exchange reaction along with the transport process as predicted by Ligenza and Spitzer (22).

The remainder of this chapter will be devoted to a discussion of the expected oxygen-18 profiles assuming the oxidation reaction is controlled by the transport of molecular oxygen, ionic oxygen, and ionic silicon. Each profile has been developed by assuming the sample has been oxidized in pure oxygen-18 to produce a scale of half the desired final thickness. The ambient gas is then changed to pure oxygen-16 and the oxidation continued until the final thickness is reached. The sample is then analyzed and the oxygen-18 concentration versus depth profile obtained. These profiles are shown as oxygen-18 concentration as a function of scale thickness, y , with

$y = 0$ being the oxide-gas interface, $y = y_1$ the initial oxygen-18 scale thickness, and $y = 2y_1$ the final scale thickness.

3.2 Oxidation Controlled by the Transport of Molecular Oxygen

3.2.1 General

If the thermal oxidation of silicon is controlled by the transport of molecular oxygen from the silica-gas interface to the silicon-silica interface and the transport process is similar to that proposed by Meek (26) for oxygen diffusion in silica (the permeating oxygen exchanges with the network oxygen) then three types of possible profiles exist depending on the relative rates of permeation and exchange. In the first case the rate of permeation is much greater than the rate of exchange (the case for no exchange is a special case of this); the second case is for the permeation rate to be less than the exchange rate; and the third case is intermediate to the first two. Each of these cases will be discussed below.

Although a mathematical solution for these three cases will not be presented, it should be possible to express the permeation rate by the following equation (51):

$$\text{Permeation Rate} = \frac{DSP\alpha}{y} \quad (39)$$

where S is the solubility of oxygen in silica, P the pressure across the oxide, and α the cross sectional area.

Two exchange reactions will also occur. The first exchange occurs at the sample surface and involves an exchange between the ambient oxygen and the surface. This exchange rate can be expressed by the following equation:

$$\text{Surface Exchange Rate} = K (C_e - C_0) a \quad (40)$$

where K is the surface exchange coefficient, C_e the concentration of oxygen-18 in the ambient and C_0 the concentration of oxygen-18 at $y = 0$. It has been assumed in this section that the surface exchange coefficient, K , is equal to infinity. The other exchange occurs between the permeating oxygen and the network oxygen; this exchange rate can be expressed by,

$$\text{Exchange Rate} = K_1 ([^{16}\text{O}_2] - [\text{Si}^{18}\text{O}_2]) a' \quad (41)$$

where K_1 is the exchange coefficient, $[^{16}\text{O}_2]$ the concentration of oxygen-16 in the permeating gas, $[\text{Si}^{18}\text{O}_2]$ the concentration of oxygen-18 incorporated in the silica scale, and a' the area of the interstitial sites.

3.2.2 Case I: The Rate of Permeation Much Greater than the Rate of Exchange

If the rate of permeation is much greater than the rate of exchange then the expected oxygen-18 concentration versus depth profile will be that shown in Figure 15. Here

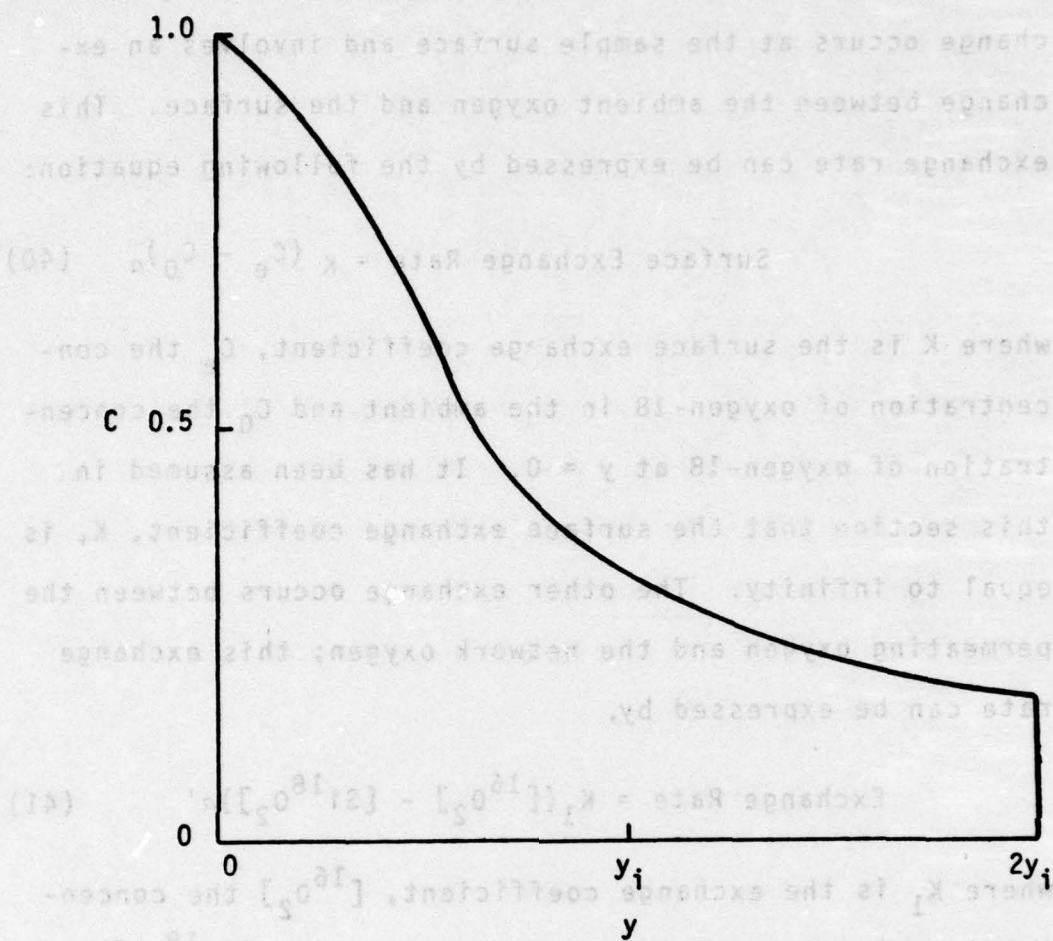


Figure 15: Case I: The rate of permeation much greater than the rate of exchange.

the incoming oxygen-16 from the second oxidation has a high probability of being transported through the existing silica scale and reacting at the silica-silicon interface without exchanging with any of the network oxygens. It is therefore expected that the oxygen-18 will remain peaked at the silica-oxygen interface.

3.2.3 Case II: Rate of Permeation Less than the Rate of Exchange

In this case the thermal oxidation reaction is again controlled by the transport of molecular oxygen to the silica-silicon interface, but the relative rates of permeation and exchange are different than in the previous case causing the oxygen-18 marker to be located at the silica-silicon interface. This is shown in Figure 16. The development of this profile can be visualized as follows: as a molecule of oxygen-16 dissolves in the silica scale the probability of one of the atoms of oxygen-16 exchanging with an oxygen-18 atom in the network is greater than the probability of it moving to the next site. The probability of the other oxygen-16 exchanging with a network oxygen-18 is also high. It is therefore expected that the oxygen-16 from the second part of the oxidation will be incorporated into the silica scale at the silica-oxygen interface and the oxygen reaching the silica-silicon interface will be oxygen-18.

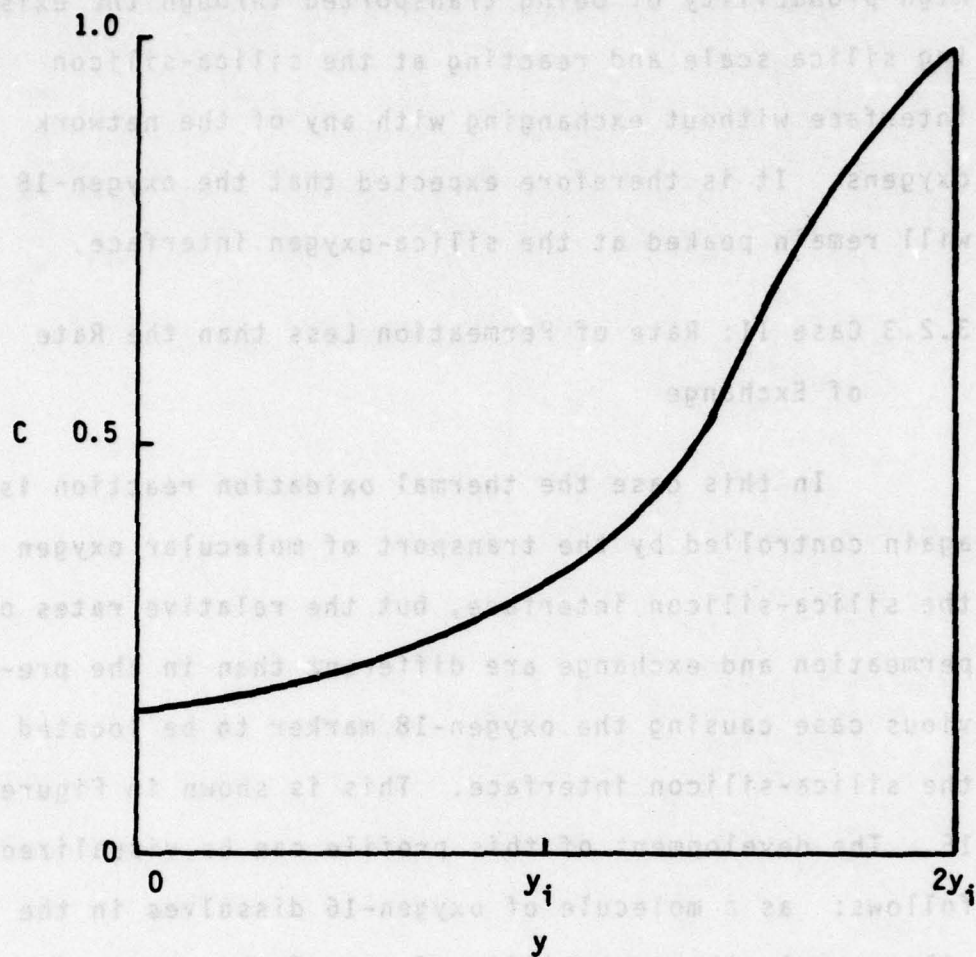


Figure 16: Case II: The rate of permeation less than the rate of exchange.

3.2.4 Case III: Relative Rates of Permeation and Exchange Intermediate to Cases I and II

It can be expected that if the relative rates of exchange and permeation are intermediate to Case I (permeation rate much greater than exchange rate) and Case II (permeation rate less than exchange rate), then the predicted oxygen-18 concentration versus depth profile will be intermediate to those shown in Figures 15 and 16. Here the location of the oxygen-18 "marker" will be peaked between the silica-oxygen interface and the silica-silicon interface.

The development of this type of profile is shown in Figures 17a - 17e for the case where the permeation rate is greater than the exchange rate and can be understood as follows:

Figure 17a shows the expected oxygen-18 concentration versus depth profile at the completion of the initial oxidation. Here the silica scale thickness is y_1 and is composed entirely of oxygen-18.

In order to see the development of Figure 17b - 17e it is necessary to propose some type of model. The simplest model is to assume that the silica scale can be divided into discrete layers each containing the same number of network oxygens. It is then assumed that the oxidation reaction occurs in discrete steps in the following

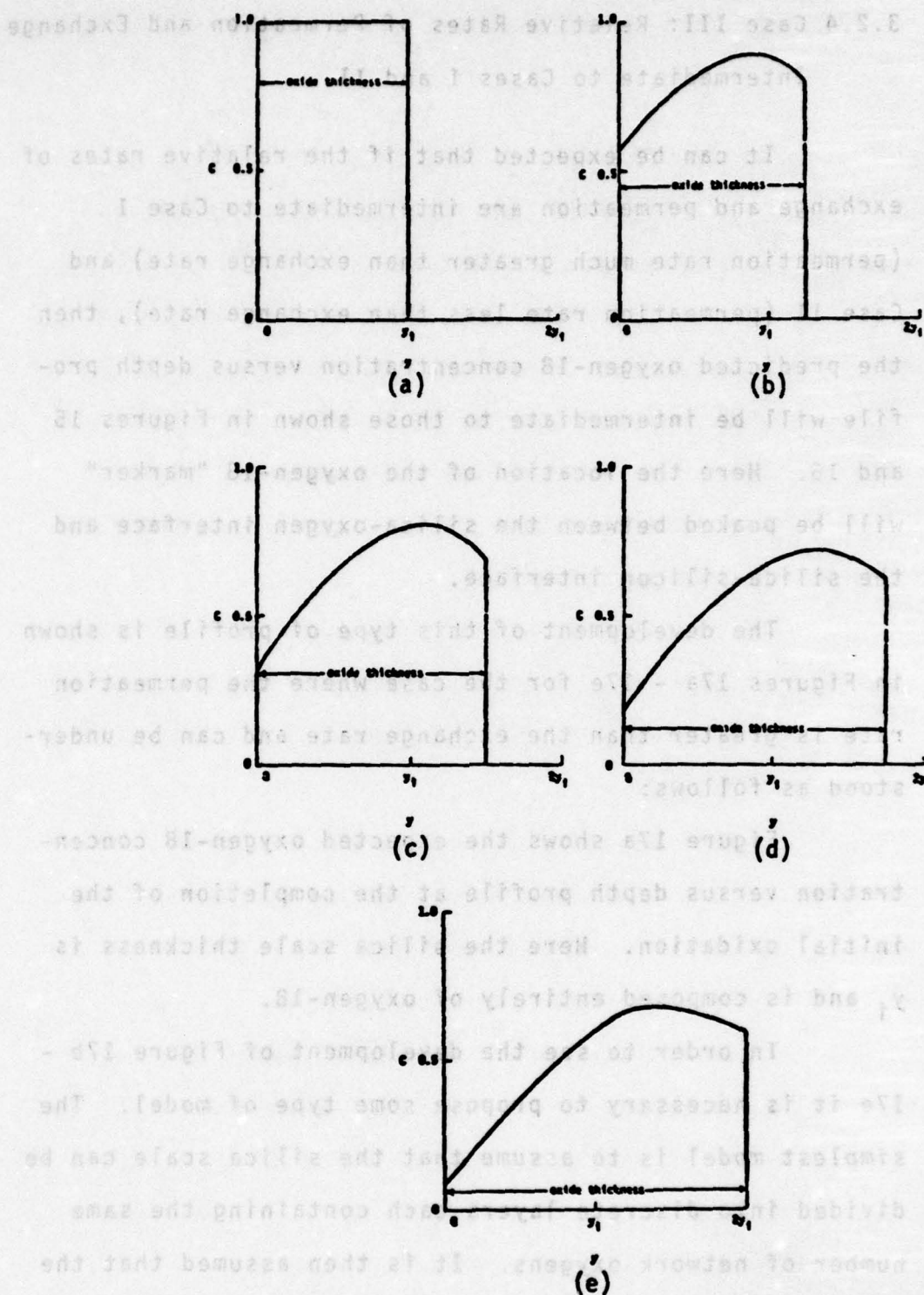


Figure 17: Case III: The relative rates of permeation and exchange are intermediate to Cases I and II at various oxide thicknesses (a) $y = y_i$; (b) $y = 1.25y_i$; (c) $y = 1.5y_i$; (d) $y = 1.75y_i$; (e) $y = 2.0y_i$.

manner. The number of oxygens required to form the next discrete layer of oxide is dissolved in the first layer of silica. This assumes an oxygen solubility in silica that is much greater than actually exists (the same solution is arrived at if it is assumed a smaller amount of oxygen is dissolved in the first layer and the process repeated until enough oxygen has passed through the layer to form one new discrete layer of scale). In the first layer a given fraction (depending on the relative rates of permeation and exchange) of the dissolved oxygen will exchange with network oxygens. This exchange will occur since the silica is not a perfect network of silicon and oxygen, i.e. vacancies exist in the silica network. These vacancies allow some of the dissolved oxygen to become part of the silica network, and to maintain thermodynamic equilibrium some of the network oxygens will enter the dissolved oxygen by the breaking of silicon to oxygen bonds. It has also been assumed here that there is no isotopic preference to the exchange reaction. The dissolved oxygen then moves to the next layer where the process repeats itself. Once the dissolved oxygen has traversed the entire silica scale it reacts completely at the silica-silicon interface to form a new discrete layer of scale. The amount of oxygen required to produce the next layer of silica is now dissolved in the first layer of silica and the above

process repeated. This continues until the silica scale thickness has increased to $2y_1$.

For the purpose of these figures it will be assumed that ten percent of the oxygen exchanges in each layer. Then if there are one hundred oxygens in each discrete layer we find that one tenth of the oxygen that dissolves in the first layer to form the new oxide will exchange. Therefore the oxygen moving to the next layer will be composed of ninety atoms of oxygen-16 and ten atoms of oxygen-18. Ten percent of these oxygens will now exchange with the second layer or nine oxygen-16's and one oxygen-18. The gas moving to the third layer is then eighty-one percent oxygen-16 and nineteen percent oxygen-18. This process continues until one-tenth of the dissolved oxygen has exchanged with the oxygen in the last layer of silica. This oxygen then reacts with the silicon to form new oxide with a composition equal to the composition of the dissolved gas after the final exchange. Once this layer of oxide is formed the oxygen required to form the second layer of new oxide will be dissolved in the first layer. Here one-tenth or ten of the oxygens will exchange with the network oxygens, but the first layer presently has a composition of ten percent oxygen-16 and ninety percent oxygen-18 making only ninety percent of these exchanges effective. After the exchanges occur the scale will be eighty-one percent oxygen-18 and the gas

moving to the second layer will be nine percent oxygen-18. Ten percent of the oxygen-16 in the gas will now exchange with the oxygen in the second layer, but only ninety-one percent of these exchanges will effect the scale composition. Ten percent of oxygen-18 in the gas will also exchange with the silica scale and nine percent of these exchanges will be effective in changing the scale composition. The new scale will now be composed of eighty-four percent oxygen-18 and sixteen percent oxygen-16. The dissolved gas transferred to the third layer will be sixteen percent oxygen-18. This process continues until the permeating gas has exchanged with the last silica layer. It then reacts with the silicon forming a new layer of silica and the gas required for the next silica layer is dissolved and the process repeated until the scale thickness has increased to $2y_i$.

Figures 17b - e show the calculated oxygen-18 concentration versus depth profiles assuming that ten percent of the oxygen exchanges in each layer. Figure 17b shows the oxygen-18 concentration versus depth profile when the scale thickness has increased to $1.25 y_i$. It can be seen the oxygen-18 concentration exhibits a maximum within the scale instead of at either interface. Figure 17c shows the concentration versus depth profile when the scale is $1.5 y_i$ thick. Figures 17d and 17e show the continued

development of the oxygen-18 concentration versus depth profile when the scale thickness has increased to $1.75 y_i$ and $2.0 y_i$ respectively. It can be seen from Figure 17e that the final profile exhibits a maximum in oxygen-18 concentration profile at approximately $1.3 y_i$.

3.3 Oxidation Controlled by the Transport of an Ionic Species

3.3.1 Case IV: Ionic Transport of Oxygen

If the thermal oxidation of silicon is controlled by the transport of an ionized species of oxygen as predicted by Jorgensen (13) the concentration profile will be given by the Wagner Theory (see Section 2.1.4) or the Morin modification to the theory of point defect diffusion (52). Here the oxygen-18 will be found peaked at the silicon-silica interface as is shown in Figure 18.

3.3.2 Case V: Ionic Transport of Silicon

It is also possible that the thermal oxidation reaction is controlled by the diffusion of silicon ions with the reaction occurring at the silica-oxygen interface. If this is the situation the oxygen-18 from the first oxidation is expected to be located at the silicon-silica interface as a step function to first approximation. The expected oxygen-18 distribution is shown in Figure 19.

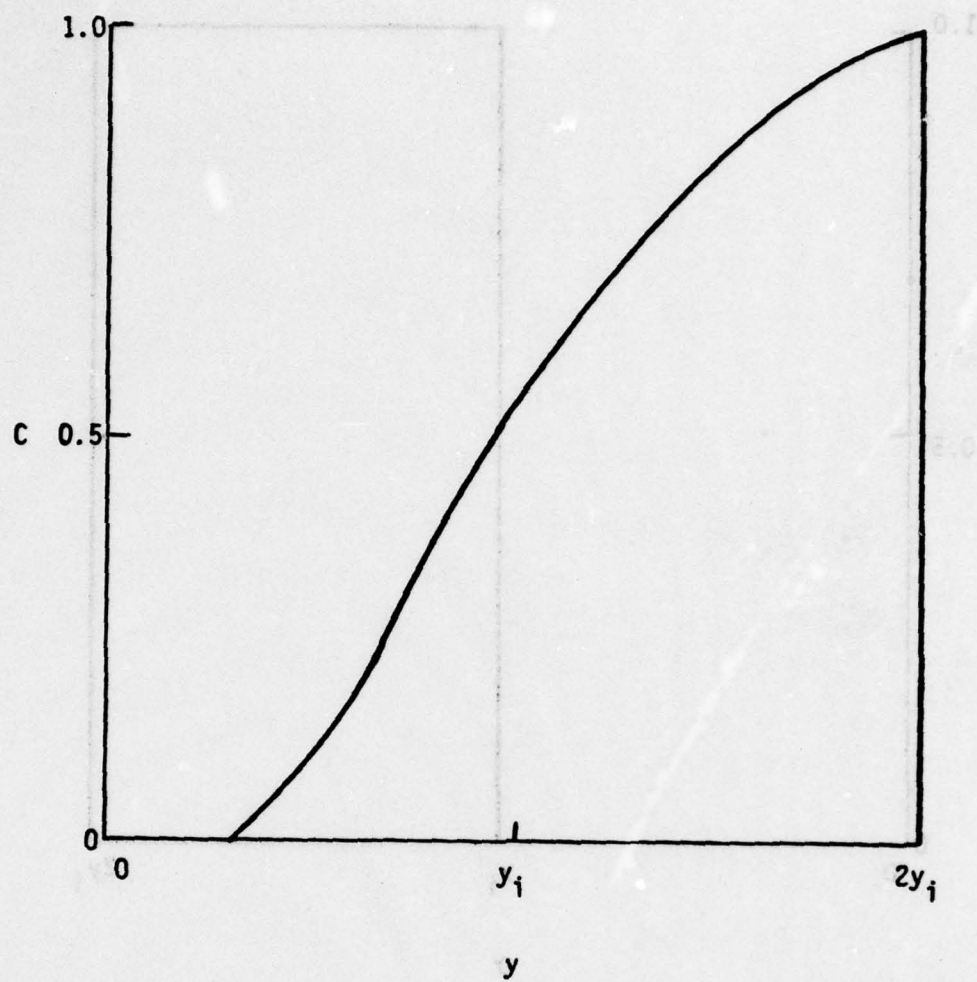


Figure 18: Case IV: The ionic transport of oxygen.

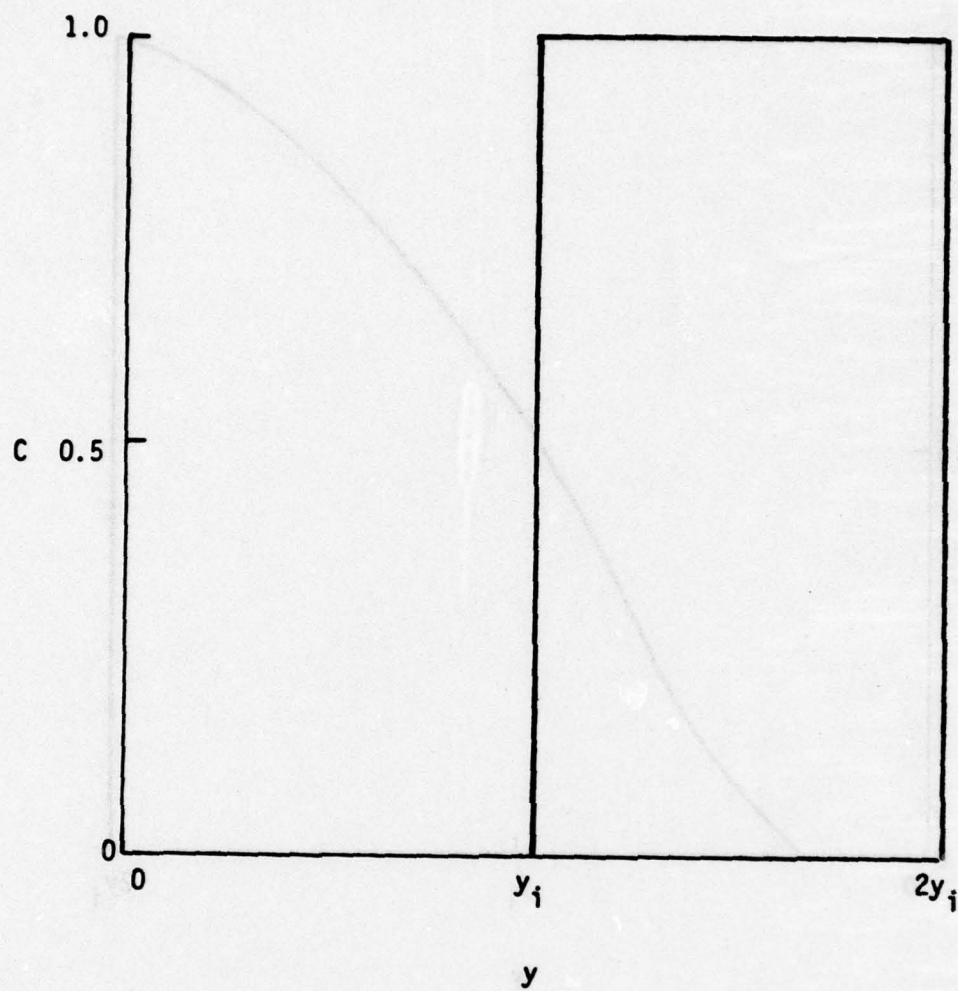


Figure 19: Case V: The ionic transport of silicon.

SECTION IV

EXPERIMENTAL PROCEDURE

4.1 Samples

The silicon coupons* used in these thermal oxidation studies were oriented in the (110) direction and were n-type crystals with a phosphorus dopant level of 10^{15} atoms per cubic centimeter. The coupons were one half millimeter thick and cut to an eight millimeter square.

The coupons were mirror finished on one side and were cleaned by the following procedure: (1) deionized water rinse; (2) ultrasonic rinse in $\text{NH}_4\text{OH}:\text{H}_2\text{O}_2:\text{H}_2\text{O}$ (1:1:5); (3) repeat 1; (4) ultrasonic rinse in $\text{HCl}:\text{H}_2\text{O}_2:\text{H}_2\text{O}$ (1:1:5); (5) repeat 1; (6) 48% HF rinse; (7) repeat 1; (8) dry in dried air.

4.2 Thermal Oxidations

4.2.1 Oxidation Apparatus and General Procedures

Figure 20 shows a schematic diagram of the oxidation apparatus. The system is designed in such

* This single crystal silicon was obtained from Ventron Corporation of Bradford, Pennsylvania.

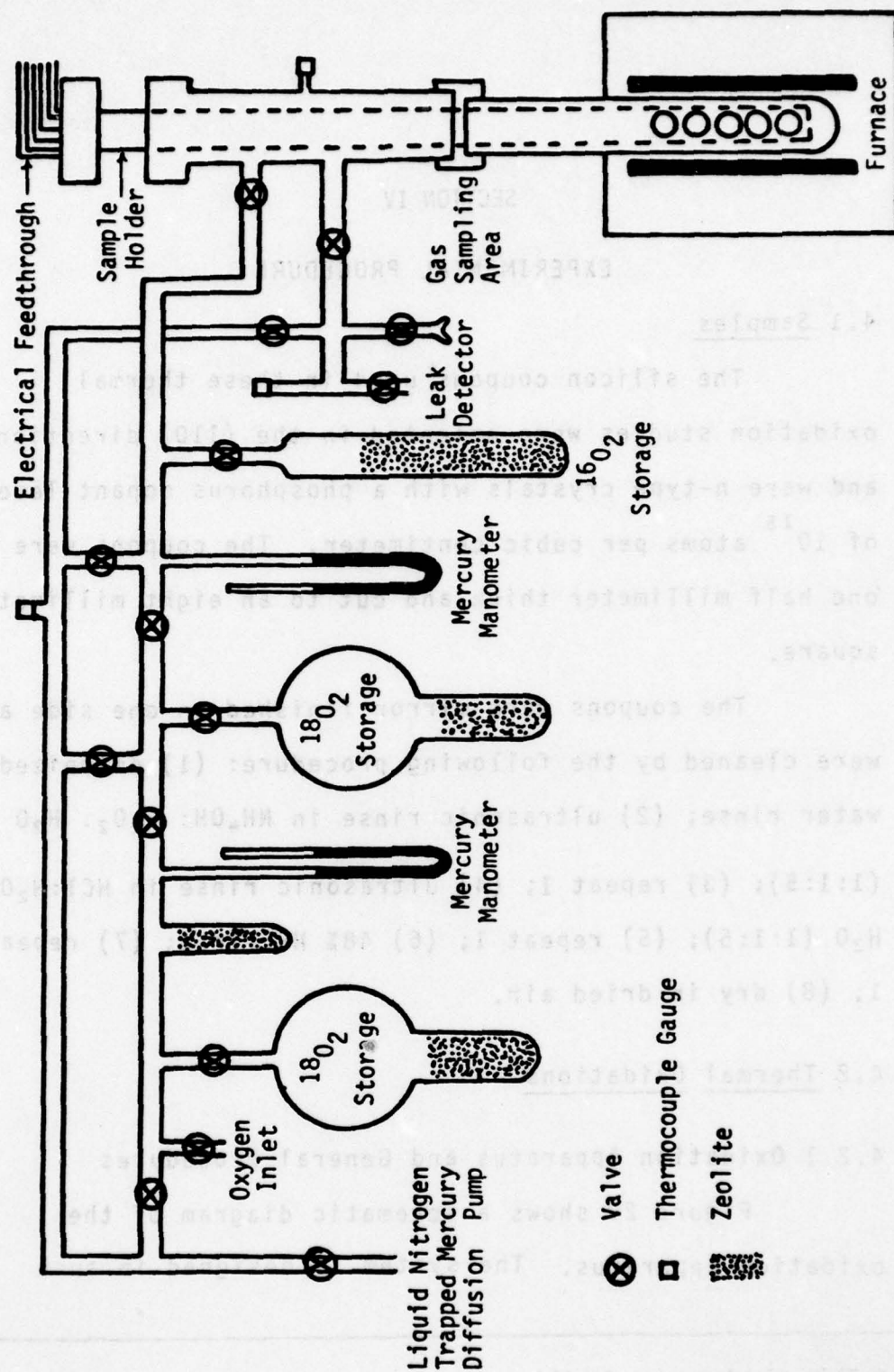


Figure 20: Schematic diagram of the oxidation apparatus.

a way as to allow the static oxidation of up to five samples which rested on alumina shelves in the sample holder. A Pt-6%Rh, Pt-30% Rh thermocouple is located next to each sample position to enable continuous temperature monitoring.

The oxygen used in the oxidation experiments was stored in Pyrex bulbs which have a zeolite-filled finger to aid in removing the oxygen from the system and to insure that the oxygen is dry. The pure oxygen gas was enriched to between 10 and 20 atom percent oxygen-18; and the oxygen-18 depleted gas was research-grade oxygen.

After placing the silicon coupons in the oxidation chamber, the chamber was evacuated using a liquid-nitrogen-trapped mercury diffusion pump to a pressure of no more than 10 microns of mercury. The system was then leak checked using a helium leak detector to insure that the system was leak free. The oxidation chamber was then heated to temperature while continued pumping maintaining a vacuum of no more than 10 microns of mercury.* Once the system reached the desired temperature it was again leak checked to be sure no leaks had developed during heating. If no leaks were present, the system was pressurized to approximately 780 millimeters of mercury with oxygen. During the oxidation run, the sample temperature

* This procedure insured that no silica was on the sample surface at the start of the experiment.

was continuously monitored using a strip chart recorder. When the desired oxidation time was reached, the furnace was shut off and the oxygen removed via the zeolite fingers. Once the oxygen had been removed the sample holder was raised and the furnace lowered to allow the system to finish cooling. When the oxidation chamber reached a temperature of approximately 800°K dry air was introduced to the chamber. This entire shut-down procedure required thirty minutes from the time the furnace was shut off until the samples could be transferred to a dessicator.

Throughout the course of the oxidation run, gas samples were periodically withdrawn in order to monitor the isotopic composition. A minimum of four gas samples were drawn during each run.

4.2.2 Kinetic Oxidation Experiments

The kinetic experiments involved oxidizing samples in an oxygen-18 enriched oxygen atmosphere for various times at several temperatures. The temperature range selected for the kinetic study was $1089 \pm 5^\circ\text{K}$ to $1473 \pm 5^\circ\text{K}$. The oxidation times ranged from ten to thirty hours.

4.2.3 Tracer Experiments

The tracer experiments were performed in the same

temperature range as the kinetic experiments. The silicon coupons were oxidized in an oxygen-18 enriched oxygen atmosphere to give a silica scale thickness of approximately 4500 A. The oxidation was interrupted and the oxygen-18 enriched oxygen replaced with oxygen-18 depleted oxygen and the oxidation continued to approximately 9000 A.

These experiments were repeated with the isotopic order reversed as an internal check on the experiment.

4.3 Charged Particle Activation Analysis

4.3.1 Sample Preparation and Positioning

After the coupons were oxidized they were placed in the center of an aluminum blank one inch in diameter and of a thickness such that the combined coupon-blank thickness was 0.275 inch. This assemblage was then placed in an evaporator and a thin layer of aluminum (approximately 100 A)* deposited over the sample surface. The samples were then sandwiched between two aluminum blanks with the top blank having a 0.25 inch diameter hole in the center beveled to 0.5 inch diameter at the top of the blank.

* The aluminum film thickness was calculated assuming 4π distribution from the tungsten holder.

This sample preparation has proven to be adequate in conducting both heat and charge from the sample surface during proton bombardment.

Once the samples have been secured in their aluminum holders, they were mounted in a movable frame, capable of holding five samples, in the scattering chamber. The frame is positioned in such a way that the normal to the sample surface makes an angle of $7\frac{1}{2}$ degrees with both the incident proton beam and the alpha particles (the tilting of the sample was not necessary in these studies, but is of importance when working with single crystals to prevent channelling of the protons or alphas). The scattering chamber was then sealed and a vacuum drawn. The chamber was maintained at a pressure of no more than 70 millimicrons of mercury throughout the analysis.

4.3.2 Alpha Particle Measurement and Recording

The energetic alpha particles observed at a laboratory scattering angle of 165° pass through a magnetic spectrometer, designed by Lindstrom and Heuer (46), which removes the backscattered protons from the alpha particles by a magnetic field. The magnetic spectrometer eliminates the need for mylar to separate the alphas from the backscattered protons, which is an advantage since one does not have to worry about the uniformity or stopping power of the mylar (the magnetic field only

changes the particle's direction and does not alter their energy). Figure 21 shows a schematic of the scattering chamber and magnetic spectrometer used in these experiments.

A gold-coated surface barrier detector was used to record the energetic particles. The detector signal was processed (amplified and shaped) and subsequently recorded in a multichannel pulse-height analyzer using a standard electronic set-up (Figure 22).

At the conclusion of the run each recorded spectrum was transferred to punched paper tape for later computer analysis.

4.3.3 The Activation Experiment

The multichannel analyzer was calibrated at the beginning and end of each day using a $\text{Ta}_2^{18}\text{O}_5$ target* and a ZnF_2 target.** The $\text{Ta}_2^{18}\text{O}_5$ calibration run was made at an incident proton energy of 750 KeV and the ZnF_2 run at 850 KeV and 890 KeV giving three calibration points.

Once the MCA had been calibrated the samples were bombarded with protons, and the alpha spectrum

* The $\text{Ta}_2^{18}\text{O}_5$ targets were prepared by Dr. J.P.S. Pringle, Chalk River Nuclear Laboratories, Atomic Energy of Canada, Ltd., Chalk River, Ontario, Canada, by anodically oxidizing tantalum blanks.

**The ZnF_2 targets were prepared by evaporating anhydrous ZnF_2 onto tantalum blanks.

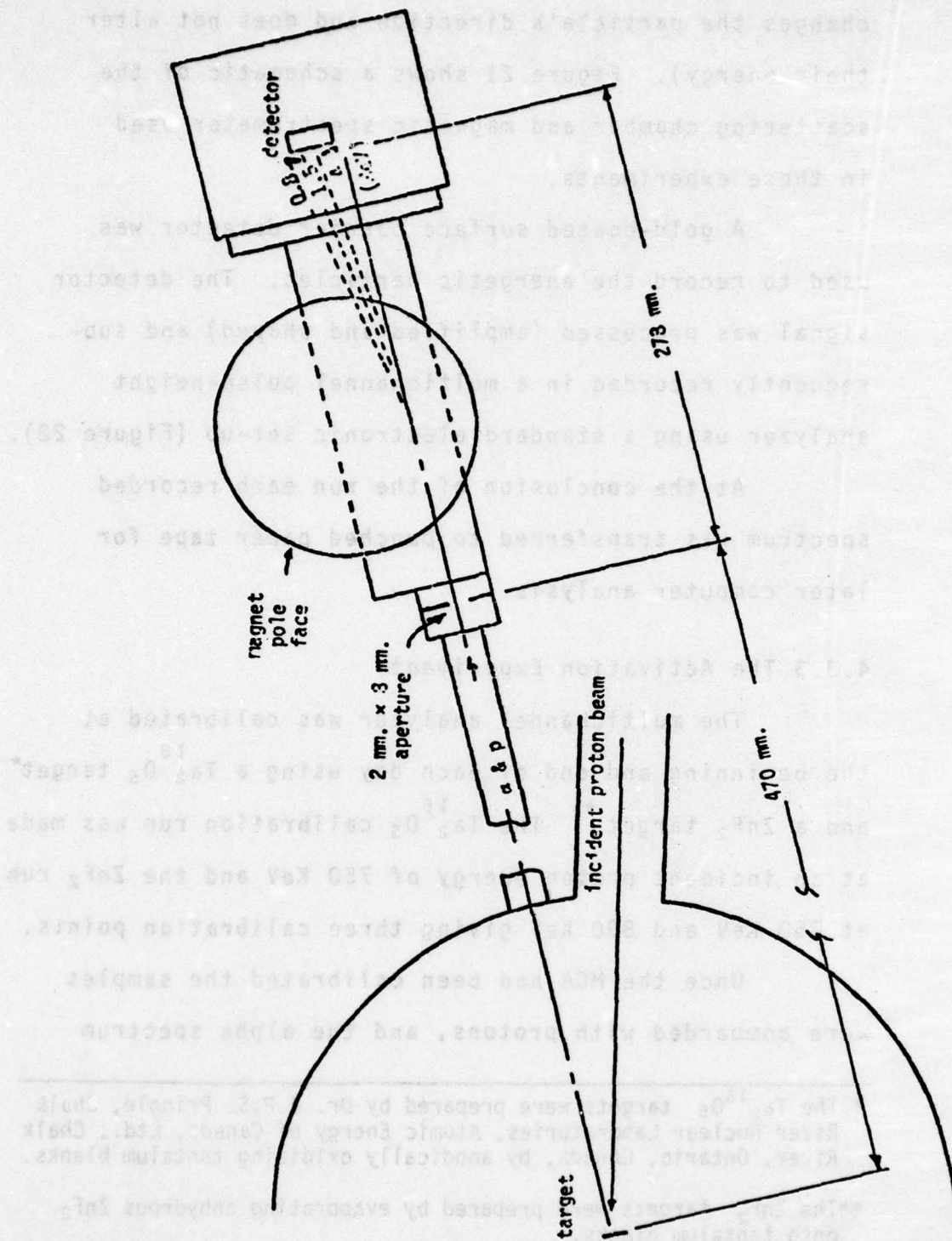


Figure 21: Schematic of the scattering chamber and magnetic spectrometer.

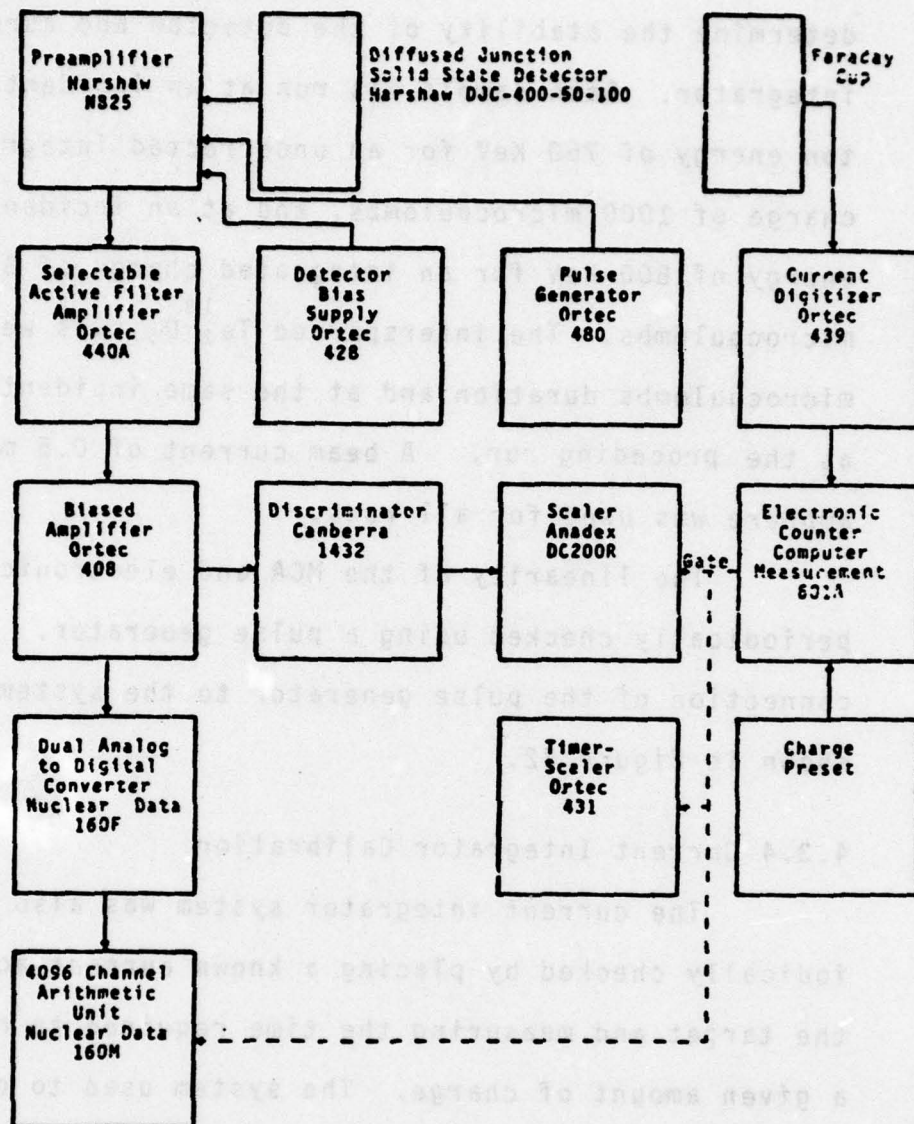


Figure 22: Schematic of electronic circuitry.

recorded for a predetermined proton flux. A $\text{Ta}_2^{18}\text{O}_5$ sample was run between each sample run in order to determine the stability of the detector and current integrator. Each sample was run at an incident proton energy of 750 KeV for an uncorrected integrated charge of 1000 microcoulombs, and at an incident energy of 800 KeV for an integrated charge of 500 microcoulombs. The interspersed $\text{Ta}_2^{18}\text{O}_5$ runs were 100 microcoulombs duration and at the same incident energy as the preceding run. A beam current of 0.5 micro-ampere was used for all runs.

The linearity of the MCA and electronics was periodically checked using a pulse generator. The connection of the pulse generator to the system is shown in Figure 22.

4.3.4 Current Integrator Calibration

The current integrator system was also periodically checked by placing a known current across the target and measuring the time required to collect a given amount of charge. The system used to calibrate the current integrator is shown schematically in Figure 23.

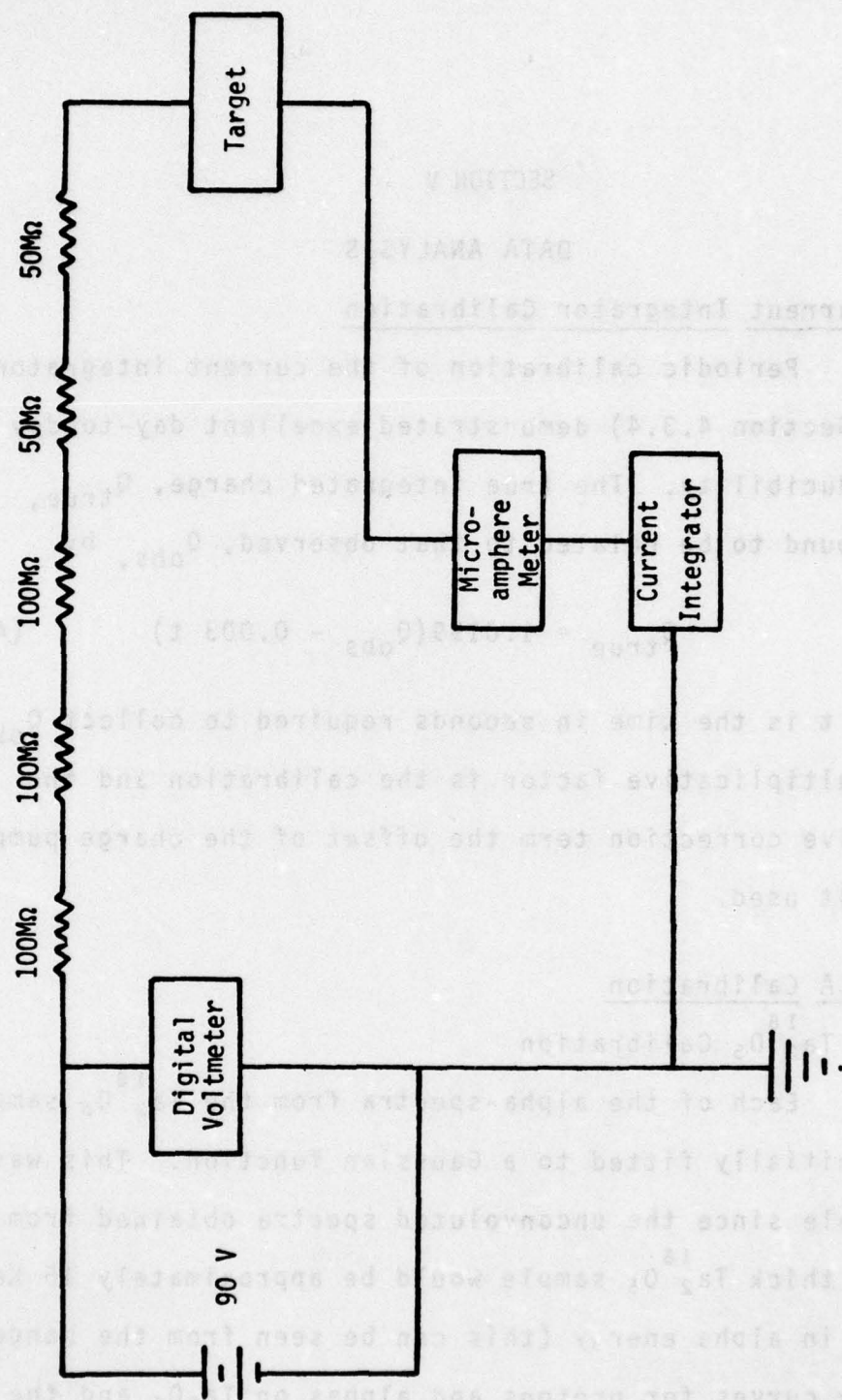


Figure 23: Schematic used to calibrate the current integrator.

SECTION V

DATA ANALYSIS

5.1 Current Integrator Calibration

Periodic calibration of the current integrator (see Section 4.3.4) demonstrated excellent day-to-day reproducibility. The true integrated charge, Q_{true} , was found to be related to that observed, Q_{obs} , by

$$Q_{\text{true}} = 1.0199(Q_{\text{obs}} - 0.003 t) \quad (42)$$

where t is the time in seconds required to collect Q_{obs} . The multiplicative factor is the calibration and the negative correction term the offset of the charge pump circuit used.

5.2 MCA Calibration

5.2.1 $\text{Ta}_2^{18}\text{O}_5$ Calibration

Each of the alpha-spectra from the $\text{Ta}_2^{18}\text{O}_5$ sample was initially fitted to a Gaussian function. This was possible since the unconvoluted spectra obtained from a 530 Å thick $\text{Ta}_2^{18}\text{O}_5$ sample would be approximately 15 KeV thick in alpha energy (this can be seen from the range-energy curves for protons and alphas on Ta_2O_5 and the kinematics of the $^{18}\text{O}(p,\alpha)^{15}\text{N}$ reaction given in Appendix

AD-A069 003

CASE WESTERN RESERVE UNIV CLEVELAND OHIO DEPT OF MET--ETC F/G 11/2
USE OF NUCLEARMICROANALYSIS. PART I. PROTON ACTIVATION STUDIES --ETC(U)
AUG 78 A R COOPER, A H HEUER, L D MAJOR F33615-74-C-4029

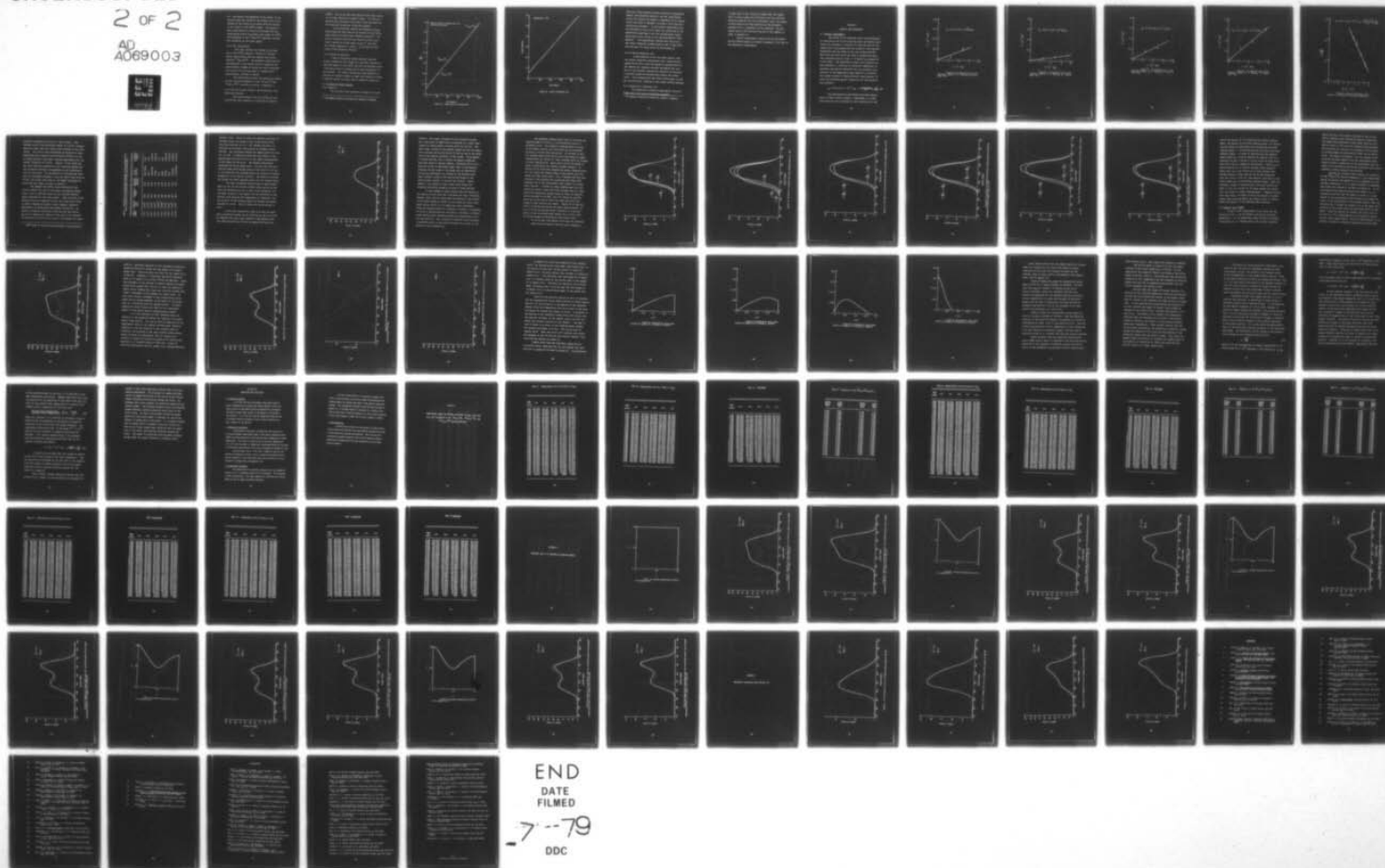
UNCLASSIFIED

AFML -TR-78-119-PT-1

NL

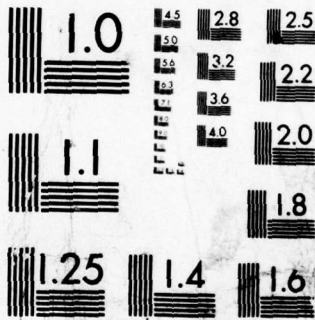
2 OF 2

AD
A069003



END
DATE
FILMED

7-79
DDC



MICROCOPY RESOLUTION TEST CHART
NATIONAL BUREAU OF STANDARDS-1963-A

1). The channel corresponding to the center of the Gaussian peak was therefore the channel which corresponded to the energy of an alpha particle created at the center of the $\text{Ta}_2^{18}\text{O}_5$ sample. The energy of this alpha particle is easily calculated from the range-energy curves for protons and alphas on $\text{Ta}_2^{18}\text{O}_5$, the kinematics of the $^{18}\text{O}(p,\alpha)^{15}\text{N}$ reaction, and the half thickness of the oxide sample.

5.2.2 ZnF_2 Calibration

Each ZnF_2 spectrum was fitted in the same way as the $\text{Ta}_2^{18}\text{O}_5$ spectra. Protons of incident energy approximately 850 KeV undergo the nuclear reaction $^{19}\text{F}(p,\alpha_1)^{16}\text{O}^*$. The energetic alpha particle corresponding to the ground state of oxygen-16 has approximately 6.66MeV of energy and that corresponding to the first excited state of oxygen-16 has approximately 1.99 MeV of energy.

The range-energy curves for protons and alphas on ZnF_2 and the kinematics of the $^{19}\text{F}(p,\alpha)^{16}\text{O}$ and $^{19}\text{F}(p,\alpha_1)^{16}\text{O}^*$ reactions are given in Appendix 1.

5.2.3 MCA Calibration Channel, MCA Dispersion, and Spreading Function

The alpha energies from the $\text{Ta}_2^{18}\text{O}_5$ and ZnF_2 calibrations were graphed as a function of channel

number. As can be seen from Figure 24 the alpha energy is a linear function of channel number. The MCA calibration then consisted of one point from the graph and the slope and dispersion in KeV per channel.

The calibration channel and dispersion determined above was then used to fit several of the $\text{Ta}_2^{18}\text{O}_5$ alpha spectra to obtain the spreading function.* The correct spreading function was found by using a non-linear regression scheme based on the χ^2 test (53), the minimum reduced chi square, χ_r^2 , giving the best value of the spreading function.

5.2.4 Pulser Calibration

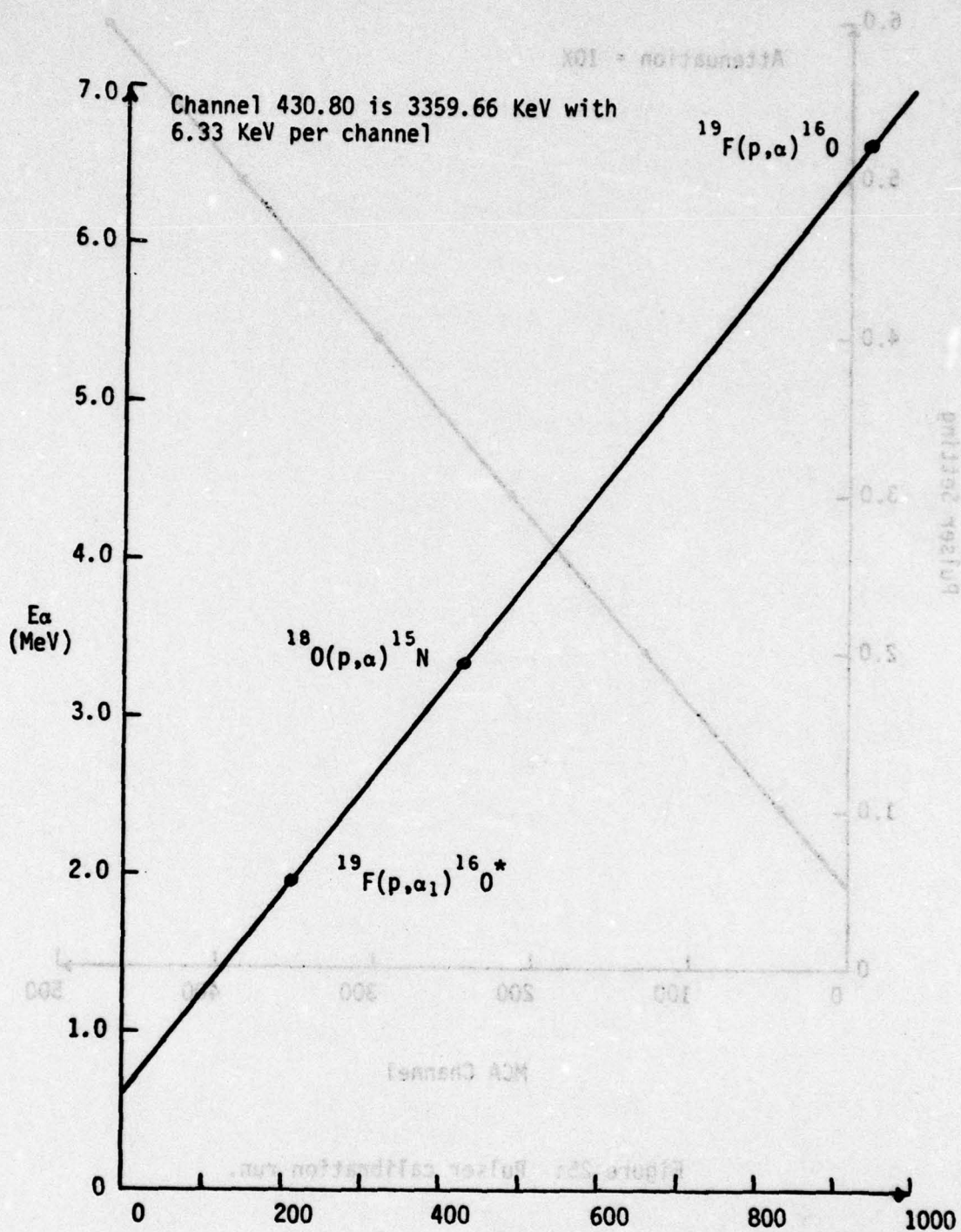
Each of the pulser peaks obtained from the pulser calibration was fitted to a Gaussian function in the same manner as the $\text{Ta}_2^{18}\text{O}_5$ and ZnF_2 calibration peaks - (The pulser peak is spread only by the electronics of the system). The pulser setting was then plotted as a function of channel number to check the linearity of MCA. A typical series of pulser runs is shown in Figure 25.

5.3 Fitting the Alpha Spectra

5.3.1 General

The recorded alpha spectrum for each of the sam-

* The computer program was written by Dr. Walter W. Lindstrom.



MCA Channel
Figure 24: Graph used to calibrate MCA.

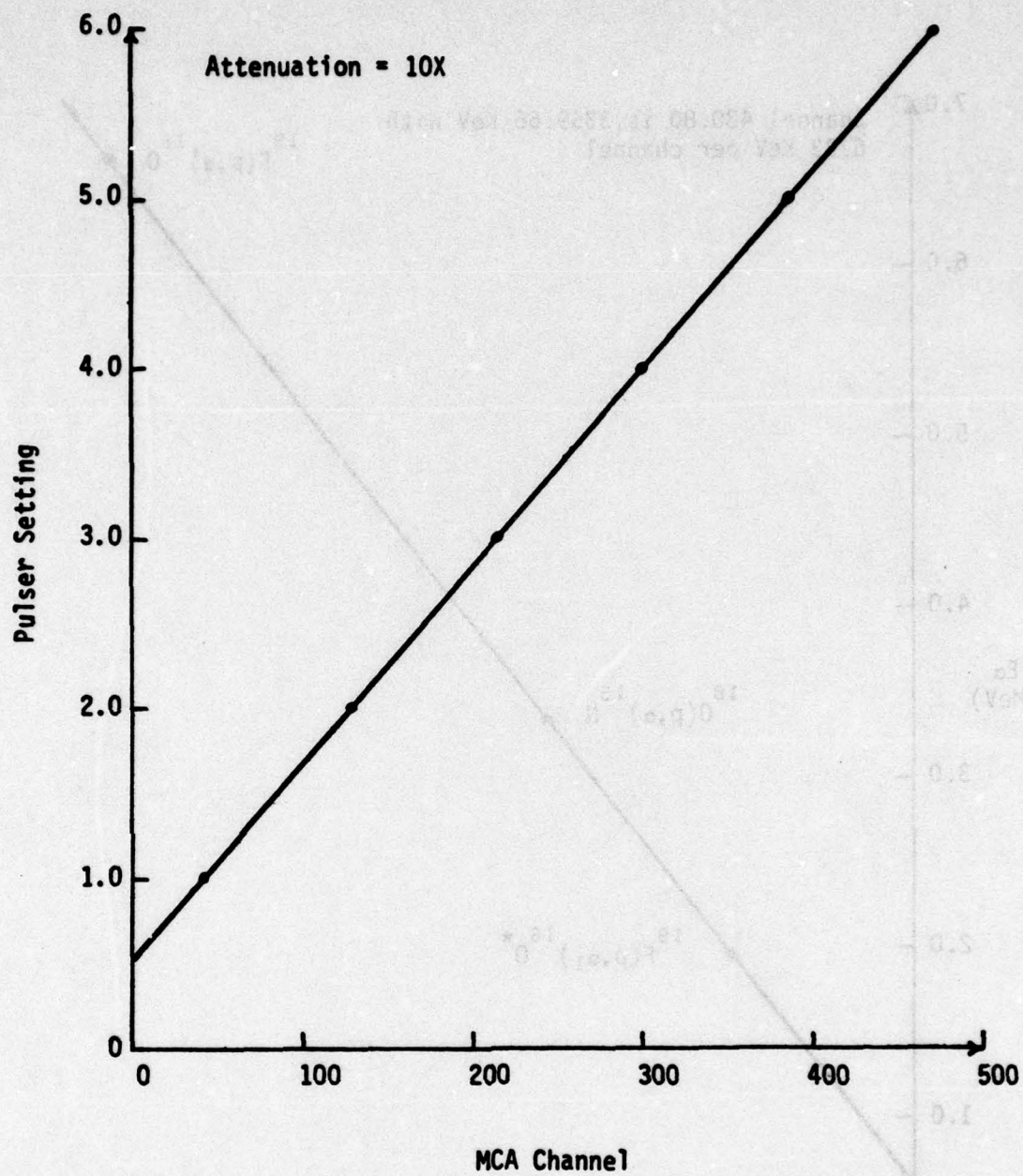


Figure 25: Pulser calibration run.

ples was fitted knowing the MCA calibration (determined above), the spreading function, and the range-energy curves for protons and alphas on amorphous silica (these curves are given in Appendix 1) using a trial and error convolution procedure. In the kinetic experiments only the thickness of the silica layer was varied and in the mechanistic experiments only the concentration versus depth profile was varied to fit the experimental alpha spectra.* The experimental spectra were fit using a non-linear regression scheme based on the χ^2 test (53), with the best fit being given by the minimum χ_r^2 .

5.3.2 Kinetic Oxidation Fits

It was possible to fit the alpha spectra from the kinetic oxidation experiments with a step function oxygen-18 profile, since the oxygen-18 concentration in the ambient gas remained constant throughout the runs. Each of the recorded spectrum was therefore fit assuming a constant oxygen-18 concentration within the silica scale. This concentration was found nearly equal to the gas concentration, implying a very rapid surface exchange.

5.3.3 Mechanistic Oxidation Fits

The mechanistic oxidation experimental data was fitted using a trial and error convolution procedure.

* The computer program was written by Dr. Walter W. Lindstrom.

In each case it was initially assumed that the sample had a uniform oxygen-18 distribution and the predicted spectrum compared with the experimental data; the oxygen-18 distribution was then modified and the procedure repeated until a reasonable χ^2_r was obtained. The procedure used to fit the data from one of the samples is shown in Appendix 2.

Typical experimental spectra and the corresponding calculated spectra are shown in Appendix 3 for some of the mechanistic experiments.

SECTION VI

RESULTS AND DISCUSSION

6.1 Kinetic Experiments

The square of the measured silica scale thickness, as measured by the single spectrum proton activation technique, was plotted as a function of time for each of the temperatures investigated and the parabolic rate constant determined from the slope of the line (Figures 26-29). Note that the point (0,0) was used in determining these rate constants since at time $t = 0$ there is no oxygen-18 silica scale. The logarithm of these rate constants was then plotted as a function of reciprocal temperature to determine the general expression for the parabolic rate constant in the temperature range $1089 \pm 5^\circ\text{K}$ to $1473 \pm 5^\circ\text{K}$. This graph is shown in Figure 30 and a least squares fit gives the following general expression for the parabolic rate constant:

$$k_p = [(7.5 \pm 3.0) \times 10^{-10} \exp - (\frac{1.08 \pm 0.09 \text{eV}}{kT})] \frac{\text{cm}^2}{\text{sec}} \quad (42)$$

The experimentally determined activation energy found in these kinetic studies, $1.08 \pm 0.09 \text{eV}$, is 0.13eV lower than any value reported in the literature for the

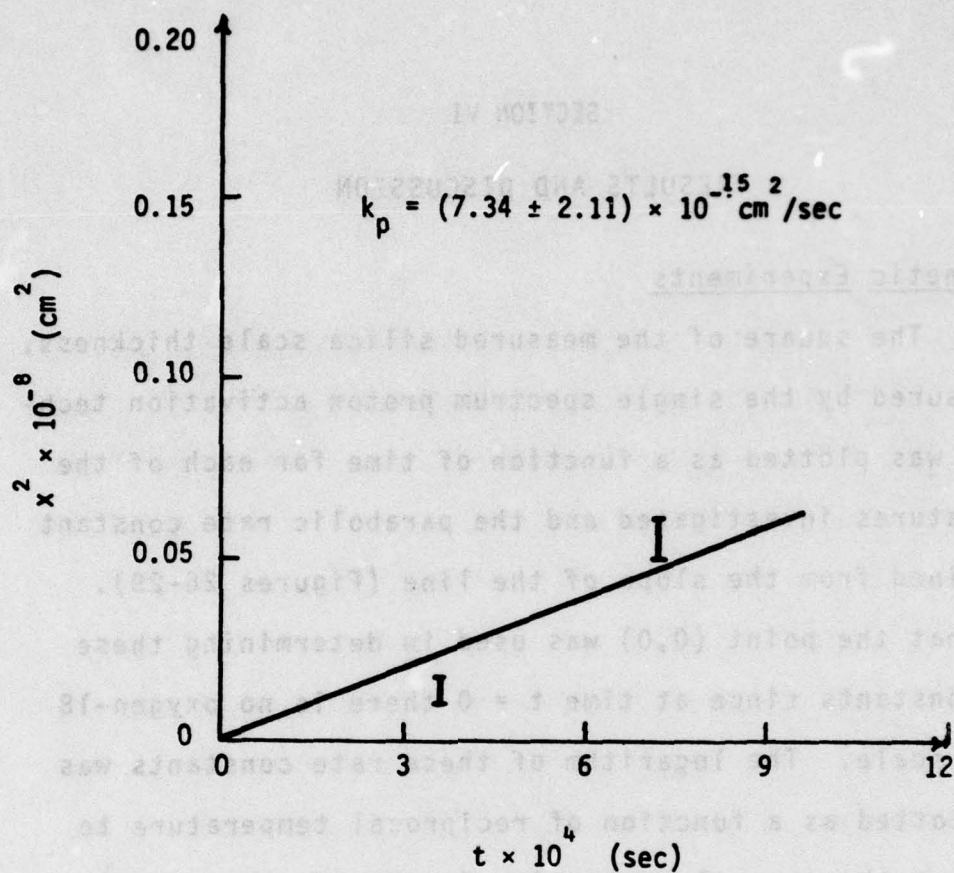


Figure 26: The measured silica scale Thickness squared as a function of time at $1091 \pm 5^\circ\text{K}$.

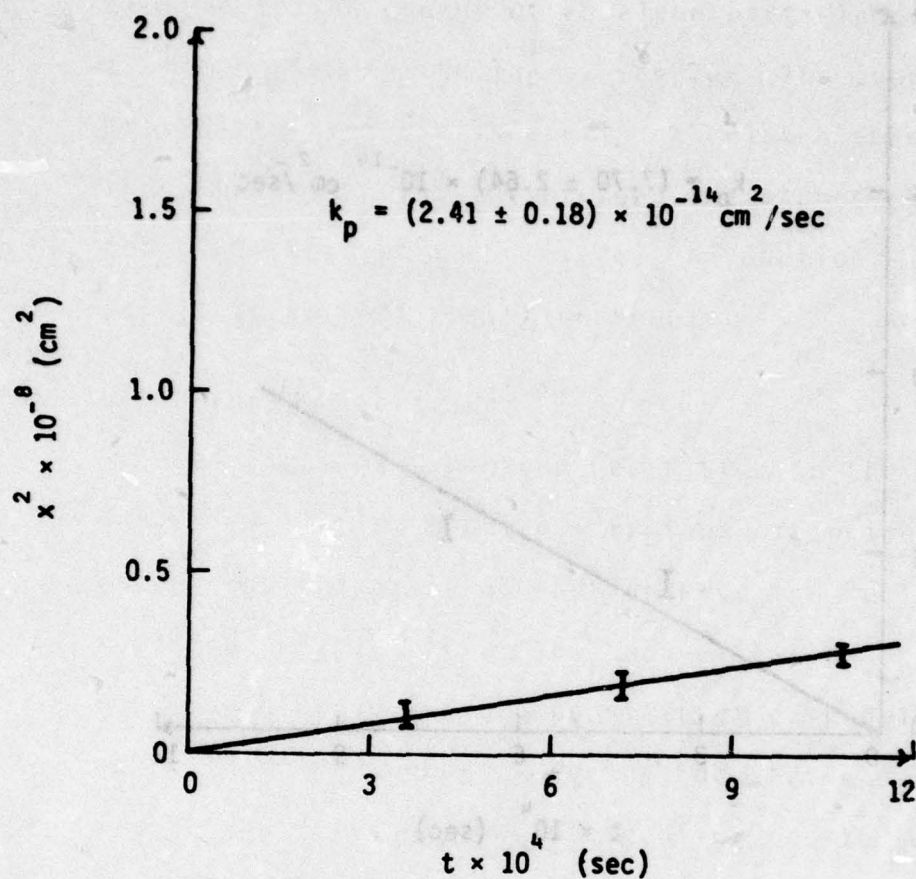


Figure 27: The measured silica scale thickness squared as a function of time at $1200 \pm 5^\circ\text{K}$.

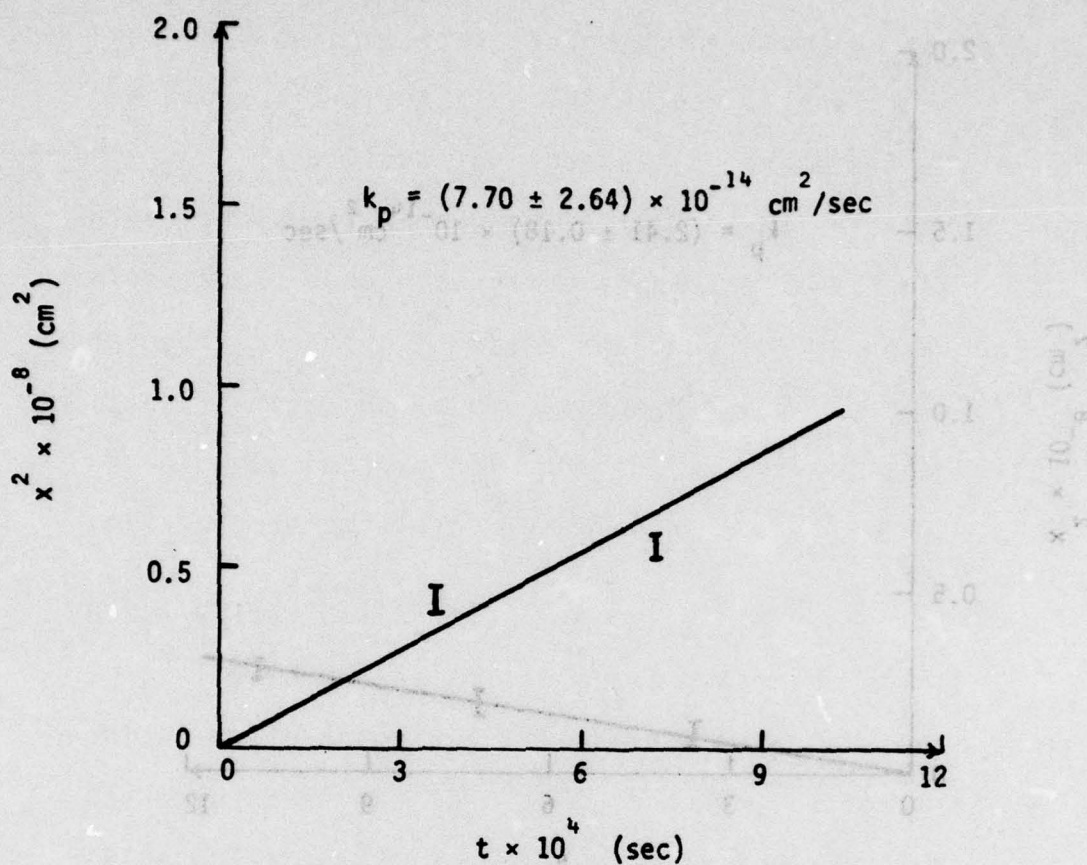


Figure 28: The measured silica scale thickness squared as a function of time at $1337 \pm 5^\circ\text{K}$.

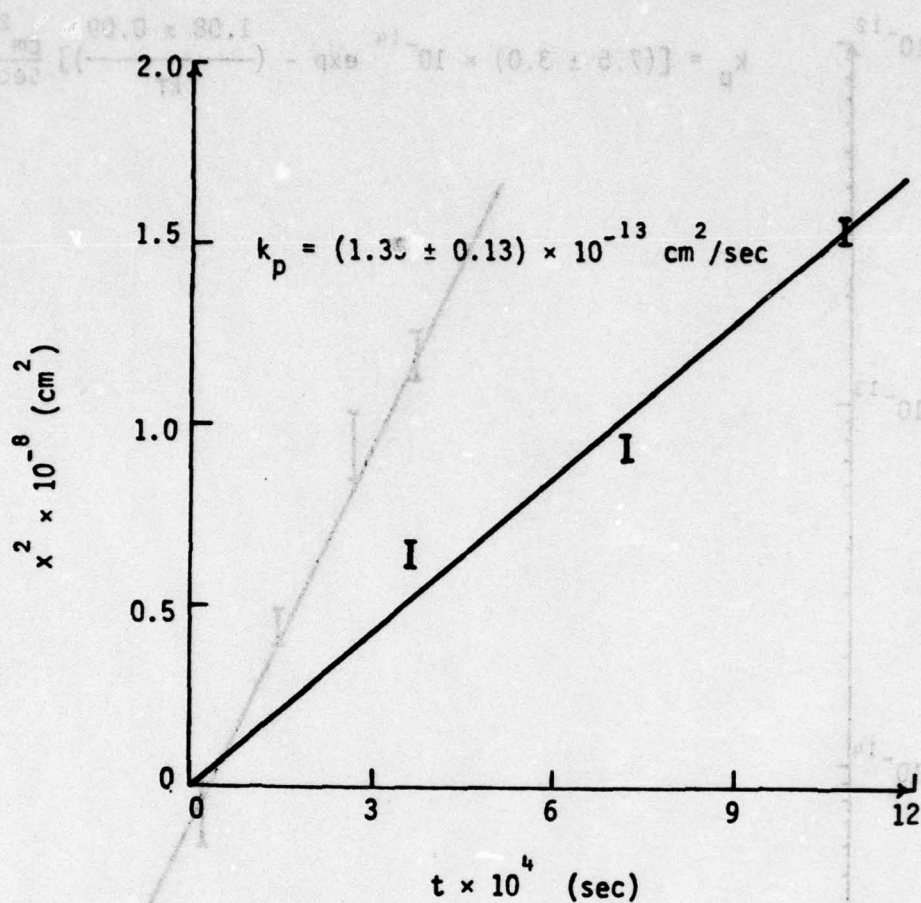


Figure 29: The measured silica scale thickness squared as a function of time at $1473 \pm 5^\circ\text{K}$.

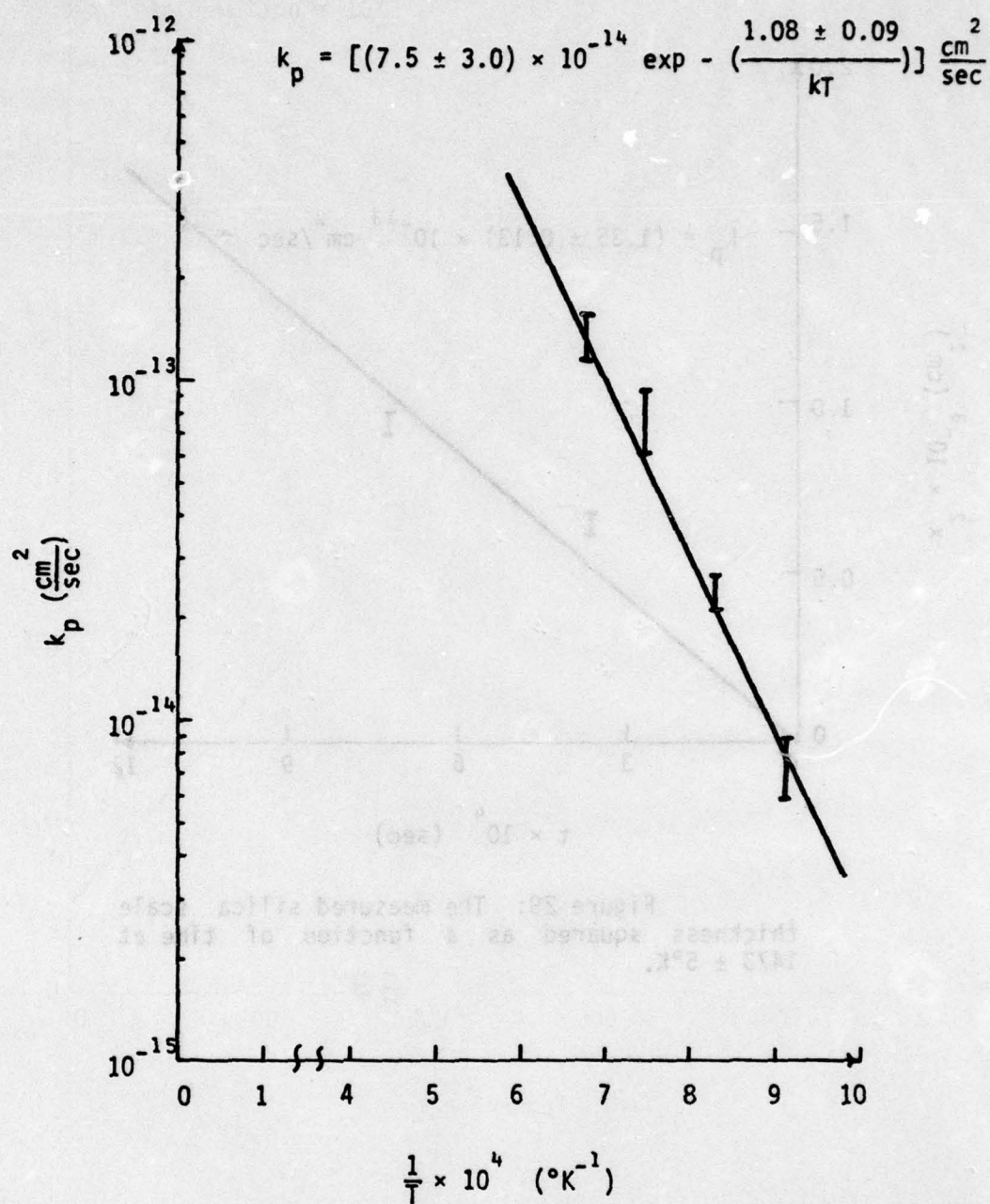


Figure 30: Graph of the parabolic rate constant as a function of reciprocal temperature.

parabolic oxidation of silicon in "dry" oxygen. (The maximum value of the activation energy is one half standard deviation lower than the lowest value reported in the literature). The silica scale thicknesses as measured in these experiments were found to be consistently thicker, by ten to twenty percent, than other reported measurements for the thermal oxidation of silicon. However, it was found that the scale thickness measured by this technique agreed with the estimated thickness corresponding to the interference color of the scale. The correlation of the measured thickness and estimated thickness, using the color chart given by Pliskin and Conrad (54) based on the VAMFO* technique for measuring thin films, is given in Table 4.

The reduced chi square values obtained for the kinetic sample fits used in the above calculations ranged from 1.3 to 3.0 and were based on only the MCA channels which contained non-zero data points. (The inclusion of MCA channels which are expected to have zero data points leads to better reduced chi square values; however, these are meaningless in determining the goodness of the fit. For example a spectrum containing forty non-zero data points may have a reduced chi square of 1.86, but if one includes 70 data points of which 30 are zero's the reduced chi square

* VAMFO stands for Variable Angle Monochromatic Fringe Observation.

TABLE 4. --Correlation of the measured thickness and the estimated thickness, using the color chart given by Pliskin and Conrad (54).

Sample Number	Oxidation Time (sec)	Temperature ($\pm 50^\circ\text{K}$)	Measured Thickness ($\pm 0.01\mu$)	Color Observed	Estimated Thickness (μ)
S-7-1	7.2×10^4	1473	0.97	Dull Yellow	0.95
S-7-2	7.2×10^4	1201	0.42	Rose	0.42
S-8-1	3.6×10^4	1473	0.81	Gray-Green	0.72-0.77
S-8-2	3.6×10^4	1200	0.33	Violet	0.30-0.31
S-9-1	1.08×10^5	1473	1.24	Pink	1.24
S-9-2	1.08×10^5	1200	0.52	Green	0.52
S-10-1	3.6×10^4	1337	0.66	Violet	0.63-0.68
S-10-2	3.6×10^4	1089	0.12	Blue	0.10-0.12
S-11-1	7.2×10^4	1337	0.75	Blue-Gray	0.68-0.72
S-11-2	7.2×10^4	1095	0.24	Yellow-Green	0.17-0.22

becomes 1.01). Figure 31 shows the computer predicted fit and data points for sample S-10-1 (0.66 micron thick) which was oxidized for 3.6×10^4 seconds (10 hours) at $1337 \pm 5^\circ\text{K}$ and analyzed using protons of incident energy 750 KeV. The calculated reduced chi square value for this fit is 1.86. It should be noted that the region of the spectra most difficult to fit is the region corresponding to the center of the scale. The program consistently predicted too low an alpha yield. The fact that the predicted alpha yield at the center of the scale is too low is an indication the stopping powers for protons and alphas assumed for silica may be in error. The effect of varying the proton and alpha stopping powers will be treated below.

The lower activation energy found in these experiments as well as the thicker thermal oxide scales can possibly be attributed to one or more of the following: (1) the water content of the oxygen, (2) the variation of the thermal oxide density with temperature of formation, and (3) an error in the stopping power for protons and alphas assumed for silica. Each of these will be discussed in turn.

It has been reported by Irene (17) that the parabolic activation energy can be varied by as much as 0.2 eV by changing the water vapor content of the ambient from less than one part per million to twenty-five parts per

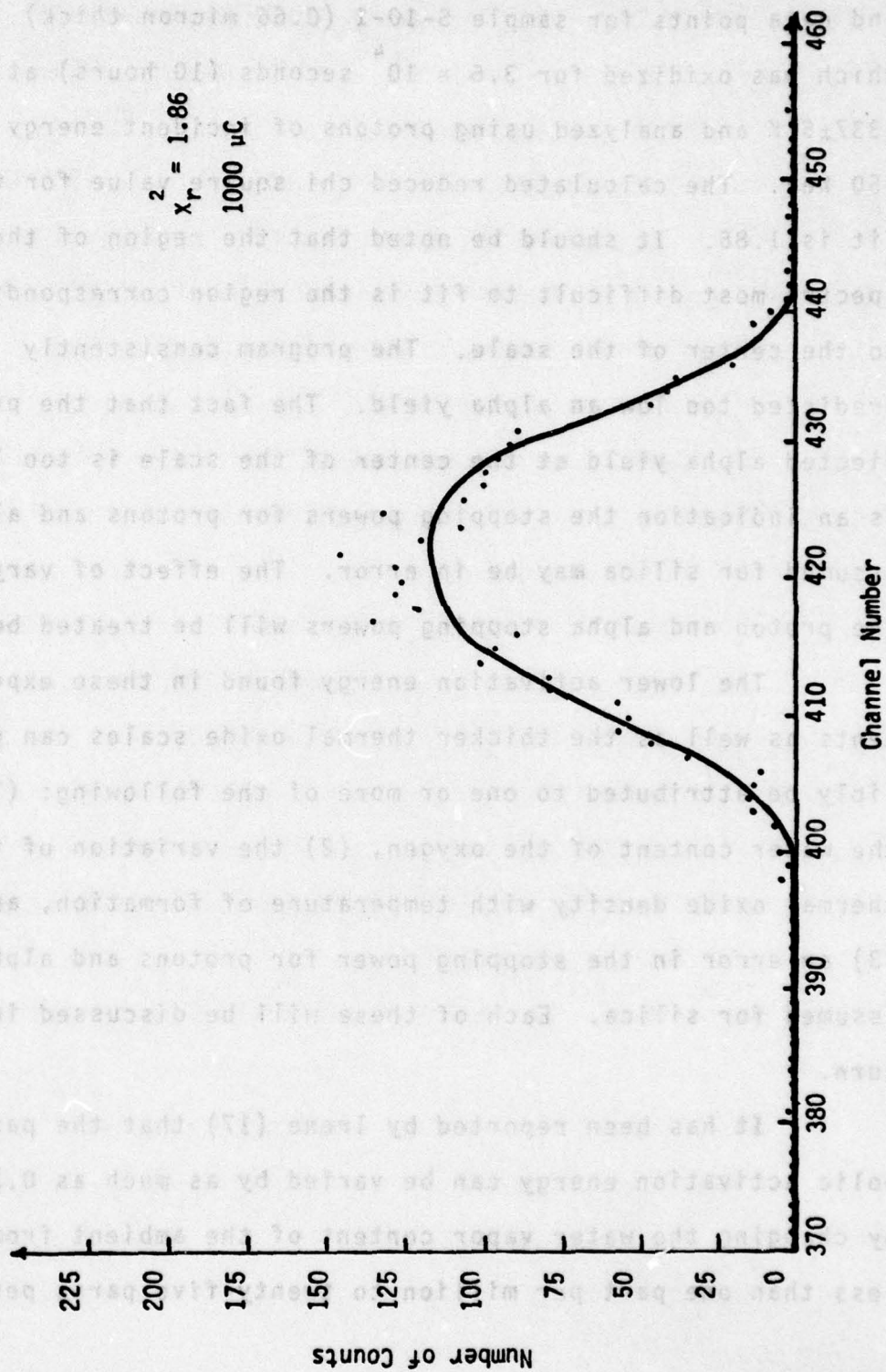


Figure 31: Fit of sample S-10-1, 0.66 μ thick, at an incident proton energy of 750 keV.

million. The oxygen introduced to the oxidation system has a dew point of 208°K which corresponds to a water vapor content of approximately thirteen parts per million. The water vapor content of the ambient oxygen can also be expected to increase during the course of the run due to the oxidation of any organic molecules in the system. Trace amounts of carbon dioxide, also a product of organic oxidation, have been found in the gas samples, indicating this to be a possible source of additional water vapor in the ambient. Although the dew point of the oxygen was not determined during the experiment, an estimate of the maximum water vapor content, based on the equilibrium values of the zeolite-water system, is 30 parts per million. Nevertheless, this amount of water vapor could effect the measured activation energy by as much as three percent.

It was assumed in these studies that the density of the thermal silica scale was 2.20 grams per cubic centimeter. However, Deal (15) has found that the density of the thermal silica layer formed at 1273°K is 2.27 grams per cubic centimeter and at 1473°K is 2.15 grams per cubic centimeter. Since the stopping power of a particle in matter is expressed in units of energy-area per unit mass, a variation in thermal oxide density would therefore effect the range-energy curve for the particle. This variation in density could introduce a systematic error in the scale thickness of as much as four percent at each temperature.

The elemental stopping powers used to calculate the stopping power of silica is a third possible source of systematic error. The elemental stopping powers as given by Williamson, Boujot, and Picard (55) can be considered accurate to no more than ten percent. An increase in proton stopping power would tend to shift the energy of alphas created below the surface to lower energies while an increase in alpha stopping power would tend to shift the energy of alphas created below the surface to lower energies. It should also be noted that changing the proton stopping powers will not effect the general shape of the spectra, but will change the total alpha yield. This is because the only term effected in the equation for calculating the alpha yield (Equation 37) is the differential cross section in a given depth interval. A change in alpha stopping power will not effect the overall alpha yield (this assumes that all alpha particles created have enough energy to reach the detector and be recorded in the MCA), but will change the spectral shape due to the rate at which the alpha particles lose energy as they traverse the sample. Figures 32-37 show the effect of varying the proton and alpha stopping powers, by plus or minus ten percent either singularly or simultaneously, on the calculated alpha spectra for a silica scale of uniform oxygen-18 concentration 0.66 micron thick.

It can be seen from Figures 32-37 that the predicted alpha yield at the center of the scale can be increased by

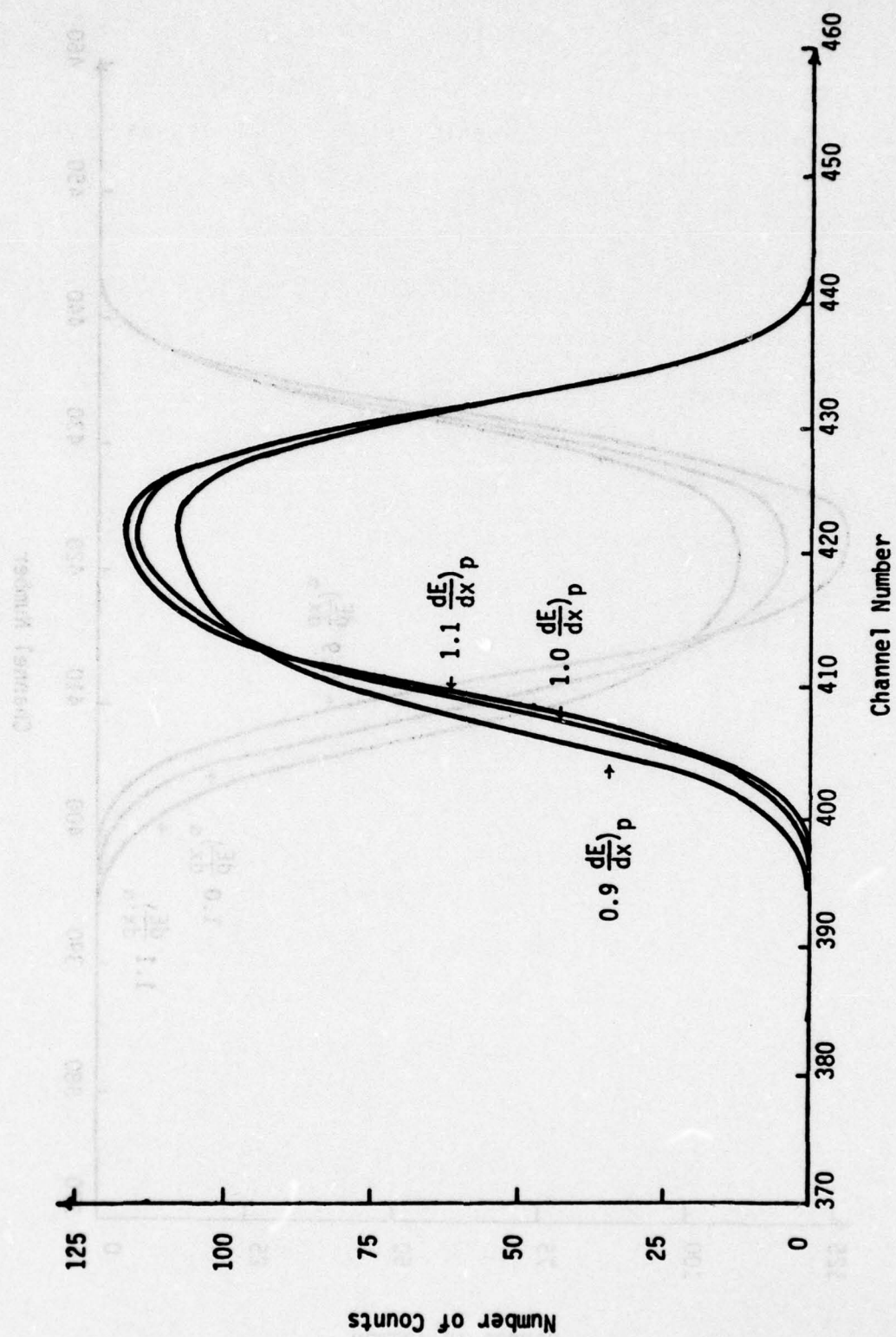


Figure 32: The effect of changing the proton stopping power by $\pm 10\%$.

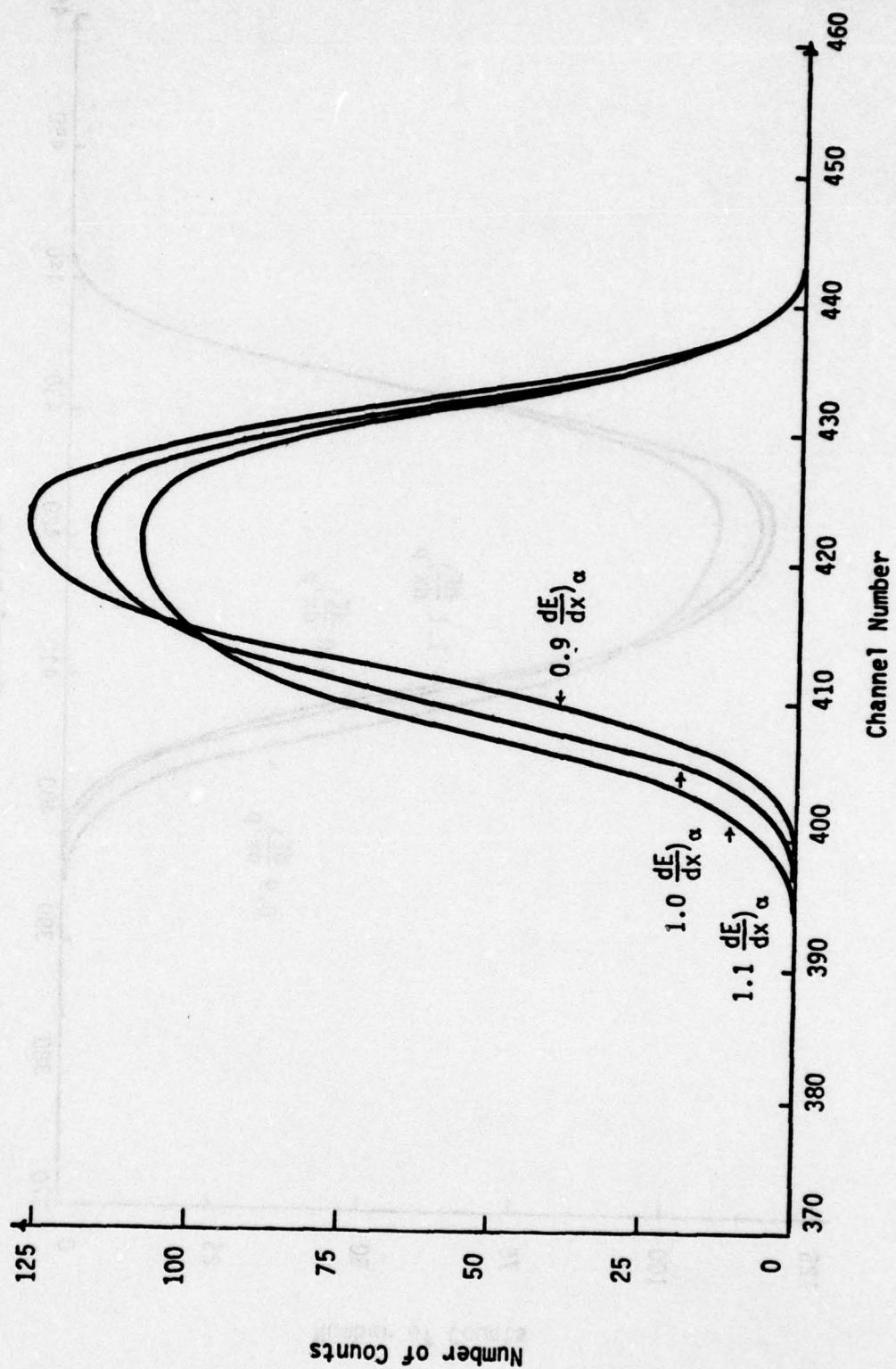


Figure 33: The effect of changing the alpha stopping power by $\pm 10\%$.

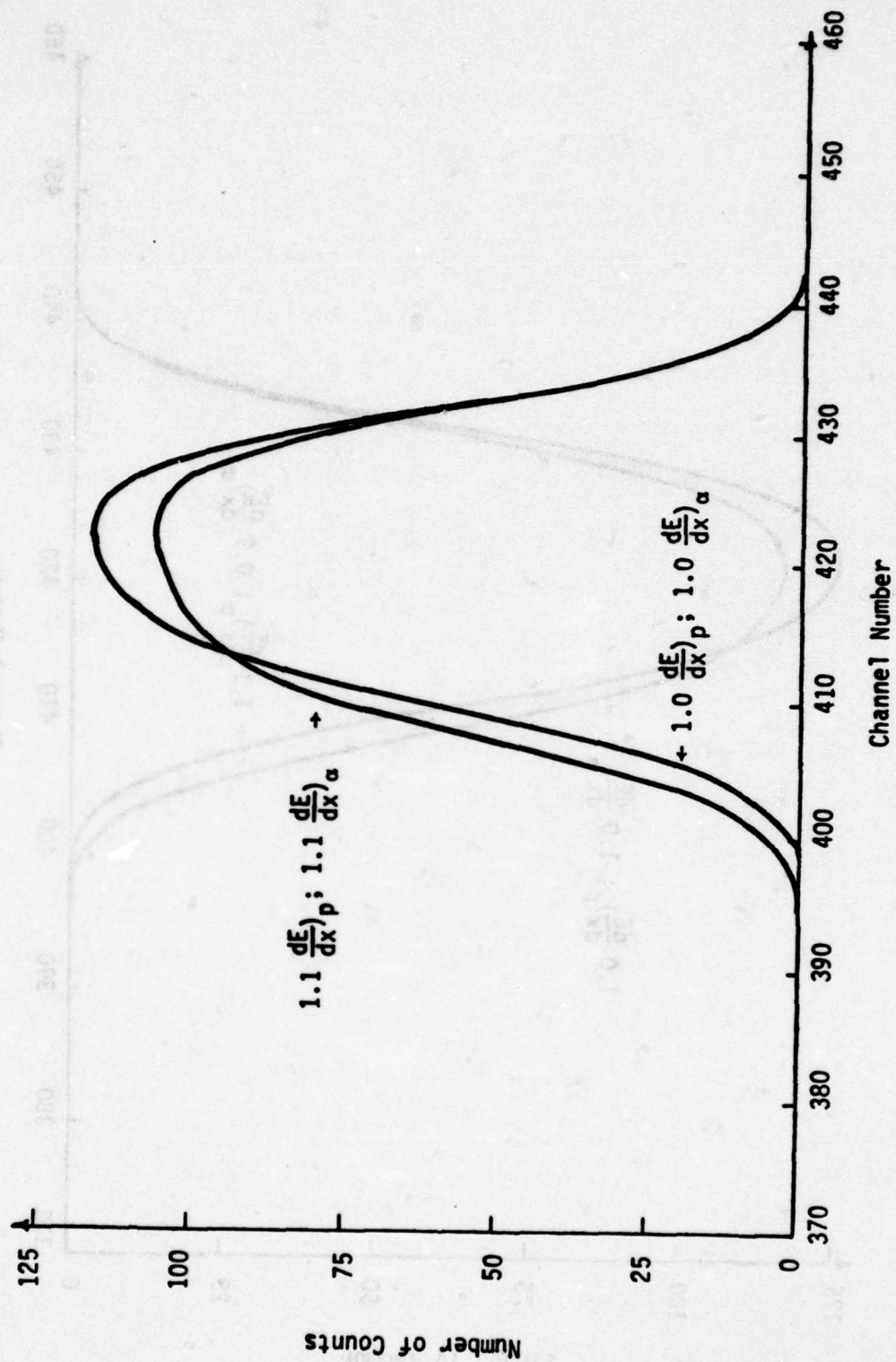


Figure 34: The effect of increasing both the proton and alpha stopping powers by 10%.

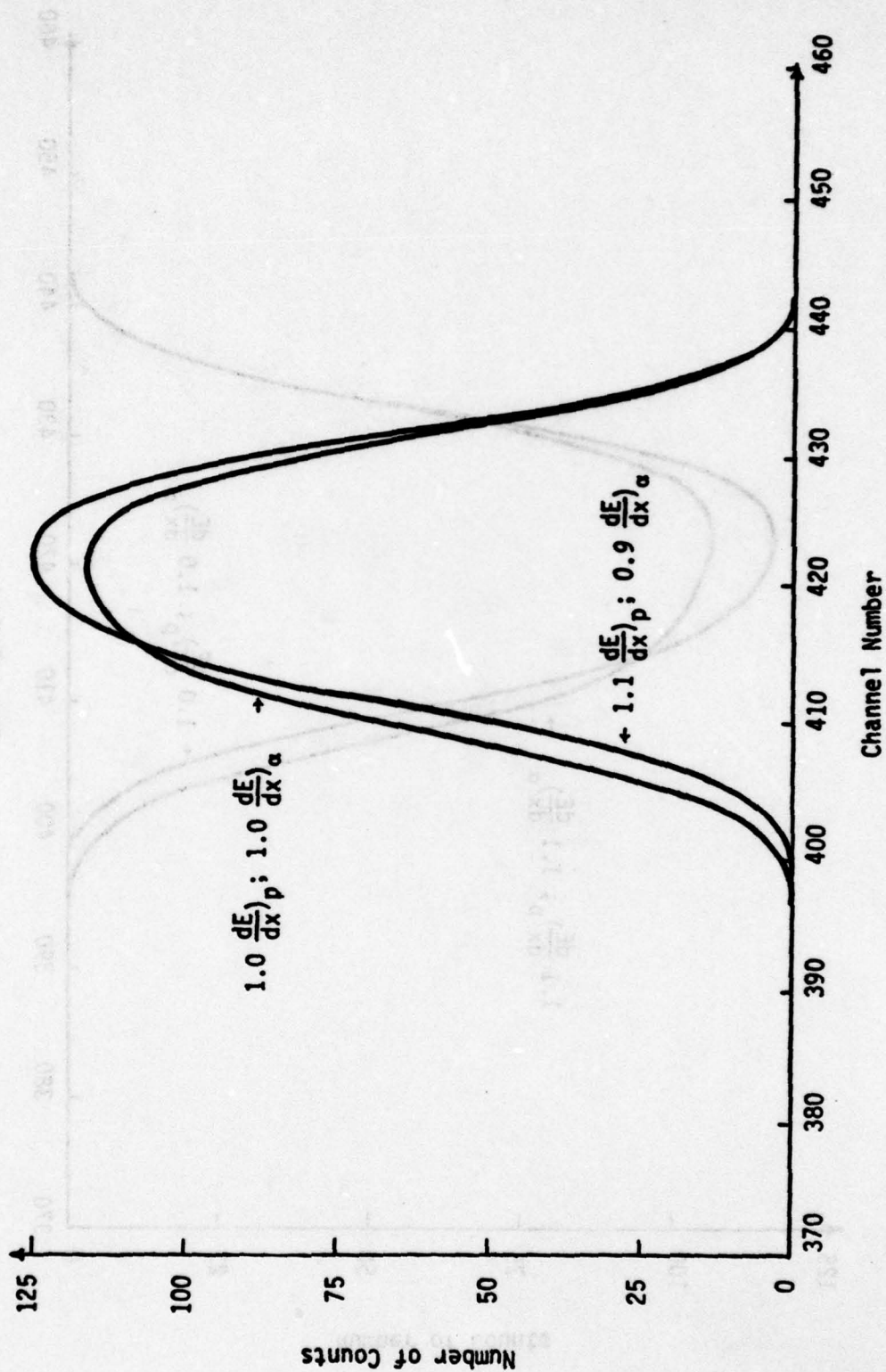


Figure 35: The effect of increasing the proton stopping power by 10% while decreasing the alpha stopping power by 10%.

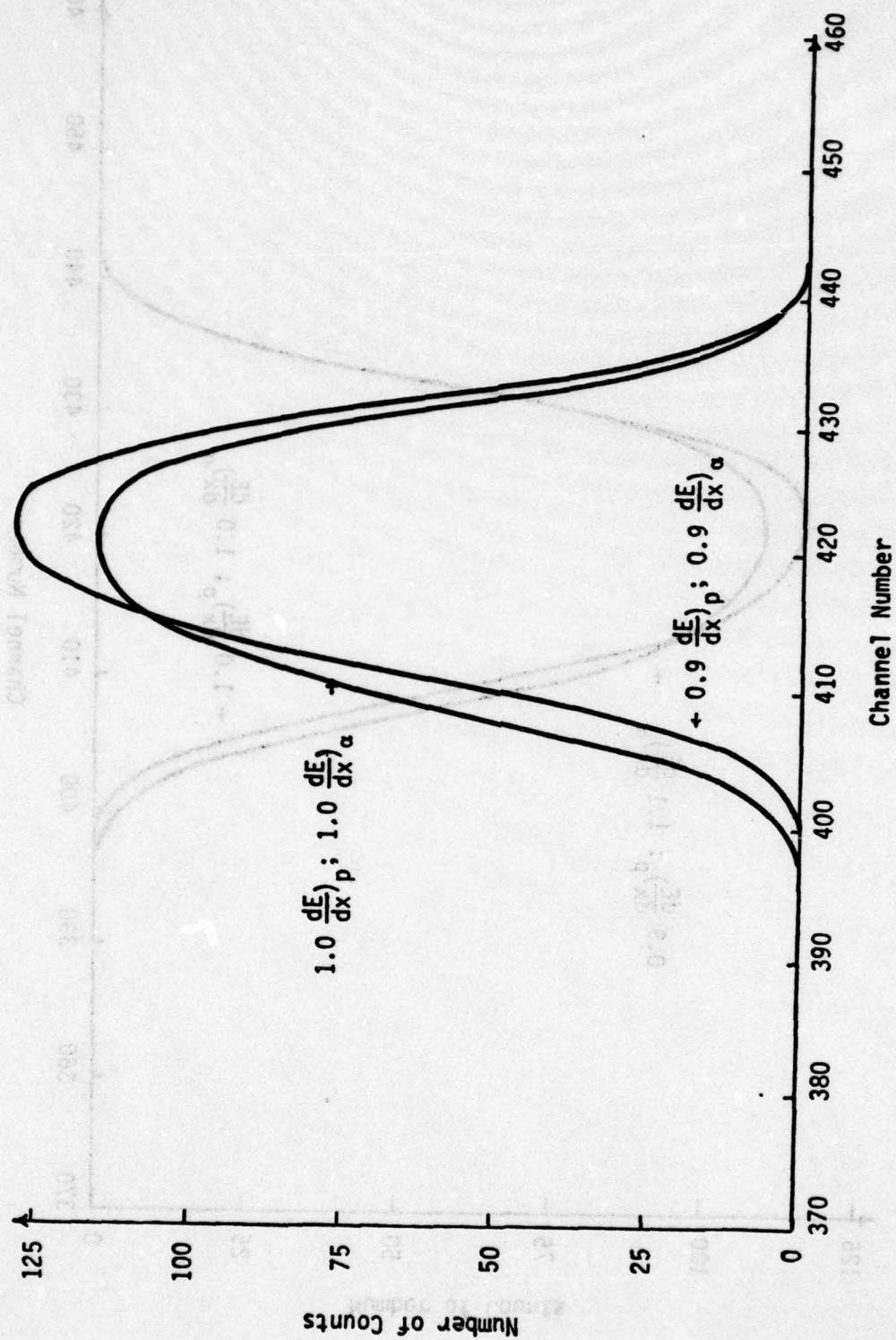


Figure 36: The effect of decreasing both the proton and alpha stopping powers by 10%.

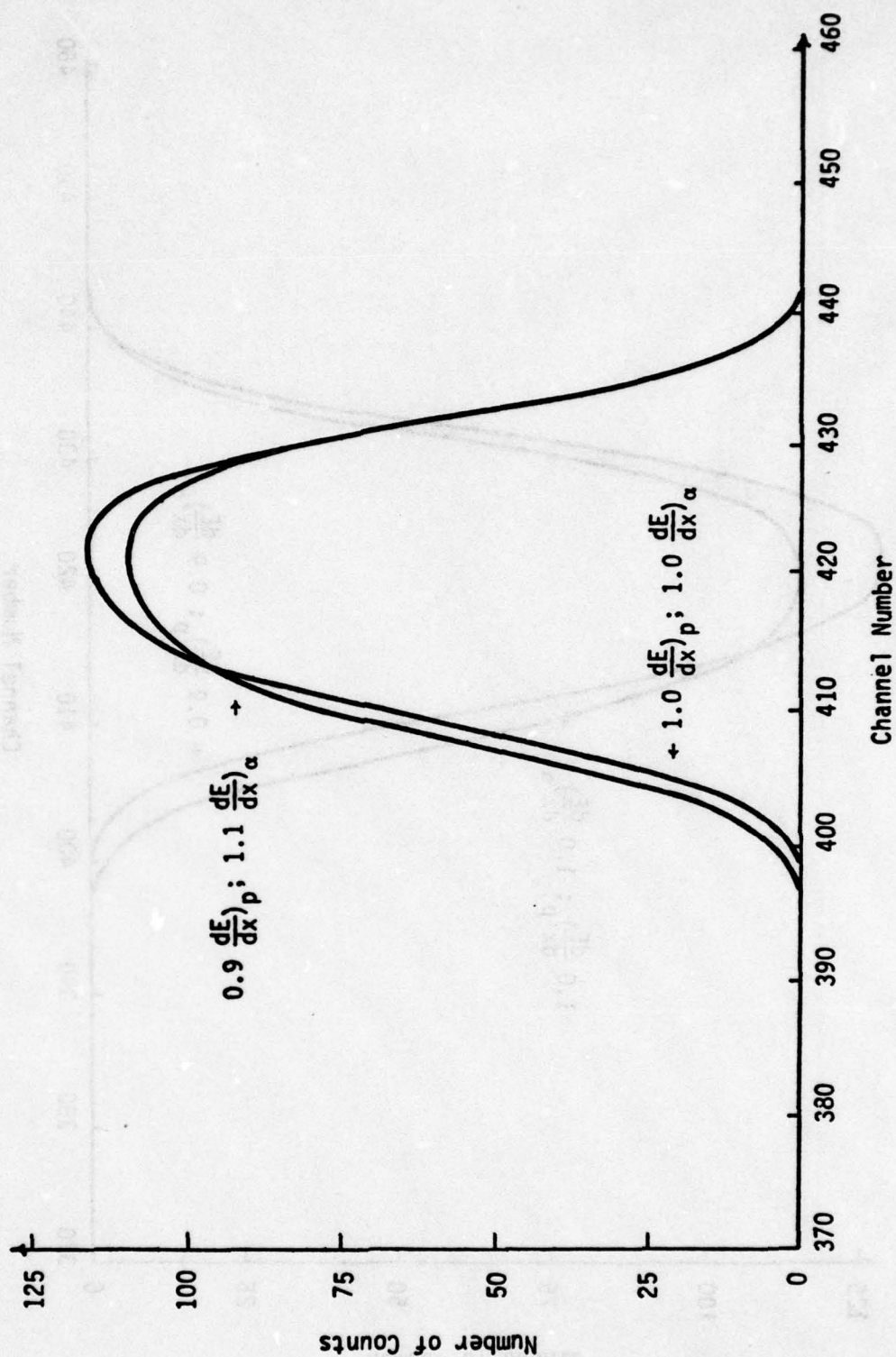


Figure 37: The effect of decreasing the proton stopping power by 10% while increasing the alpha stopping power by 10%.

one of the following: (1) increasing the proton stopping power, (2) decreasing the alpha stopping power, (3) increasing the proton stopping power while decreasing the alpha stopping power, or (4) decreasing both the proton and alpha stopping powers. In order to determine how the stopping powers should be varied to improve the spectral fits it is necessary to have a series of silica scales of known thickness and of uniform oxygen-18 distribution. These samples should then be run at several incident proton energies where there are large variations in cross section with incident proton energy (such as the 637 KeV resonance). This will give a series of alpha spectra, each having a different alpha yield and different spectral shape. Since the thickness, oxygen 18 concentration, and cross section are known it will be possible to fit these spectra by varying only the proton and alpha stopping powers. Computer calculation shows that a variation of up to ten percent in proton and/or alpha stopping powers can cause an error of approximately ten percent in the measured scale thickness.

6.2 "Marker" Experiments

In the "marker" experiments it was found that the position of the oxygen-18 "marker" varied with oxidation temperature. In the temperature range $1171 \pm 5^\circ\text{K}$ to $1473 \pm 5^\circ\text{K}$ the position of the isotope used in the initial oxidation

moved from the silica-oxygen interface to the silicon-silica interface with increasing oxidation temperature. The oxygen-18 concentration versus depth profiles were derived using a trial and error deconvolution procedure. Each spectrum was initially fit assuming a silica scale of uniform oxygen-18 concentration (20%) and one micron thick. The spectra corresponding to this oxygen-18 distribution was then compared with the experimental data. Figure 38 shows a comparison of the experimental data for sample S-5-3 analyzed at 750 KeV and predicted alpha spectra assuming a uniform oxygen-18 distribution.

Knowing the incident proton energy, the kinematics of the $^{18}\text{O}(p,\alpha)^{15}\text{N}$ reaction (Appendix 1), the range-energy curves for protons and alphas on silica (Appendix 1), and the MCA calibration, it is a simple procedure to determine what depth each channel of the MCA corresponds to. If the experimental and predicted spectra were ideal (i.e. no spreading occurred) then the number of counts in a given channel of the experimental data divided by the number of counts in the same channel of the assumed spectra times the concentration of oxygen-18 assumed to be at the depth corresponding to the channel would be the concentration at that depth. Since the spectra are spread, this value can only be used as a first approximation to the oxygen-18 concentration versus depth profile. With this approximation it was possible to obtain an improved concentration versus depth

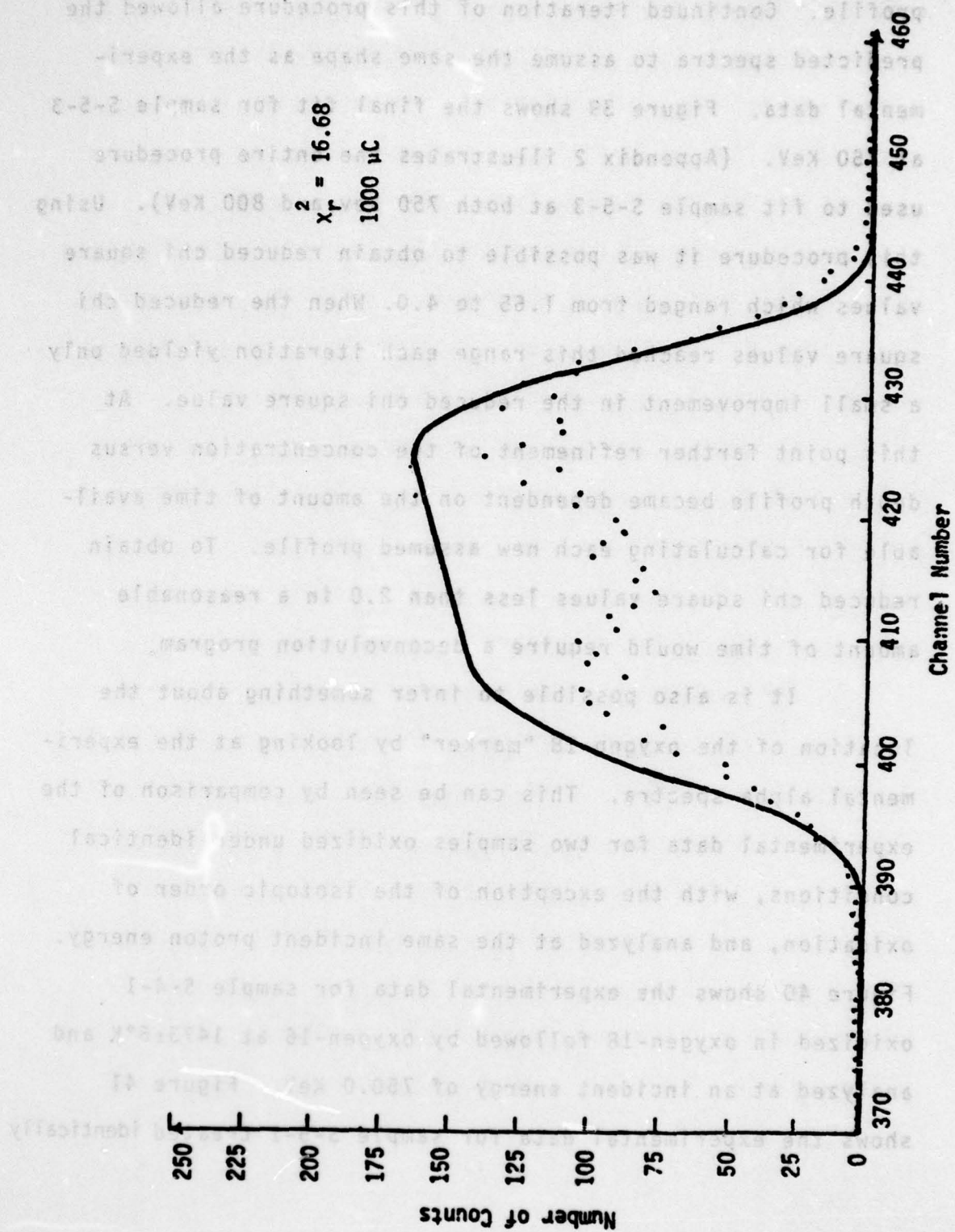


Figure 38: Initial fit of sample S-5-3 at an incident proton energy of 750 KeV.

profile. Continued iteration of this procedure allowed the predicted spectra to assume the same shape as the experimental data. Figure 39 shows the final fit for sample S-5-3 at 750 KeV. (Appendix 2 illustrates the entire procedure used to fit sample S-5-3 at both 750 KeV and 800 KeV). Using this procedure it was possible to obtain reduced chi square values which ranged from 1.65 to 4.0. When the reduced chi square values reached this range each iteration yielded only a small improvement in the reduced chi square value. At this point farther refinement of the concentration versus depth profile became dependent on the amount of time available for calculating each new assumed profile. To obtain reduced chi square values less than 2.0 in a reasonable amount of time would require a deconvolution program.

It is also possible to infer something about the location of the oxygen-18 "marker" by looking at the experimental alpha spectra. This can be seen by comparison of the experimental data for two samples oxidized under identical conditions, with the exception of the isotopic order of oxidation, and analyzed at the same incident proton energy. Figure 40 shows the experimental data for sample S-4-1 oxidized in oxygen-18 followed by oxygen-16 at $1473 \pm 5^\circ\text{K}$ and analyzed at an incident energy of 750.0 KeV. Figure 41 shows the experimental data for sample S-5-1 treated identically

bioRxiv preprint doi: <https://doi.org/10.1101/123456>; this version posted January 1, 2018. The copyright holder for this preprint (which was not certified by peer review) is the author/funder, who has granted bioRxiv a license to display the preprint in perpetuity. It is made available under aCC-BY-NC-ND 4.0 International license.

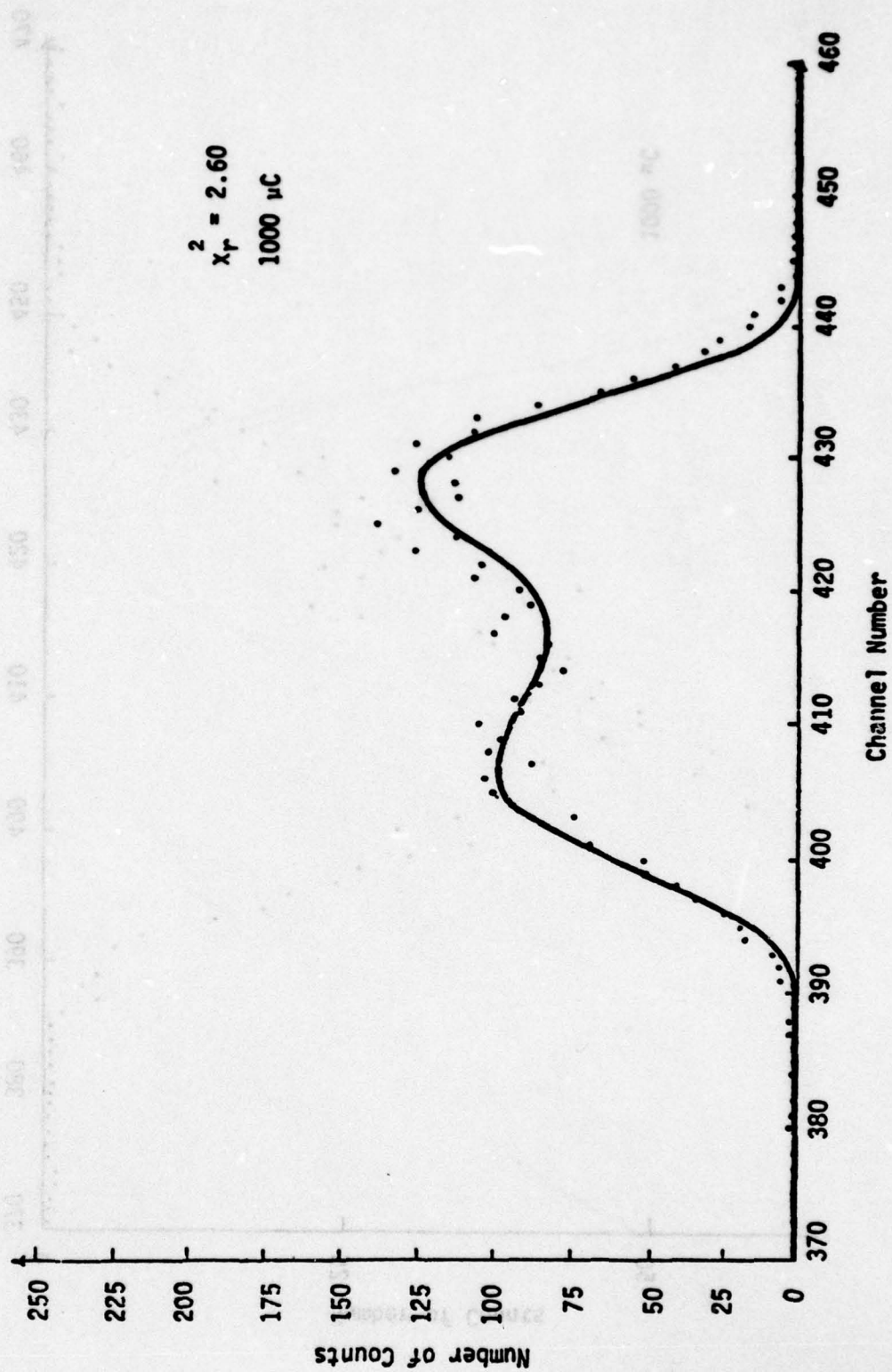


Figure 39: Final fit of sample S-5-3 at an incident proton energy of 750 KeV.

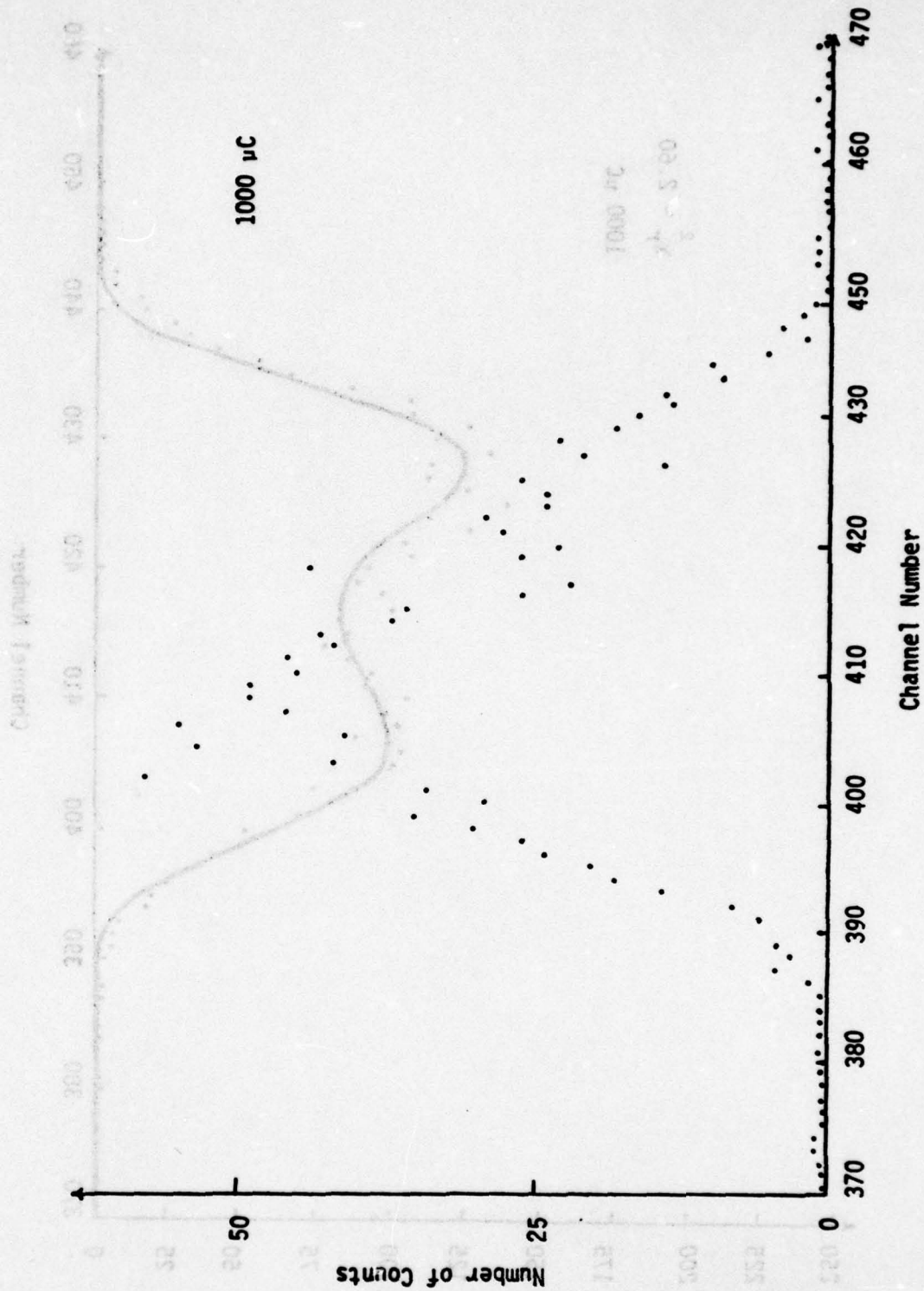


Figure 40: The experimental alpha spectrum for sample S-4-1 at an incident proton energy of 750 KeV.

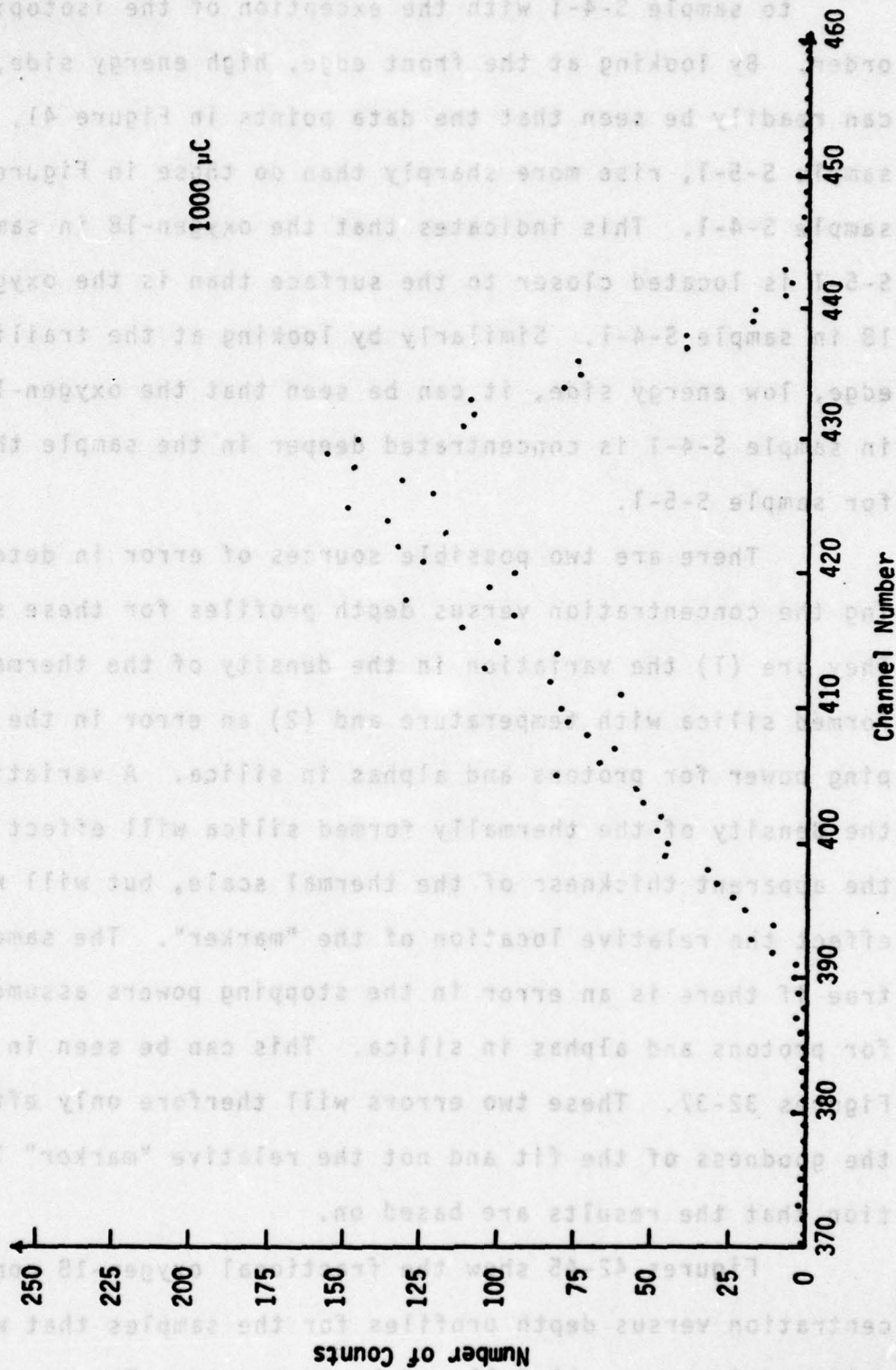


Figure 41: The experimental alpha spectrum for sample S-5-1 at an incident proton energy of 750 KeV.

to sample S-4-1 with the exception of the isotopic order. By looking at the front edge, high energy side, it can readily be seen that the data points in Figure 41, sample S-5-1, rise more sharply than do those in Figure 40, sample S-4-1. This indicates that the oxygen-18 in sample S-5-1 is located closer to the surface than is the oxygen-18 in sample S-4-1. Similarly by looking at the trailing edge, low energy side, it can be seen that the oxygen-18 in sample S-4-1 is concentrated deeper in the sample than for sample S-5-1.

There are two possible sources of error in determining the concentration versus depth profiles for these samples. They are (1) the variation in the density of the thermally formed silica with temperature and (2) an error in the stopping power for protons and alphas in silica. A variation in the density of the thermally formed silica will effect only the apparent thickness of the thermal scale, but will not effect the relative location of the "marker". The same is true if there is an error in the stopping powers assumed for protons and alphas in silica. This can be seen in Figures 32-37. These two errors will therefore only effect the goodness of the fit and not the relative "marker" location that the results are based on.

Figures 42-45 show the fractional oxygen-18 concentration versus depth profiles for the samples that were oxidized in oxygen-18 followed by oxygen-16. The concentration

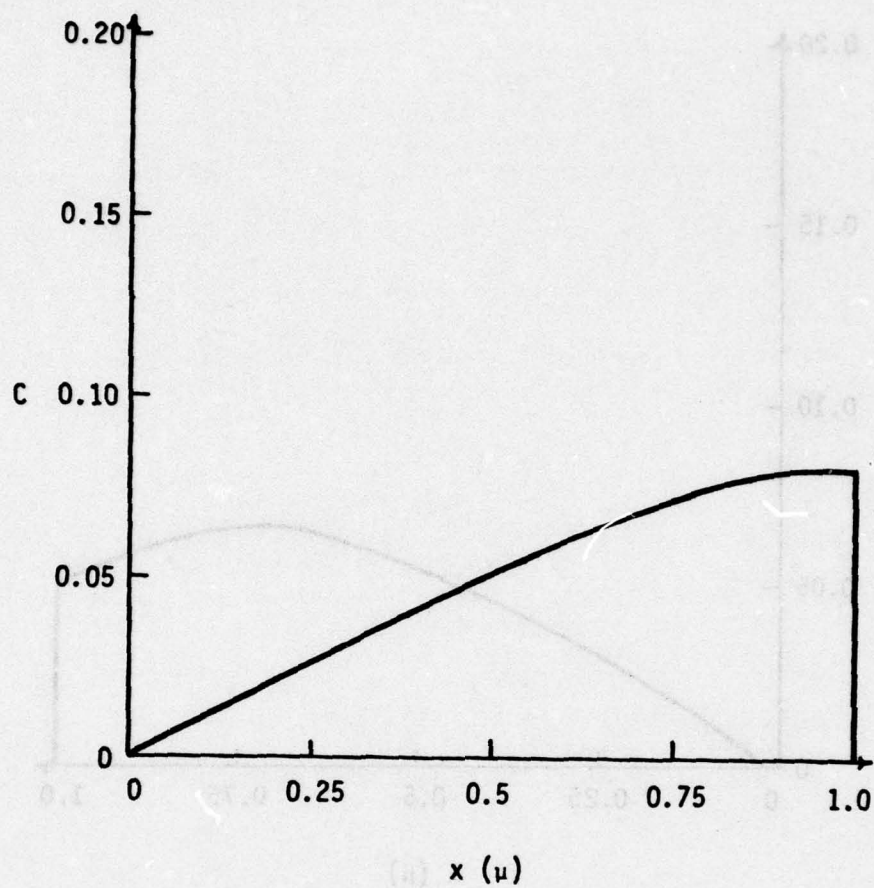


Figure 42: Concentration versus depth profile for sample S-4-1 oxidized at $1473 \pm 5^\circ\text{K}$.

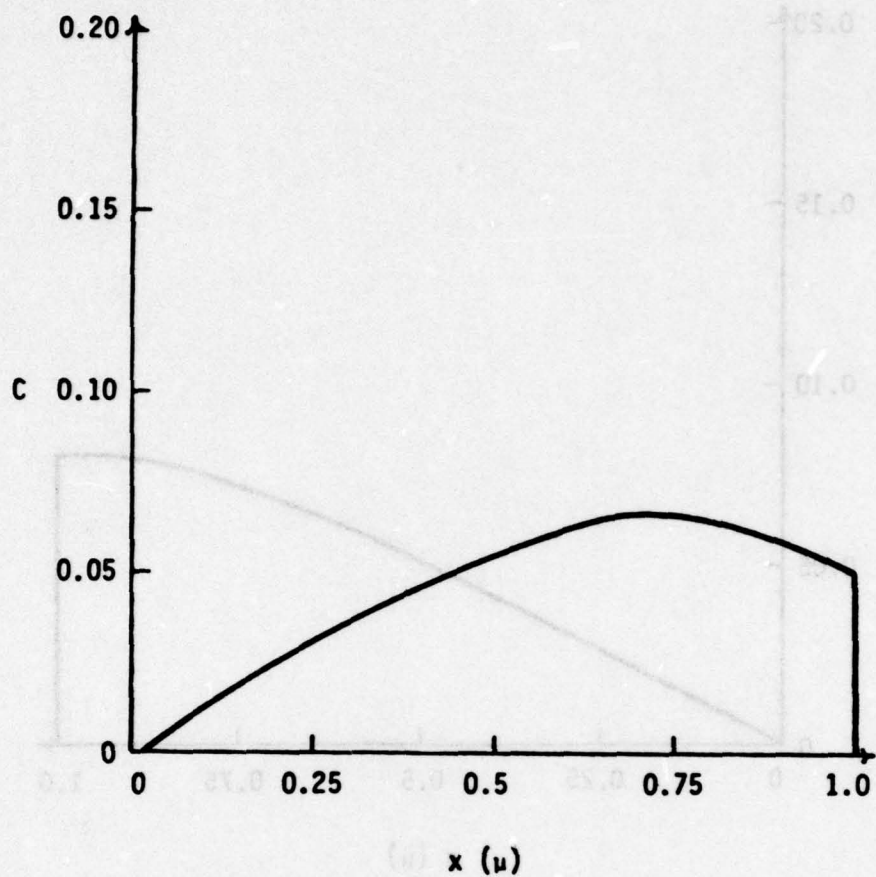


Figure 43: Concentration versus depth profile for sample S-4-2 oxidized at $1412 \pm 5^\circ\text{K}$.

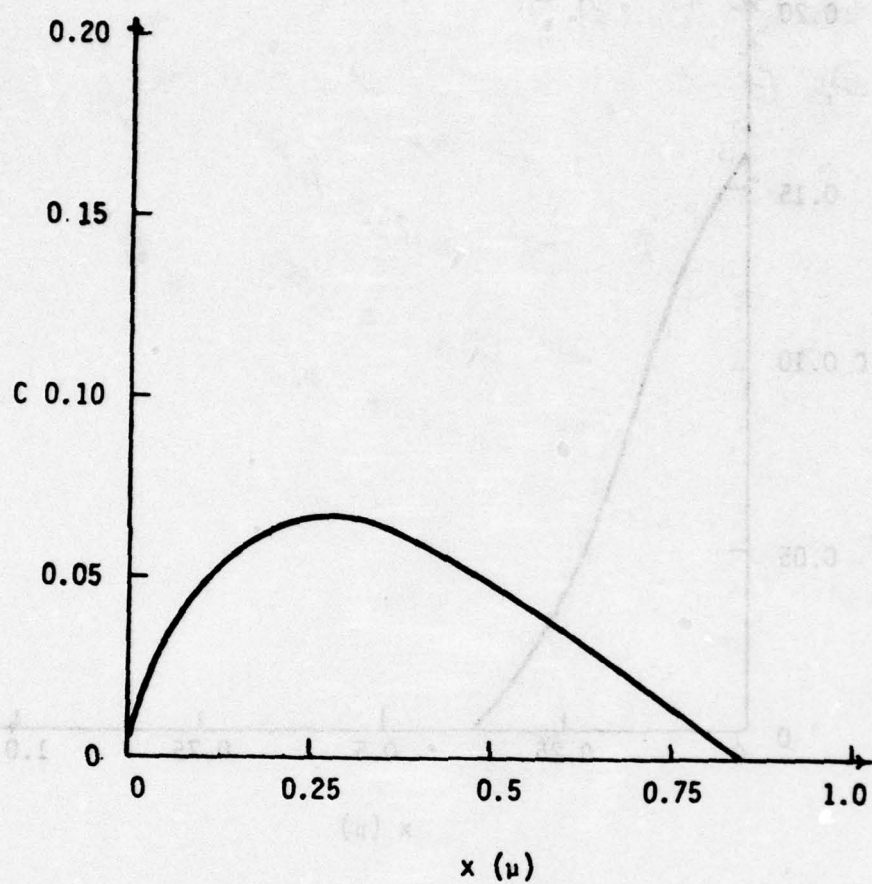


Figure 44: Concentration versus depth profile for sample S-4-3 oxidized at $1295 \pm 5^\circ\text{K}$.

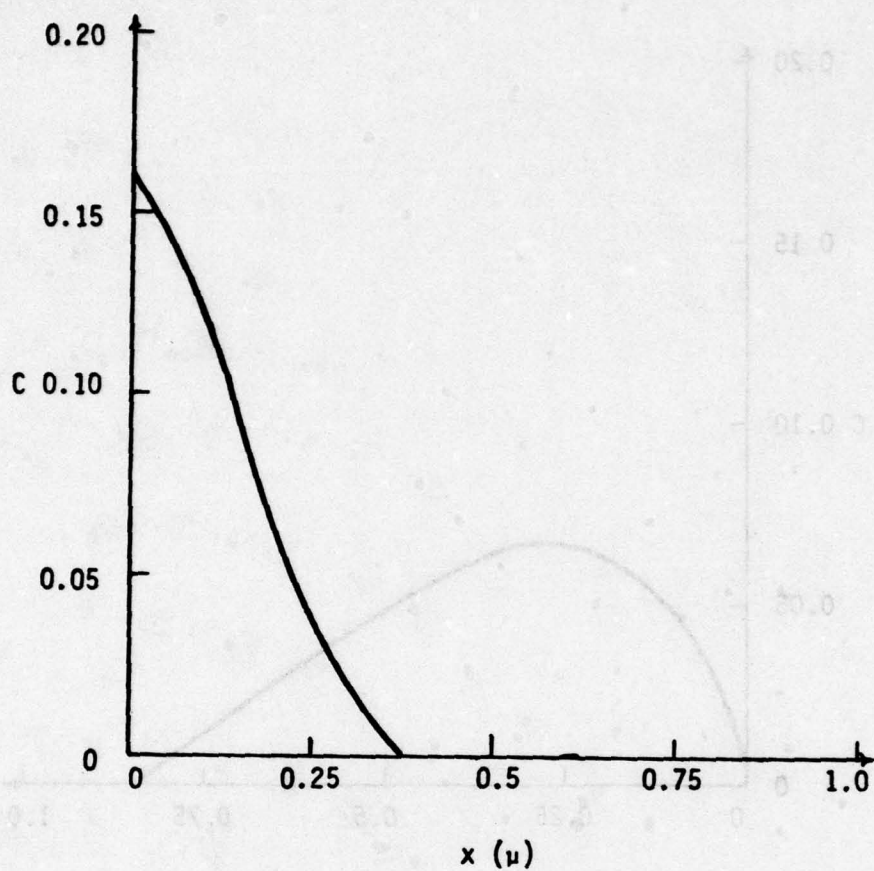


Figure 45: Concentration versus depth profile for sample S-4-4 oxidized at $1171 \pm 5^\circ\text{K}$.

versus depth profiles for the samples where the isotopic order was reversed are not shown since they are simply identical profiles with the isotopes reversed and the isotopic order of these spectra corresponds to the isotopic order used in Chapter III.

Figure 42 shows the oxygen-18 concentration versus depth profile for a sample oxidized at $1473 \pm 5^\circ\text{K}$. The fact that the oxygen-18 "marker" is located at the silica-silicon interface, (Case II), indicates that the rate controlling mechanism for the thermal oxidation of silicon at this temperature is either the transport of molecular oxygen with the rate of permeation less than the rate of exchange (see Section 3.2.3) or the transport of an ionic species (see Sections 3.3.1 and 3.3.2).

Figure 43 shows the concentration versus depth profile for a sample oxidized at $1412 \pm 5^\circ\text{K}$. Here the shape and position of the oxygen-18 "marker" corresponds to a situation intermediate to Cases I and II (see Section 3.2.4). The rate controlling mechanism at this temperature is thus interpreted to be the transport of molecular oxygen, with the rate of permeation equal to or slightly less than the rate of exchange.

Figure 44 again shows the oxygen-18 concentration versus depth profile which is expected if the rate controlling mechanism is the transport of molecular oxygen with the kinetics of the permeation and exchange reaction roughly equal

(see Section 3.2.4). This sample was oxidized at $1295 \pm 5^\circ\text{K}$.

The profile shown in Figure 45 is for the sample oxidized at the lowest temperature, $1171 \pm 5^\circ\text{K}$. At this temperature the oxygen-18 "marker" was found at the silica-oxygen interface, (Case I), indicating the rate controlling mechanism at this temperature was the transport of molecular oxygen with the rate of permeation much greater than the rate of exchange (see Section 3.2.2).

The fact that the oxygen-18 "marker" position is a function of the oxidizing temperature rules out the possibility that the rate controlling process in the thermal oxidation of silicon is the transport of either silicon or oxygen ions. If the reaction were controlled by the transport of an ionic species the oxygen-18 "marker" would always be located at the silica-silicon interface (see Sections 3.3.1 and 3.3.2). The motion of the "marker" with temperature indicates that two processes are involved in the thermal oxidation reaction, the kinetics of each having different temperature dependences. These studies indicate that the two processes involved are the permeation of molecular oxygen through the adherent silica scale and the exchange of the permeating oxygen with the network oxygen. This study also suggests that the kinetics of exchange are roughly equal to the kinetics of permeation at 1323°K and exceed the permeation kinetics at higher temperatures.

The results of these mechanistic experiments, when combined with the pressure dependence reported by other investigators (4,22)- the parabolic rate constant being directly proportional to the oxygen partial pressure- leads to the same conclusion arrived at by Ligenza and Spitzer (22), i.e. the rate controlling process in the thermal oxidation of silicon is the diffusion of molecular oxygen through the adherent silica scale with appreciable isotopic exchange occurring between the diffusing oxygen and the network oxygen.

According to Meek (26) oxygen diffusion in silica involves two processes, as determined in these studies, a transport process and an exchange process. If the mechanism for the thermal oxidation of silicon (the transport of molecular oxygen through the adherent silica scale) presented here is to be consistent with Meek's argument it should be possible to calculate the diffusivity of oxygen in thermally grown silica using the parabolic rate constant determined in the kinetic studies. This value should be approximately equal to the diffusivity measured by Norton in his permeation experiment. The diffusivity can be related to the parabolic rate constant by the following equation (3,4):

$$D = \frac{k_p C''}{2C'} \quad (43)$$

where C'' is the concentration of oxygen incorporated in the silica scale (2.2×10^{22} molecules / cm^3) (26) and C' is the

solubility of oxygen in silica (5.6×10^{16} molecules / cm^3) (26). Using these values one obtains the following expression for the diffusivity:

$$D = [1.47 \times 10^{-4} \exp - (\frac{1.08\text{eV}}{kT})] \frac{\text{cm}^2}{\text{sec}} \quad (44)$$

This calculated value is within experimental error of Norton's calculated diffusivity (21):

$$D = [2.88 \times 10^{-4} \exp - (\frac{1.17\text{eV}}{kT})] \frac{\text{cm}^2}{\text{sec}} \quad (45)$$

Of even greater interest is the fact that the final scales in the successive isotopic oxidation studies should be composed of ten percent oxygen-18, while it is found that only twenty-five to fifty percent of the oxygen-18 incorporated in the silica scale during the initial oxidation remains at the end of the experiment (see Figures 42-45). This decrease in oxygen-18 concentration must occur by diffusion of oxygen-18 out of the silica scale at the silica-oxygen interface. The oxygen-18 cannot be lost by any other diffusion of oxygen in any other direction since this oxygen-18 would be located and measured during the proton activation analysis. Diffusion of oxygen across the silica-oxygen interface requires diffusion of oxygen up an oxygen concentration gradient but down an isotopic concentration gradient. Although it is not possible to calculate a diffusion coefficient from the "marker" experimental data due

to the qualitateness of the fits, it is possible to make some approximate calculation. Shewmon (56) gives the following equation for the degassing of thin metal films when the ratio of the average final composition of a sample to its average initial composition is less than 0.8:

$$\frac{\text{Average Final Composition}}{\text{Average Initial Composition}} = \frac{8}{\pi} \exp - \left(\frac{t \pi^2 D}{y^2} \right) \quad (46)$$

Using this equation it is possible to calculate a range of diffusivities corresponding to the amount of oxygen-18 remaining in the silica after the second oxidation. The calculated diffusivities fall in the range 10^{-14} to 10^{-13} cm^2/sec for the variation in oxygen-18 concentration observed. This range of diffusivities is in agreement with the diffusivity measured by Williams (20) in his isotopic exchange experiments:

$$D = [2.0 \times 10^{-9} \exp - \left(\frac{1.26 \text{ eV}}{kT} \right)] \frac{\text{cm}^2}{\text{sec}} \quad (47)$$

It should also be noted that less oxygen-18 remains in the silica scale formed at the lower temperature. This can possibly be attributed to the fact that at low temperatures the oxygen-18 remains peaked at the silica-oxygen interface giving a shorter diffusion distance for the removal of oxygen-18.

These "marker" studies therefore indicate that the diffusivity of oxygen in silica governing the transport of

oxygen is that value measured by Norton (20) in his permeation experiments. The transport of oxygen therefore occurs by oxygen dissolving in the silica at the silica-oxygen interface and diffusing through the oxide. An exchange also occurs between the diffusing oxygen and the network oxygen. The exchange probably occurs by dissolved oxygen molecules entering vacancies which exist in the silica scale. At these sites broken silicon-to-oxygen bonds will exist which makes it possible for one of the oxygens to become part of the oxide. It is equally likely that an oxygen which is bonded to only one silicon can bond to the single oxygen atom, which has lost an oxygen atom to the scale, and continue diffusing through the scale. This model is consistent with the model proposed by Meek (26) for oxygen diffusion in vitreous silica.

SECTION VII

SUGGESTIONS FOR FUTURE WORK

7.1 Kinetic Oxidations

It is felt that since the thermal oxide scales found in these investigations are thicker than others reported in the literature a series of experiments should be undertaken to investigate the effect of water vapor content of the ambient on the parabolic rate constant. It is also felt that the temperature range and time of oxidation should be extended in order to better determine the exact kinetics of the reaction.

7.2 Mechanistic Oxidations

The mechanistic experiment has shown that the relative rate of exchange becomes approximately equal to the rate of permeation around 1323°K, and then becomes more rapid than the rate of permeation at higher temperatures. This result is based on runs at only four temperatures. It is felt that the number of temperatures investigated should be increased to allow better determination of the relative exchange and permeation rates.

Along the same line it is felt that a numerical solution, and possibly an analytical solution, exists to predict the oxygen-18 distributions expected in tracer experiments where the distribution will be a function of exchange rate and permeation rate.

7.3 Experimental Procedure

The construction of an oxidation apparatus that can accommodate samples up to 1.5 centimeters square will be invaluable. (This apparatus is under construction). The larger samples will allow the use of ellipsometry as well as proton activation techniques.

SECTION VII
SUGGESTIONS FOR FUTURE WORK

In future studies where it is possible to produce thin films of known thickness and uniform oxygen-18 concentration the stopping powers for protons and alphas in the material should be checked. This experimental procedure, which has been outlined in Chapter VI, is straight forward if one works in a region of the cross section that is rapidly changing (i.e. the 637 KeV resonance) to give large changes in alpha flux for small changes in energy.

7.4 Data Reduction

A deconvolution program for the analysis of alpha spectra from oxidation and diffusion runs would greatly decrease the amount of time required to analyze each spectrum. The trial and error convolution procedure presently used is quite laborious whereas a deconvolution program would give the concentration versus depth profile directly.

Depth in microns	0.05	0.04	0.03	0.02	0.01
------------------------	------	------	------	------	------

APPENDIX A

RANGE-ENERGY CURVES FOR PROTONS AND ALPHAS ON Ta_2O_5 , ZnF_2 , AND
 SiO_2 AND KINEMATICS OF THE $^{18}O(p,\alpha)^{15}N$, $^{19}F(p,\alpha)^{16}O$, AND
 $^{19}F(p,\alpha_1)^{16}O^*$ NUCLEAR REACTIONS

0.000	1000.00000	999.99997	999.99994	999.99991	999.99988
0.001	999.99997	999.99994	999.99991	999.99988	999.99985
0.002	999.99985	999.99982	999.99979	999.99976	999.99973
0.003	999.99973	999.99970	999.99967	999.99964	999.99961
0.004	999.99961	999.99958	999.99955	999.99952	999.99949
0.005	999.99949	999.99946	999.99943	999.99940	999.99937
0.006	999.99937	999.99934	999.99931	999.99928	999.99925
0.007	999.99925	999.99922	999.99919	999.99916	999.99913
0.008	999.99913	999.99910	999.99907	999.99904	999.99901
0.009	999.99901	999.99898	999.99895	999.99892	999.99889
0.010	999.99889	999.99886	999.99883	999.99880	999.99877
0.011	999.99877	999.99874	999.99871	999.99868	999.99865
0.012	999.99865	999.99862	999.99859	999.99856	999.99853
0.013	999.99853	999.99850	999.99847	999.99844	999.99841
0.014	999.99841	999.99838	999.99835	999.99832	999.99829
0.015	999.99829	999.99826	999.99823	999.99820	999.99817
0.016	999.99817	999.99814	999.99811	999.99808	999.99805
0.017	999.99805	999.99802	999.99799	999.99796	999.99793
0.018	999.99793	999.99790	999.99787	999.99784	999.99781
0.019	999.99781	999.99778	999.99775	999.99772	999.99769
0.020	999.99769	999.99766	999.99763	999.99760	999.99757
0.021	999.99757	999.99754	999.99751	999.99748	999.99745
0.022	999.99745	999.99742	999.99739	999.99736	999.99733
0.023	999.99733	999.99730	999.99727	999.99724	999.99721
0.024	999.99721	999.99718	999.99715	999.99712	999.99709
0.025	999.99709	999.99706	999.99703	999.99700	999.99697
0.026	999.99697	999.99694	999.99691	999.99688	999.99685
0.027	999.99685	999.99682	999.99679	999.99676	999.99673
0.028	999.99673	999.99670	999.99667	999.99664	999.99661
0.029	999.99661	999.99658	999.99655	999.99652	999.99649
0.030	999.99649	999.99646	999.99643	999.99640	999.99637
0.031	999.99637	999.99634	999.99631	999.99628	999.99625
0.032	999.99625	999.99622	999.99619	999.99616	999.99613
0.033	999.99613	999.99610	999.99607	999.99604	999.99601
0.034	999.99601	999.99598	999.99595	999.99592	999.99589
0.035	999.99589	999.99586	999.99583	999.99580	999.99577
0.036	999.99577	999.99574	999.99571	999.99568	999.99565
0.037	999.99565	999.99562	999.99559	999.99556	999.99553
0.038	999.99553	999.99550	999.99547	999.99544	999.99541
0.039	999.99541	999.99538	999.99535	999.99532	999.99529
0.040	999.99529	999.99526	999.99523	999.99520	999.99517
0.041	999.99517	999.99514	999.99511	999.99508	999.99505
0.042	999.99505	999.99502	999.99499	999.99496	999.99493
0.043	999.99493	999.99490	999.99487	999.99484	999.99481
0.044	999.99481	999.99478	999.99475	999.99472	999.99469
0.045	999.99469	999.99466	999.99463	999.99460	999.99457
0.046	999.99457	999.99454	999.99451	999.99448	999.99445
0.047	999.99445	999.99442	999.99439	999.99436	999.99433
0.048	999.99433	999.99430	999.99427	999.99424	999.99421
0.049	999.99421	999.99418	999.99415	999.99412	999.99409
0.050	999.99409	999.99406	999.99403	999.99400	999.99397
0.051	999.99397	999.99394	999.99391	999.99388	999.99385
0.052	999.99385	999.99382	999.99379	999.99376	999.99373
0.053	999.99373	999.99370	999.99367	999.99364	999.99361
0.054	999.99361	999.99358	999.99355	999.99352	999.99349
0.055	999.99349	999.99346	999.99343	999.99340	999.99337
0.056	999.99337	999.99334	999.99331	999.99328	999.99325
0.057	999.99325	999.99322	999.99319	999.99316	999.99313
0.058	999.99313	999.99310	999.99307	999.99304	999.99301
0.059	999.99301	999.99298	999.99295	999.99292	999.99289
0.060	999.99289	999.99286	999.99283	999.99280	999.99277
0.061	999.99277	999.99274	999.99271	999.99268	999.99265
0.062	999.99265	999.99262	999.99259	999.99256	999.99253
0.063	999.99253	999.99250	999.99247	999.99244	999.99241
0.064	999.99241	999.99238	999.99235	999.99232	999.99229
0.065	999.99229	999.99226	999.99223	999.99220	999.99217
0.066	999.99217	999.99214	999.99211	999.99208	999.99205
0.067	999.99205	999.99202	999.99199	999.99196	999.99193
0.068	999.99193	999.99190	999.99187	999.99184	999.99181
0.069	999.99181	999.99178	999.99175	999.99172	999.99169
0.070	999.99169	999.99166	999.99163	999.99160	999.99157
0.071	999.99157	999.99154	999.99151	999.99148	999.99145
0.072	999.99145	999.99142	999.99139	999.99136	999.99133
0.073	999.99133	999.99130	999.99127	999.99124	999.99121
0.074	999.99121	999.99118	999.99115	999.99112	999.99109
0.075	999.99109	999.99106	999.99103	999.99100	999.99097
0.076	999.99097	999.99094	999.99091	999.99088	999.99085
0.077	999.99085	999.99082	999.99079	999.99076	999.99073
0.078	999.99073	999.99070	999.99067	999.99064	999.99061
0.079	999.99061	999.99058	999.99055	999.99052	999.99049
0.080	999.99049	999.99046	999.99043	999.99040	999.99037
0.081	999.99037	999.99034	999.99031	999.99028	999.99025
0.082	999.99025	999.99022	999.99019	999.99016	999.99013
0.083	999.99013	999.99010	999.99007	999.99004	999.99001
0.084	999.99001	999.98998	999.98995	999.98992	999.98989
0.085	999.98989	999.98986	999.98983	999.98980	999.98977
0.086	999.98977	999.98974	999.98971	999.98968	999.98965
0.087	999.98965	999.98962	999.98959	999.98956	999.98953
0.088	999.98953	999.98950	999.98947	999.98944	999.98941
0.089	999.98941	999.98938	999.98935	999.98932	999.98929
0.090	999.98929	999.98926	999.98923	999.98920	999.98917
0.091	999.98917	999.98914	999.98911	999.98908	999.98905
0.092	999.98905	999.98902	999.98899	999.98896	999.98893
0.093	999.98893	999.98890	999.98887	999.98884	999.98881
0.094	999.98881	999.98878	999.98875	999.98872	999.98869
0.095	999.98869	999.98866	999.98863	999.98860	999.98857
0.096	999.98857	999.98854	999.98851	999.98848	999.98845
0.097	999.98845	999.98842	999.98839	999.98836	999.98833
0.098	999.98833	999.98830	999.98827	999.98824	999.98821
0.099	999.98821	999.98818	999.98815	999.98812	999.98809
0.100	999.98809	999.98806	999.98803	999.98800	999.98797

TABLE A1 --Range-energy curve for protons on Ta₂O₅

Depth in microns	0.00	0.04	0.08	0.12	0.16
0.000	1000.00000	996.83937	993.67426	990.50311	987.32748
0.200	984.14572	980.95945	977.76863	974.57165	971.37010
0.400	968.16232	964.94994	961.73295	958.50967	955.28174
0.600	952.04747	948.80845	945.56300	942.31287	939.05637
0.800	935.79516	932.52751	929.25514	925.97626	922.69263
1.000	919.40246	916.10572	912.90417	909.49601	906.18300
1.200	902.86333	899.53876	896.20749	892.86951	889.52664
1.400	886.17703	882.82064	879.45744	876.03740	872.71239
1.600	869.33050	865.94169	862.54787	859.14515	855.73738
1.800	852.32260	848.90067	845.47357	842.03754	838.59644
2.000	835.14830	831.69308	828.23074	824.76123	821.28456
2.200	817.80066	814.30952	810.81110	807.30538	803.79232
2.400	800.27189	796.74377	793.20833	789.66553	786.11533
2.600	782.55769	778.99040	775.41779	771.83543	768.24549
2.800	764.64792	761.04044	757.42754	753.80462	750.17394
3.000	746.53526	742.88653	739.23002	735.56571	731.89116
3.200	728.20871	724.51832	720.81754	717.10873	713.39187
3.400	709.65443	705.92635	702.19012	698.42547	694.65999
3.600	690.88379	687.09937	683.30668	679.50309	675.68852
3.800	671.86291	668.02616	664.18362	660.32983	656.46475
4.000	652.58830	648.70021	644.80059	640.88958	636.96712
4.200	633.03594	629.09602	625.14443	621.18109	617.20593
4.400	613.21885	609.21979	605.20867	601.18542	597.14931
4.600	593.10121	589.04097	584.96538	580.87429	576.77078
4.800	572.65472	568.52604	564.38468	560.23055	556.06357
5.000	551.88026	547.67952	543.46641	539.24046	535.00155
5.200	530.74261	526.47045	522.18498	517.88245	513.56276
5.400	509.22942	504.87858	500.51010	496.12646	491.72545
5.600	487.30692	482.87062	478.41639	473.94802	469.45727
5.800	464.95211	460.42408	455.88138	451.31532	446.72891
6.000	442.12381	437.49525	432.85178	428.18426	423.49694
6.200	418.78495	414.05274	409.29526	404.51708	399.71092
6.400	394.88436	390.03249	385.15485	380.25104	375.32588
6.600	370.37382	365.39448	360.38748	355.35245	350.28905
6.800	345.19476	340.06727	334.91163	329.72734	324.50777
7.000	319.25853	313.97281	308.64985	303.29575	297.90131
7.200	292.46803	287.00415	281.49515	275.95421	270.36604
7.400	264.73716	259.06666	253.34585	247.57949	241.76930
7.600	235.90897	229.99705	224.03216	218.01300	211.93828
7.800	205.80582	199.61748	193.35749	187.02050	180.61795
8.000	174.13811	167.58110	160.93481	154.21126	147.41069
8.200	140.52064	133.54113	126.47221	119.31398	112.05337
8.400	104.70375	97.25209	89.69824	82.02875	74.27154
8.600	65.39285	58.41067	50.30733	42.09004	33.74294
8.800	25.26705	16.66247	7.92985	.00000	.00000

TABLE A2 --Range-energy curve for alphas on Ta₂O₅

Depth in microns	0.00	0.04	0.08	0.12	0.16
0.000	5000.00000	4988.66000	4977.30580	4965.93740	4954.55610
0.200	4943.16060	4931.75070	4920.32650	4908.88800	4897.43650
0.400	4885.96940	4874.48900	4862.99310	4851.48390	4839.95900
0.600	4828.42090	4816.86690	4805.29840	4793.71520	4782.11730
0.800	4770.50500	4758.87700	4747.23450	4735.57750	4723.90460
1.000	4712.21700	4700.51470	4688.97660	4677.06230	4665.31460
1.200	4653.55080	4641.77080	4629.97460	4618.16470	4606.33870
1.400	4594.49570	4582.63610	4570.76010	4558.86780	4546.95900
1.600	4535.03520	4523.09620	4511.14070	4499.16850	4487.17970
1.800	4475.17450	4463.15220	4451.11330	4439.05770	4426.98520
2.000	4414.89300	4402.78390	4390.65840	4378.51580	4366.35630
2.200	4354.17970	4341.93590	4329.77210	4317.54110	4305.29290
2.400	4293.02730	4280.74140	4268.43830	4256.11770	4243.77810
2.600	4231.41950	4219.04340	4206.64670	4194.23170	4181.79700
2.800	4169.34340	4156.87070	4144.37800	4131.86790	4119.33760
3.000	4106.78820	4094.21930	4081.63090	4069.02310	4056.39420
3.200	4043.74570	4031.07750	4018.38800	4005.67870	3992.94960
3.400	3980.19900	3967.42850	3954.63650	3941.82440	3928.99070
3.600	3916.13510	3903.25760	3890.35990	3877.44020	3864.49840
3.800	3851.53440	3838.54810	3825.53960	3812.50880	3799.45550
4.000	3786.37910	3773.28020	3760.15690	3747.01330	3733.84500
4.200	3720.65220	3707.43650	3694.19810	3680.93430	3667.64620
4.400	3654.33560	3641.00130	3627.64010	3614.25560	3600.84580
4.600	3587.41070	3573.95220	3560.46650	3546.95720	3533.42060
4.800	3519.86040	3506.27240	3492.65880	3479.01930	3465.35200
5.000	3451.65860	3437.93910	3424.19140	3410.41540	3396.61240
5.200	3382.78260	3368.92470	3355.03870	3341.12430	3327.18140
5.400	3313.21000	3299.20980	3285.18080	3271.12280	3257.03570
5.600	3242.91940	3228.77370	3214.59860	3200.39170	3186.15210
5.800	3171.88280	3157.58350	3143.25200	3128.88320	3114.49400
6.000	3100.06510	3085.60570	3071.11130	3056.58620	3042.02560
6.200	3027.43420	3012.60710	2998.14670	2983.45340	2968.72410
6.400	2953.96100	2939.16160	2924.32810	2909.45790	2894.55030

TABLE A2 Continued

Depth in microns	0.03	0.04	0.08	0.12	0.16
6.600	2879.50510	2864.62310	2849.60410	2834.54800	2819.45450
6.800	2804.32360	2789.15440	2773.94670	2758.70110	2743.41470
7.000	2728.03720	2712.72130	2697.31410	2681.85420	2666.37340
7.200	2650.84160	2635.26840	2619.65370	2603.99440	2588.29640
7.400	2572.55300	2556.76400	2540.92920	2525.05130	2509.13000
7.600	2493.16210	2477.14730	2461.08550	2444.97660	2428.81450
7.800	2412.60480	2396.34740	2380.04240	2363.68320	2347.27580
8.000	2330.81660	2314.30560	2297.74250	2281.12650	2264.45490
8.200	2247.73070	2230.95360	2214.12020	2197.23000	2180.28310
8.400	2163.28220	2146.22350	2129.10340	2111.92510	2094.68820
8.600	2077.38960	2060.02990	2042.60440	2025.11930	2007.56710
8.800	1989.95530	1972.27670	1954.53100	1936.72510	1918.85130
9.000	1900.90910	1882.89610	1864.81510	1846.66520	1828.44620
9.200	1810.14960	1791.78330	1773.34240	1754.82540	1736.23200
9.400	1717.56180	1698.81020	1679.98100	1661.06990	1642.07660
9.600	1623.00070	1603.84170	1584.59930	1565.26840	1545.84880
9.800	1526.33990	1506.74150	1487.04870	1467.27040	1447.39660
10.000	1427.42700	1407.36130	1387.19940	1366.94060	1346.57470
10.200	1326.11160	1305.54100	1284.87410	1264.09840	1243.21420
10.400	1222.22160	1201.12070	1179.91190	1158.58910	1137.15790
10.600	1115.61340	1093.95610	1072.17970	1050.28430	1028.27080
10.800	1006.14029	983.89447	961.53241	939.04511	916.44385
11.000	893.72102	870.88324	847.92724	824.85508	801.67031
11.200	778.37332	754.96515	731.45659	707.84472	684.14058
11.400	660.34794	636.47360	612.52424	588.51250	564.44987
11.600	540.35441	516.23589	492.12109	468.02177	443.97245
11.800	419.99701	396.12010	372.39090	348.84964	325.53982
12.000	302.53191	279.85414	257.56913	235.78061	214.55834
12.200	194.00313	174.11718	155.06183	136.95589	119.92844
12.400	104.08955	89.43985	76.03236	64.01065	53.06524
12.600	43.33601	34.60065	26.92987	20.10485	14.13502
12.800	8.88307	4.32130	.26947	.00000	.00000

TABLE A3 --Kinematics of the $^{18}\text{O}(p,\alpha)^{15}\text{N}$ reaction

PROTON ENERGY (MeV)	ALPHA ENERGY (MeV)	PROTON ENERGY (MeV)	ALPHA ENERGY (MeV)
0.500	3.250	0.760	3.374
0.510	3.254	0.770	3.379
0.520	3.259	0.780	3.384
0.530	3.263	0.790	3.389
0.540	3.268	0.800	3.394
0.550	3.273	0.810	3.399
0.560	3.277	0.820	3.404
0.570	3.282	0.830	3.409
0.580	3.287	0.840	3.414
0.590	3.292	0.850	3.419
0.600	3.296	0.860	3.424
0.610	3.301	0.870	3.430
0.620	3.306	0.880	3.435
0.630	3.310	0.890	3.440
0.640	3.315	0.900	3.445
0.650	3.320	0.910	3.450
0.660	3.325	0.920	3.455
0.670	3.330	0.930	3.460
0.680	3.335	0.940	3.465
0.690	3.340	0.950	3.470
0.700	3.345	0.960	3.476
0.710	3.350	0.970	3.481
0.720	3.354	0.980	3.486
0.730	3.359	0.990	3.491
0.740	3.364	1.000	3.496
0.750	3.369		

TABLE A4 --Range-energy curve for protons on ZnF₂

Depth in microns	0.00	0.04	0.08	0.12	0.16
0.000	1000.00000	977.19401	994.38459	991.57020	988.75079
0.200	985.92792	983.10003	980.26708	977.43066	974.58915
0.400	971.74256	968.89248	966.03728	963.17693	960.31307
0.600	957.44406	954.56985	951.69047	948.80591	945.91781
0.800	943.02452	940.12599	937.22221	934.31488	931.40230
1.000	928.48441	925.56123	922.63275	919.69892	916.75974
1.200	913.81696	910.86879	907.91524	904.95629	901.99192
1.400	899.02199	896.04652	893.06565	890.07934	887.08761
1.600	884.09042	881.08775	878.07961	875.06595	872.04678
1.800	869.02206	865.99178	862.95594	859.91450	856.86745
2.000	853.81479	850.75648	847.69056	844.61901	841.54180
2.200	838.45892	835.37035	832.27608	829.17410	826.06638
2.400	822.95290	819.83365	816.70860	813.57572	810.43700
2.600	807.29244	804.13996	800.98160	797.81704	794.64668
2.800	791.46840	788.28423	785.09205	781.89395	778.68991
3.000	775.47776	772.25964	769.03334	765.80102	762.56047
3.200	759.31385	756.05893	752.79791	749.52832	746.25259
3.400	742.96856	739.67844	736.37996	733.07305	729.75998
3.600	726.43842	723.10831	719.77196	716.42699	713.07337
3.800	709.71344	706.34478	702.96735	699.58322	696.19025
4.000	692.78848	689.37791	685.95848	682.53263	679.09533
4.200	675.65156	672.19875	668.73687	665.26587	661.78571
4.400	658.29634	654.79772	651.28981	647.77233	644.24566
4.600	640.70969	637.16438	633.60965	630.04274	626.46909
4.800	622.88311	619.28754	615.68233	612.06456	608.43994
5.000	604.80265	601.15555	597.49794	593.82775	590.14779
5.200	586.45796	582.75524	579.03953	575.31685	571.58104
5.400	567.83200	564.07279	560.30336	556.52048	552.72406
5.600	548.91384	545.09316	541.26219	537.41764	533.55938
5.800	529.68733	525.80138	521.90144	517.98739	514.06612
6.000	510.13061	506.18076	502.21648	498.23718	494.24312
6.200	490.23481	486.21213	482.17496	478.12318	474.05667
6.400	469.97148	465.86746	461.74830	457.61390	453.46414
6.600	449.29804	445.11632	440.91532	436.69487	432.45883
6.800	428.20710	423.93953	419.64740	415.33915	411.01465
7.000	406.66483	402.29847	397.91494	393.50547	389.07957
7.200	384.62777	380.15918	375.66885	371.15660	366.62214
7.400	362.06531	357.48072	352.87847	348.24689	343.59183
7.600	338.91430	334.20867	329.47985	324.72209	319.94060
7.800	315.12938	310.28801	305.42199	300.52508	295.59462
8.000	290.63407	285.64288	280.62052	275.56645	270.48019
8.200	265.36123	260.20913	255.01646	249.78966	244.51876
8.400	239.21416	233.86799	228.47933	223.05524	217.57936
8.600	212.06696	206.50098	200.89751	195.24211	189.52146
8.800	183.75685	177.92827	172.03648	166.08223	160.06625
9.000	153.98926	147.85197	141.65510	135.38917	129.05505
9.200	122.66362	116.20543	109.68132	103.09202	96.43833
9.400	89.71096	82.92077	76.05852	69.12507	62.12127
9.600	55.04792	47.90586	40.69589	33.40895	26.04591
9.800	18.61753	11.10493	3.52873	.00000	.00000

TABLE A5 --Range-energy curve for alphas on ZnF₂

Depth in microns	0.00	0.04	0.08	0.12	0.16
0.000	5000.00000	4990.16020	4980.30860	4970.44510	4960.57100
0.200	4950.68620	4940.78950	4930.88100	4920.96060	4911.02810
0.400	4901.08380	4891.12740	4881.15910	4871.17860	4861.18620
0.600	4851.18170	4841.16510	4831.13640	4821.09560	4811.04260
0.800	4800.97740	4790.89980	4780.81000	4770.70810	4760.59390
1.000	4750.46630	4740.32520	4730.17190	4720.00610	4709.82820
1.200	4699.63790	4689.43390	4679.21630	4668.98630	4658.74380
1.400	4648.48880	4638.21890	4627.93650	4617.64150	4607.33260
1.600	4597.00980	4586.67430	4576.32500	4565.96170	4555.58600
1.800	4545.19500	4534.79130	4524.37370	4513.94210	4503.49780
2.000	4493.03810	4482.56550	4472.07750	4461.57670	4451.06040
2.200	4440.53110	4429.98630	4419.42860	4408.85510	4398.26710
2.400	4387.66460	4377.04780	4366.41660	4355.76970	4345.10830
2.600	4334.43240	4323.74060	4313.03430	4302.31200	4291.57500
2.800	4280.82210	4270.05450	4259.27080	4248.47250	4237.65790
3.000	4226.82700	4215.98140	4205.11960	4194.24000	4183.34530
3.200	4172.43580	4161.51150	4150.57210	4139.61760	4128.64780
3.400	4117.66260	4106.66180	4095.64510	4084.61250	4073.56400
3.600	4062.49920	4051.41810	4040.32050	4029.20480	4018.07230
3.800	4006.92300	3995.75580	3984.56690	3973.35820	3962.12790
4.000	3950.87790	3939.60820	3928.31720	3917.00480	3905.67310
4.200	3894.32020	3882.94610	3871.55290	3860.13690	3848.70190
4.400	3837.24610	3825.76340	3814.27220	3802.75440	3791.23630
4.600	3779.69560	3768.13540	3756.55280	3744.94650	3733.52170
4.800	3721.67330	3710.00190	3698.31120	3686.59770	3674.86140
5.000	3663.10420	3651.32610	3639.52550	3627.70240	3615.85680
5.200	3603.98880	3592.08900	3580.15760	3568.20880	3556.24240
5.400	3544.25830	3532.25610	3520.23570	3508.19700	3496.13960
5.600	3484.06340	3471.96670	3459.84910	3447.71220	3435.55560
5.800	3423.37920	3411.18280	3398.96630	3386.73450	3374.48010
6.000	3362.20290	3349.90130	3337.57480	3325.22550	3312.85130
6.200	3300.45220	3288.03000	3275.58070	3263.10830	3250.60860
6.400	3238.08570	3225.53520	3212.96140	3200.36010	3187.73280
6.600	3175.08010	3162.39980	3149.69380	3136.96210	3124.20260
6.800	3111.41710	3098.60370	3085.76200	3072.89410	3059.99790
7.000	3047.07330	3034.12010	3021.13830	3008.12780	2995.08840
7.200	2982.02010	2968.92290	2955.79650	2942.63880	2929.45190

TABLE A5 -Continued

Depth in microns	0.00	0.04	0.08	0.12	0.16
7.400	2916.23560	2902.98770	2889.71040	2876.40120	2863.06250
7.600	2849.69180	2836.28890	2822.85380	2809.38630	2795.88850
7.800	2782.35580	2768.79060	2755.19300	2741.56010	2727.89690
8.000	2714.19830	2700.46400	2686.69880	2672.89770	2659.06040
8.200	2645.18690	2631.27710	2617.33080	2603.34770	2589.32840
8.400	2575.27190	2561.17850	2547.04770	2532.87960	2518.67410
8.600	2504.42830	2490.14180	2475.81760	2461.45570	2447.05040
8.800	2432.60700	2418.11990	2403.59460	2389.02540	2374.41730
9.000	2359.76580	2345.07230	2330.33720	2315.55750	2300.73290
9.200	2285.86590	2270.95430	2255.99790	2240.99630	2225.94940
9.400	2210.85700	2195.71860	2180.53110	2165.29610	2150.01610
9.600	2134.68780	2119.31010	2103.88240	2088.40790	2072.87890
9.800	2057.29840	2041.66540	2025.97930	2010.24390	1994.45400
10.000	1978.60960	1962.71010	1946.75510	1930.74460	1914.67820
10.200	1898.55570	1882.37450	1866.13780	1849.84150	1833.48570
10.400	1817.07320	1800.59670	1784.06510	1767.46730	1750.80690
10.600	1734.08390	1717.29450	1700.44220	1683.52310	1666.53310
10.800	1649.48720	1632.36990	1615.18600	1597.93110	1580.60380
11.000	1563.20910	1545.74280	1528.20450	1510.59410	1492.91230
11.200	1475.15360	1457.31660	1439.40110	1421.40710	1403.33480
11.400	1385.18420	1366.95510	1348.64750	1330.25720	1311.78410
11.600	1293.22860	1274.59040	1255.86490	1237.05660	1218.16140
11.800	1199.17920	1180.11060	1160.95450	1141.71150	1122.37730
12.000	1102.95240	1083.44280	1063.83720	1044.14130	1024.35500
12.200	1004.47764	984.50726	964.44520	944.29353	924.05310
12.400	903.71614	883.29293	862.78028	842.18204	821.57028
12.600	800.73308	779.88632	758.96055	737.96099	716.88791
12.800	695.74608	674.54001	653.27863	631.96689	610.61110
13.000	589.22438	567.80986	546.37941	524.94670	503.52357
13.200	482.13010	460.77687	439.49234	418.28785	397.19035
13.400	376.23817	355.44199	334.86611	314.50749	294.43271
13.600	274.66574	255.24753	236.27876	217.73515	199.69492
13.800	182.27444	165.42606	149.27131	133.93268	119.40576
14.000	105.84727	93.21437	81.50187	70.77483	60.91091
14.200	51.94603	43.91575	36.52927	29.99504	24.09231
14.400	18.79689	14.07300	9.88054	6.17252	2.88440

TABLE A6 --Kinematics of the $^{19}\text{F}(\text{p},\alpha)^{16}\text{O}$ reaction

PROTON ENERGY (MeV)	ALPHA ENERGY (MeV)	PROTON ENERGY (MeV)	ALPHA ENERGY (MeV)
0.500	6.516	0.760	6.625
0.510	6.519	0.770	6.630
0.520	6.523	0.780	6.634
0.530	6.527	0.790	6.639
0.540	6.531	0.800	6.643
0.550	6.535	0.810	6.648
0.560	6.539	0.820	6.652
0.570	6.544	0.830	6.657
0.580	6.548	0.840	6.662
0.590	6.552	0.850	6.666
0.600	6.556	0.860	6.671
0.610	6.560	0.870	6.675
0.620	6.564	0.880	6.680
0.630	6.568	0.890	6.685
0.640	6.573	0.900	6.689
0.650	6.577	0.910	6.694
0.660	6.581	0.920	6.699
0.670	6.586	0.930	6.704
0.680	6.590	0.940	6.708
0.690	6.594	0.950	6.713
0.700	6.599	0.960	6.718
0.710	6.603	0.970	6.723
0.720	6.607	0.980	6.727
0.730	6.612	0.990	6.732
0.740	6.616	1.000	6.737
0.750	6.621		

TABLE A7 -Kinematics of the $^{19}\text{F}(\text{p},\alpha_1)^{16}\text{O}^*$ reaction

PROTON ENERGY (MeV)	ALPHA ENERGY (MeV)	PROTON ENERGY (MeV)	ALPHA ENERGY (MeV)
0.500	1.773	0.760	1.917
0.510	1.779	0.770	1.922
0.520	1.784	0.780	1.928
0.530	1.790	0.790	1.934
0.540	1.795	0.800	1.939
0.550	1.801	0.810	1.945
0.560	1.806	0.820	1.951
0.570	1.811	0.830	1.956
0.580	1.817	0.840	1.962
0.590	1.822	0.850	1.968
0.600	1.828	0.860	1.973
0.610	1.833	0.870	1.979
0.620	1.839	0.880	1.985
0.630	1.844	0.890	1.990
0.640	1.850	0.900	1.996
0.650	1.856	0.910	2.002
0.660	1.861	0.920	2.007
0.670	1.867	0.930	2.013
0.680	1.872	0.940	2.019
0.690	1.878	0.950	2.024
0.700	1.883	0.960	2.030
0.710	1.889	0.970	2.036
0.720	1.894	0.980	2.041
0.730	1.900	0.990	2.047
0.740	1.906	1.000	2.053
0.750	1.911		

TABLE A8 -Range-energy curve for protons on SiO₂

Depth in microns	0.00	0.04	0.08	0.12	0.16
0.000	1000.00000	998.27081	996.53918	994.80727	993.07290
0.200	991.33608	989.59787	987.85828	986.11622	984.37169
0.400	982.62577	980.87846	979.12865	977.37634	975.62263
0.600	973.86753	972.10991	970.34975	968.58820	966.82523
0.800	965.05973	963.29168	961.52107	959.75019	957.97675
1.000	956.20074	954.42215	952.64214	950.86071	949.07640
1.200	947.28957	945.50016	943.71050	941.91824	940.12338
1.400	938.32592	936.52585	934.72554	932.92261	931.11705
1.600	929.30255	927.49801	925.68693	923.87321	922.05682
1.800	920.23778	918.41606	916.59290	914.76828	912.94098
2.000	911.11097	909.27827	907.44286	905.60599	903.76767
2.200	901.92662	900.08291	898.23649	896.38734	894.53544
2.400	892.68336	890.82953	888.97094	887.11060	885.24748
2.600	883.38160	881.51293	879.64408	877.77244	875.89801
2.800	874.02079	872.14074	870.25788	868.37219	866.48368
3.000	864.59502	862.70352	860.80917	858.91198	857.01192
3.200	855.10901	853.20324	851.29458	849.38266	847.46802
3.400	845.55129	843.63428	841.71379	839.79043	837.86420
3.600	835.93506	834.00305	832.06813	830.13030	828.18955
3.800	826.24588	824.29928	822.34974	820.39726	818.44182
4.000	816.48342	814.52351	812.56209	810.59770	808.63033
4.200	806.65998	804.68664	802.71029	800.73095	798.74854
4.400	796.76315	794.77470	792.78340	790.78902	788.79162
4.600	786.79120	784.78775	782.78127	780.77172	778.75914
4.800	776.74350	774.72478	772.70300	770.67814	768.65018
5.000	766.61913	764.58498	762.54772	760.50735	758.46066
5.200	756.41083	754.35786	752.30175	750.24212	748.17936
5.400	746.11349	744.04451	741.97239	739.89716	737.81879
5.600	735.73726	733.65257	731.56473	729.47203	727.37449
5.800	725.27374	723.16979	721.06262	718.95223	716.83861
6.000	714.72176	712.60166	710.47831	708.34821	706.21485
6.200	704.07819	701.93826	699.79487	697.64816	695.49819
6.400	693.34140	691.18132	689.01794	686.85126	684.68127
6.600	682.50795	680.32765	678.14399	675.95699	673.76661
6.800	671.57287	669.37388	667.16962	664.96195	662.75088
7.000	660.53640	658.31465	656.08947	653.86084	651.62876
7.200	649.39112	647.14794	644.90134	642.65130	640.39584
7.400	638.13494	635.87058	633.60274	631.32939	629.05053
7.600	626.76816	624.48227	622.18875	619.89170	617.59110

TABLE A8-Continued

Depth in microns	0.00	0.04	0.08	0.12	0.16
7.800	615.28486	612.97296	610.65749	608.33631	606.00943
8.000	603.67895	601.34270	599.00038	596.65459	594.30306
8.200	591.94576	589.58487	587.21597	584.84345	582.46730
8.400	580.08303	577.69512	575.30129	572.90152	570.49809
8.600	568.08636	565.67094	563.24950	560.82201	558.38845
8.800	555.94881	553.50544	551.05355	548.59722	546.13269
9.000	543.66450	541.19027	538.70997	536.22355	533.73100
9.200	531.23229	528.72739	526.21627	523.69890	521.17524
9.400	518.64530	516.10902	513.56640	511.01479	508.45939
9.600	505.89491	503.32397	500.74655	498.16175	495.57066
9.800	492.97056	490.36670	487.75373	485.13427	482.50829
10.000	479.87302	477.23115	474.58268	471.92473	469.26009
10.200	466.58874	463.90775	461.21997	458.52540	455.82103
10.400	453.10978	450.39165	447.66297	444.92454	442.17928
10.600	439.42720	436.66516	433.89309	431.11406	428.32803
10.800	425.53179	422.72528	419.91165	417.08761	414.25309
11.000	411.41139	408.55908	405.69613	402.82245	399.94047
11.200	397.04774	394.14447	391.23056	388.30942	385.37750
11.400	382.43471	379.48098	376.51623	373.54038	370.55334
11.600	367.55506	364.54546	361.52446	358.49199	355.44799
11.800	352.39238	349.32429	346.24425	343.14895	340.04217
12.000	336.92383	333.79386	330.65214	327.49447	324.32488
12.200	321.13899	317.94100	314.73082	311.50398	308.26478
12.400	305.00861	301.73994	298.45097	295.14657	291.82998
12.600	288.49651	285.14592	281.78278	278.40223	275.00404
12.800	271.59299	268.16402	264.71692	261.25155	257.76771
13.000	254.26527	250.74404	247.20229	243.64193	240.05730
13.200	236.45927	232.83648	229.19440	225.53282	221.84572
13.400	218.13884	214.41200	210.65893	206.87935	203.07941
13.600	199.26359	195.41913	191.54222	187.63327	183.69263
13.800	179.72068	175.71778	171.68428	167.62053	163.52689
14.000	159.40367	155.25123	151.06991	146.85253	142.59956
14.200	138.31881	134.01061	129.66055	125.28381	120.87338
14.400	116.42967	111.96028	107.45113	102.91702	98.34397
14.600	93.73956	89.10415	84.43109	79.72782	74.99470
14.800	70.22516	65.42652	60.59228	55.72287	50.82549
15.000	45.89374	40.92802	35.92875	30.89635	25.83122
15.200	20.73374	15.59781	10.43040	5.32187	.00000

TABLE A9 -Range-energy curve for alphas on SiO₂

Depth in microns	0.00	0.04	0.08	0.12	0.16
0.000	5000.00000	4994.04800	4988.09110	4982.12960	4976.16340
0.200	4970.19240	4964.21660	4958.23610	4952.25080	4946.26080
0.400	4940.26590	4934.26640	4928.26190	4922.25250	4916.23890
0.600	4910.22010	4904.19650	4898.16810	4892.13490	4886.09690
0.800	4880.05400	4874.00630	4867.95380	4861.89640	4855.83420
1.000	4849.76700	4843.69520	4837.61830	4831.53670	4825.44930
1.200	4819.35610	4813.25810	4807.15520	4801.04740	4794.93420
1.400	4788.81620	4782.69330	4776.56550	4770.43200	4764.29280
1.600	4758.14860	4751.99950	4745.84560	4739.68670	4733.52290
1.800	4727.35250	4721.17710	4714.99680	4708.81160	4702.62140
2.000	4696.42530	4690.22350	4684.01670	4677.80490	4671.58810
2.200	4665.36540	4659.13690	4652.90340	4646.66490	4640.42050
2.400	4634.17010	4627.91470	4621.65440	4615.38810	4609.11590
2.600	4602.83860	4596.55620	4590.26710	4583.97300	4577.67370
2.800	4571.36850	4565.05750	4558.74120	4552.41990	4546.09180
3.000	4539.75850	4533.42020	4517.07490	4520.72450	4514.36800
3.200	4508.00550	4501.63800	4495.26430	4488.88460	4482.49970
3.400	4476.10800	4469.71100	4463.30790	4456.89870	4450.48440
3.600	4444.06300	4437.63640	4431.20380	4424.76490	4418.31990
3.800	4411.86880	4405.41240	4398.94850	4392.47930	4386.00310
4.000	4379.52170	4373.03310	4366.53940	4360.03860	4353.53260
4.200	4347.01940	4340.50100	4333.97540	4327.44460	4320.90550
4.400	4314.36230	4307.81190	4301.25510	4294.69210	4288.12300
4.600	4281.54740	4274.96460	4268.37650	4261.78110	4255.17940
4.800	4248.57140	4241.95600	4235.33430	4228.70620	4222.07180
5.000	4215.43110	4208.78310	4202.12860	4195.46750	4188.79900
5.200	4182.12420	4175.44310	4168.75440	4162.05940	4155.35810
5.400	4148.64920	4141.93290	4135.21010	4128.48100	4121.74430
5.600	4115.00110	4108.25040	4101.49320	4094.72850	4087.95720
5.800	4081.17850	4074.39310	4067.60010	4060.79960	4053.99260
6.000	4047.17790	4040.35670	4033.52770	4026.69110	4019.94680
6.200	4012.99600	4006.13740	3999.27080	3992.39750	3985.51660
6.400	3978.62800	3971.73170	3964.82880	3957.91830	3950.99990
6.600	3944.07380	3937.14000	3930.19840	3923.24900	3916.29300
6.800	3909.32910	3902.35740	3895.37790	3888.39050	3881.39520
7.000	3874.39210	3867.38110	3860.36220	3853.33550	3846.30080
7.200	3839.25810	3832.20540	3825.14660	3818.07890	3811.00320
7.400	3803.91960	3796.82760	3789.72760	3782.61840	3775.50130
7.600	3768.37610	3761.24290	3754.10050	3746.95010	3739.79170

TABLE A9 Continued

Depth in microns	0.00	0.04	0.08	0.12	0.16
7.800	3732.62510	3725.44930	3718.26530	3711.07210	3703.87070
8.000	3696.66120	3689.44240	3682.21540	3674.97890	3667.73430
8.200	3660.48020	3653.21790	3645.94620	3638.66610	3631.37660
8.400	3624.07770	3616.77040	3609.45350	3602.12710	3594.79190
8.600	3587.44730	3580.09310	3572.73060	3565.35650	3557.97680
8.800	3550.58680	3543.18710	3535.77780	3528.35380	3520.93020
9.000	3513.49310	3506.04500	3498.58840	3491.12080	3483.64460
9.200	3476.15880	3468.66300	3461.15750	3453.64210	3446.11550
9.400	3438.58030	3431.03390	3423.47830	3415.91260	3408.33780
9.600	3400.75150	3393.15490	3385.54830	3377.93050	3370.30410
9.800	3362.66640	3355.01750	3347.35980	3339.69090	3332.01050
10.000	3324.32140	3316.62080	3308.90880	3301.18660	3293.45430
10.200	3285.71050	3277.95510	3270.19080	3262.41490	3254.62740
10.400	3246.82820	3239.01710	3231.19730	3223.36570	3215.52230
10.600	3207.66720	3199.80010	3191.92060	3184.03070	3176.13030
10.800	3168.21800	3160.29380	3152.35760	3144.40960	3136.44950
11.000	3128.47730	3120.49310	3112.49690	3104.48860	3096.46810
11.200	3088.43550	3080.39070	3072.33380	3064.26470	3056.18320
11.400	3048.08960	3039.98370	3031.96240	3023.72870	3015.58270
11.600	3007.42440	2999.25360	2991.07100	2982.87440	2974.66370
11.800	2966.44050	2958.20470	2949.95660	2941.69250	2933.41600
12.000	2925.12690	2916.82340	2908.50560	2900.17520	2891.82950
12.200	2883.46950	2875.09680	2866.70920	2858.30830	2849.89210
12.400	2841.46200	2833.01880	2824.55940	2816.08720	2807.59880
12.600	2799.09740	2790.58060	2782.05090	2773.50460	2764.94530
12.800	2756.36950	2747.77880	2739.17330	2730.55290	2721.91760
13.000	2713.26560	2704.59850	2695.91580	2687.21600	2678.50140
13.200	2669.77010	2661.02400	2652.26110	2643.48320	2634.68860
13.400	2625.87890	2617.05230	2608.20870	2599.34810	2590.47270
13.600	2581.58020	2572.67040	2563.74330	2554.80070	2545.84080
13.800	2536.86350	2527.86870	2518.85640	2509.82640	2500.77890
14.000	2491.71120	2482.62590	2473.52290	2464.40220	2455.26370
14.200	2446.10550	2436.92930	2427.73520	2418.52110	2409.28910
14.400	2400.03700	2390.76720	2381.47710	2372.16890	2362.84030
14.600	2353.49130	2344.12410	2334.73630	2325.32800	2315.89910
14.800	2306.44960	2296.98120	2287.48980	2277.97990	2268.44690
15.000	2258.89530	2249.32070	2239.72510	2230.10860	2220.46880
15.200	2210.81020	2201.12820	2191.42320	2181.69700	2171.94930
15.400	2162.17800	2152.38300	2142.56660	2132.72870	2122.86700

TABLE A9 Continued

Depth in microns	0.00	0.04	0.08	0.12	0.16
15.600	2112.98120	2103.07170	2093.13750	2083.17950	2073.19750
15.800	2053.19140	2053.16100	2043.10660	2033.02790	2022.92490
16.000	2012.79770	2002.64610	1992.47010	1982.26500	1972.03560
16.200	1961.78180	1951.50370	1941.19590	1930.86360	1920.50670
16.400	1910.11990	1899.70830	1889.26830	1878.80110	1868.30650
16.600	1857.78450	1847.23500	1836.65770	1826.05280	1815.42010
16.800	1804.75670	1794.06560	1783.34650	1772.59620	1761.81470
17.000	1751.00450	1740.16290	1729.29260	1718.39070	1707.45720
17.200	1696.49180	1685.49460	1674.46550	1663.40440	1652.31130
17.400	1641.18320	1630.02280	1618.83030	1607.60540	1596.34540
17.600	1585.04980	1573.72150	1562.35750	1550.95760	1539.52490
17.800	1528.05330	1516.54880	1505.00530	1493.42900	1481.81380
18.000	1470.16240	1458.47480	1446.74790	1434.98170	1423.18230
18.200	1411.34360	1399.46530	1387.54700	1375.58900	1363.59130
18.400	1351.55380	1339.47660	1327.35950	1315.20270	1303.00620
18.600	1290.76430	1278.48210	1266.15970	1253.79380	1241.38440
18.800	1228.93500	1216.43890	1203.90290	1191.32030	1178.69470
19.000	1166.02610	1153.31110	1140.55320	1127.74920	1114.90230
19.200	1102.00950	1089.07030	1076.08430	1063.05190	1049.97320
19.400	1036.84860	1023.67486	1010.45576	997.19271	983.88069
19.600	970.51964	957.11373	943.65977	930.15846	916.60731
19.800	903.01381	889.37240	875.68635	861.95632	848.17966
20.000	834.35620	820.48672	806.57870	792.62781	778.63380
20.200	764.59683	750.51859	736.39471	722.23292	708.03501
20.400	693.80334	679.53811	665.23596	650.90422	636.54602
20.600	622.15676	607.74401	593.31063	578.85846	564.39113
20.800	549.91232	535.42714	520.93674	506.44745	491.96713
21.000	477.49537	463.03894	448.60418	434.20319	419.83668
21.200	405.51304	391.25183	377.04965	362.91724	348.86909
21.400	334.92293	321.07700	307.35273	293.76725	280.32244
21.600	267.03443	253.91885	241.03571	228.33303	215.84614
21.800	203.61188	191.69625	180.01386	168.58645	157.48347
22.000	146.74482	136.37370	126.42682	116.82968	107.71728
22.200	98.99906	90.77354	82.98512	75.56208	68.60395
22.400	62.09665	55.95399	50.21239	44.84259	39.80813
22.600	35.14212	30.80437	26.82948	23.09533	19.62218
22.800	16.43807	13.48717	10.79208	8.29136	6.00663
23.000	3.87063	1.89747	.04683	.00000	.00000

APPENDIX B

PROCEDURE USED TO FIT MECHANISTIC OXIDATION SAMPLES

APPENDIX B

PROCEDURE USED TO FIT MECHANISTIC OXIDATION SAMPLES

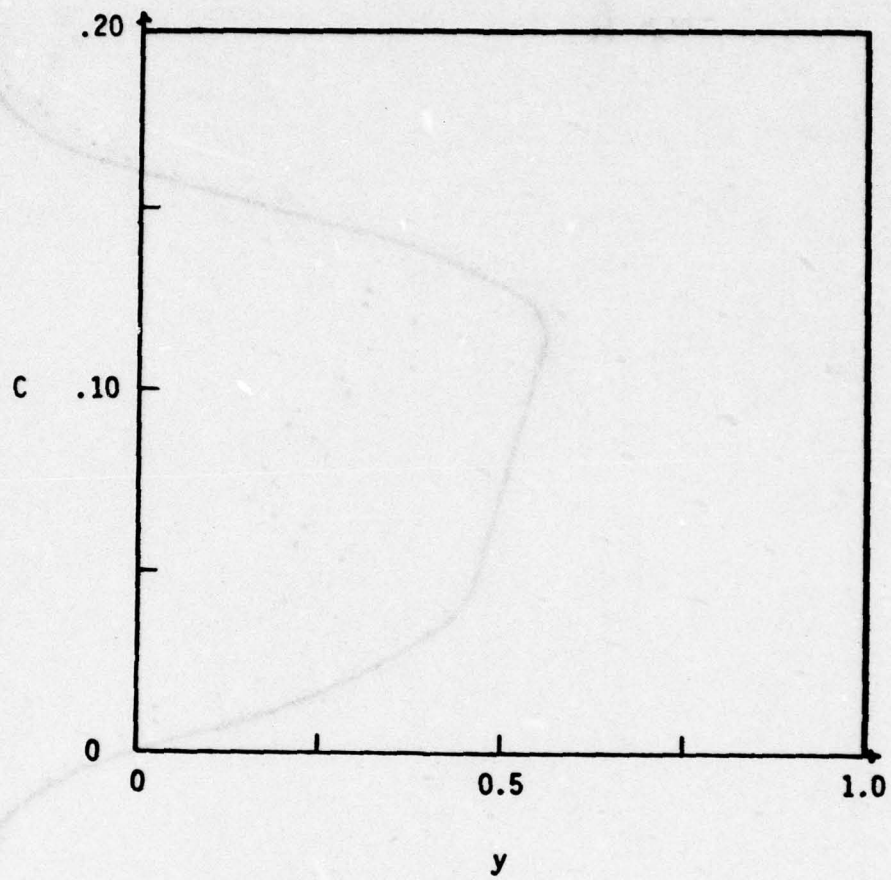


Figure B1 Assumed concentration profile
1 for sample S-5-3.

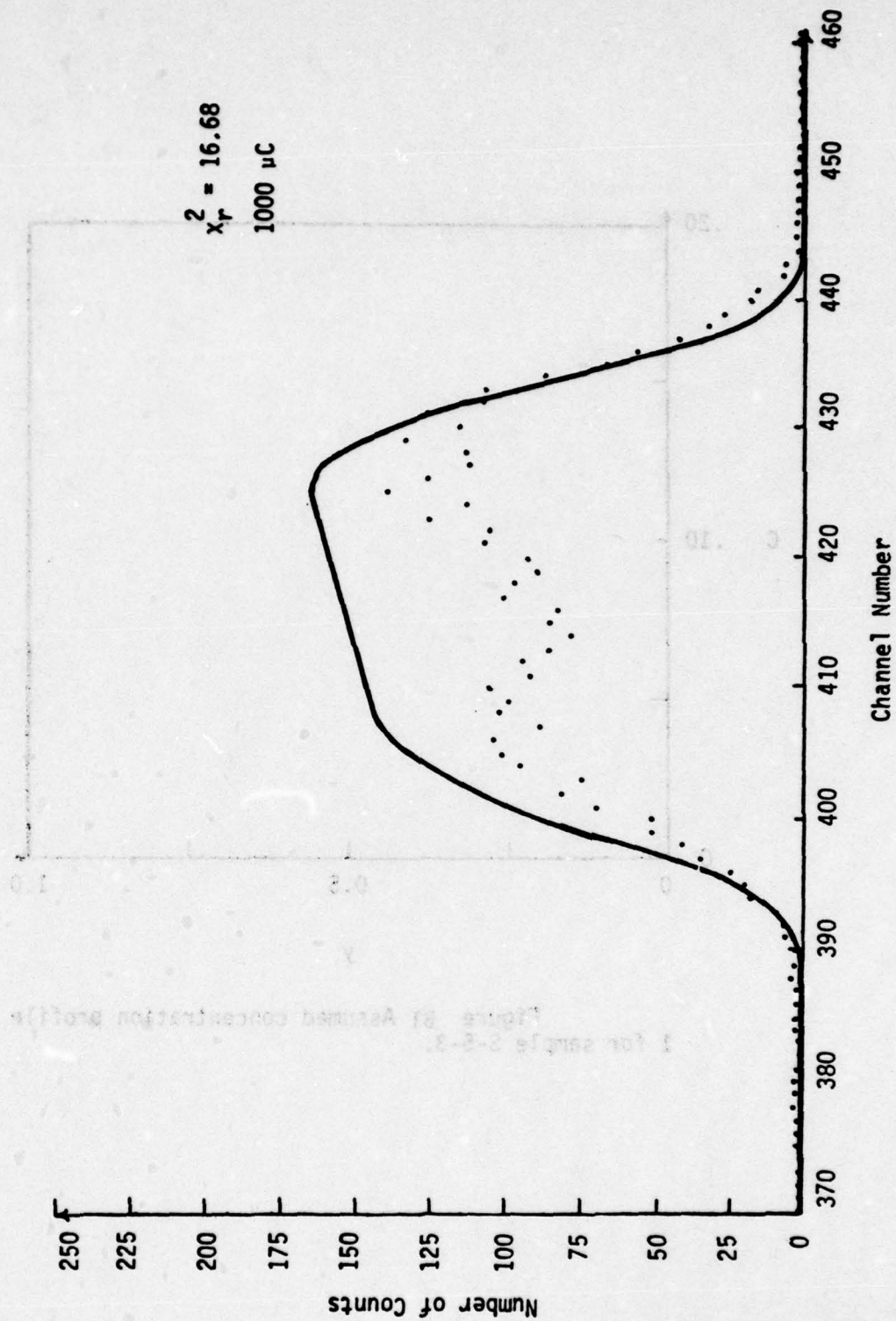


Figure B2 : Comparison of experimental data with predicted spectra using assumed concentration profile 1 for sample S-5-3 at 750 KeV.

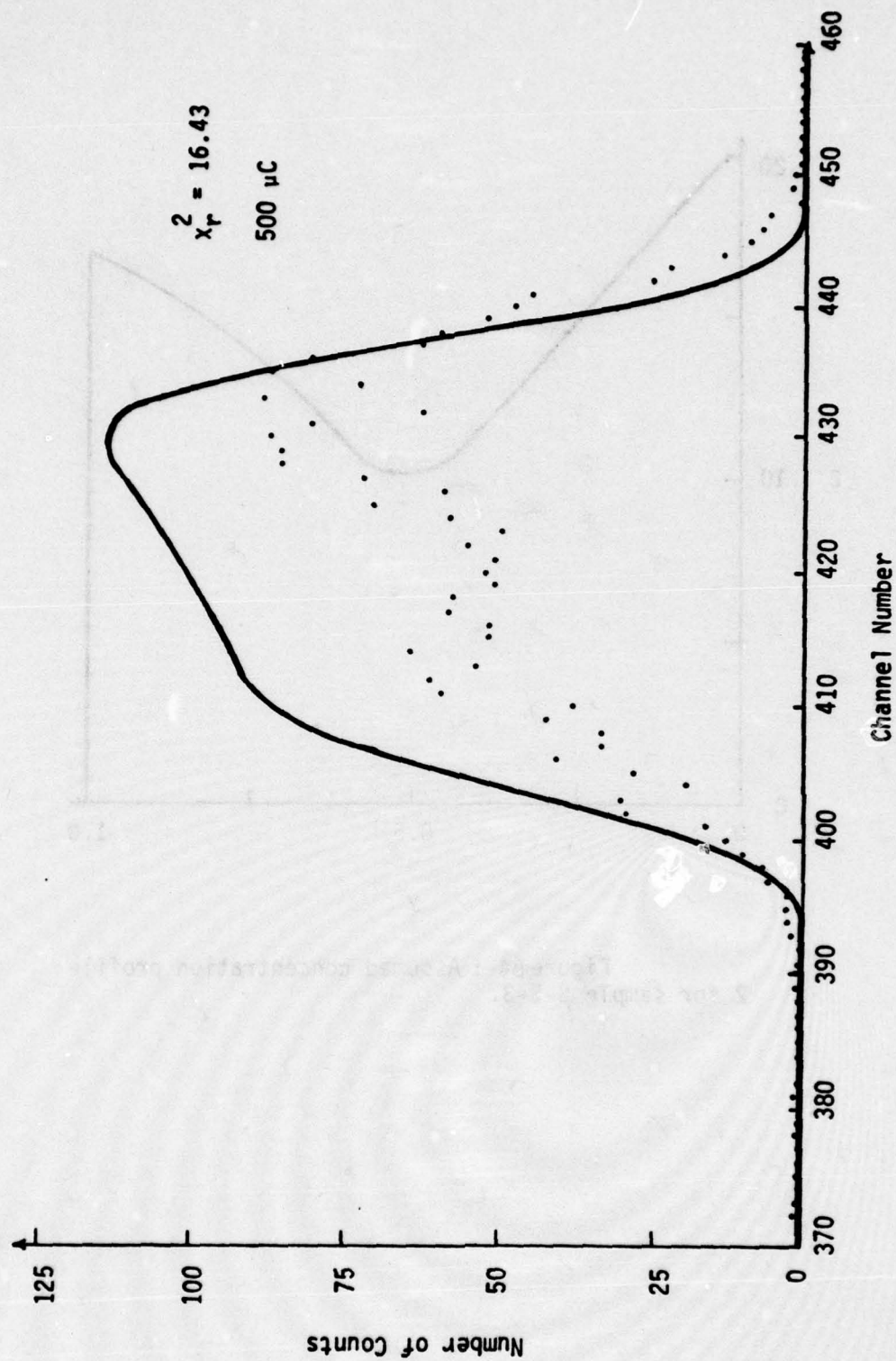


Figure B3 : Comparison of experimental data with predicted spectra using assumed concentration profile 1 for sample S-5-3 at 800 KeV.

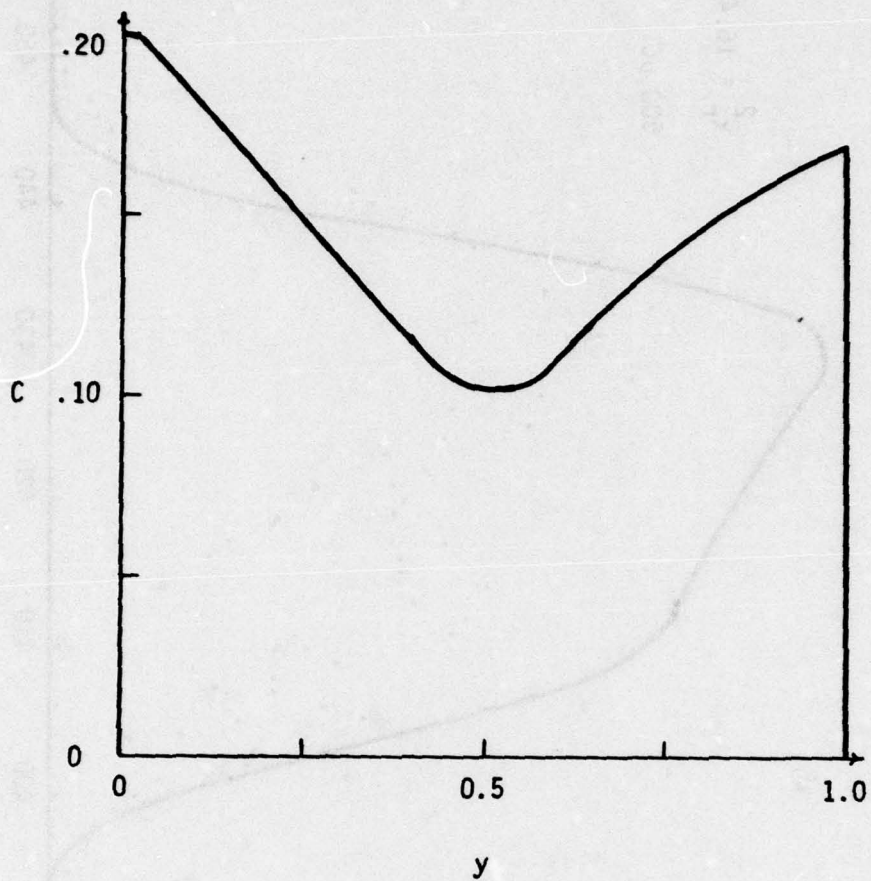


Figure B4 : Assumed concentration profile
2 for sample S-5-3.

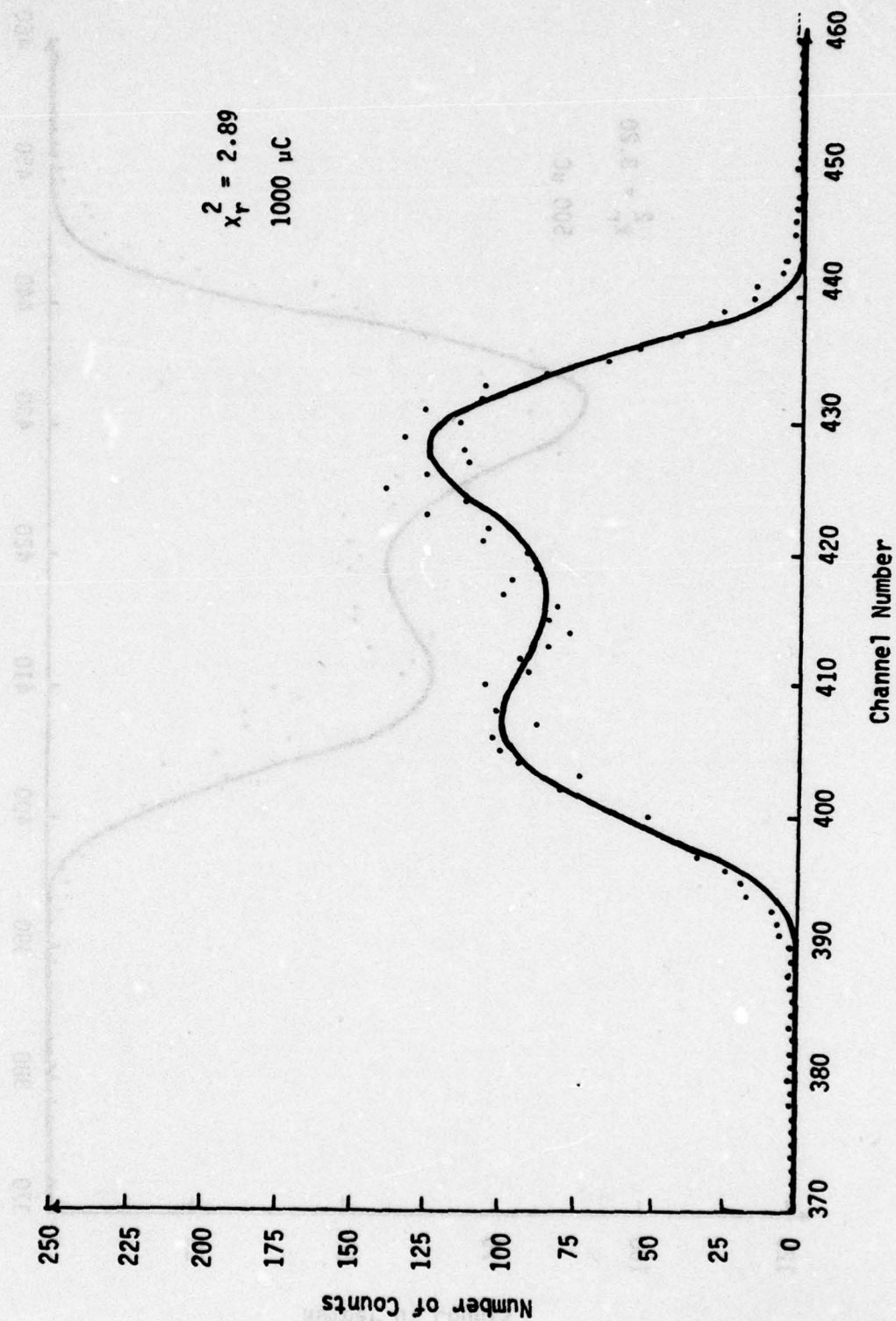


Figure B5 :Comparison of experimental data with predicted spectra using assumed concentration profile 2 for sample S-5-3 at 750 KeV.

CONCENTRATION PROFILE 2 FOR SAMPLE S-5-3 AT 800 KEV.
LINES OF CONCENTRATION OF SUBSTANCES WITH BURIED EFFECTS ARE INDICATED

Channel Number

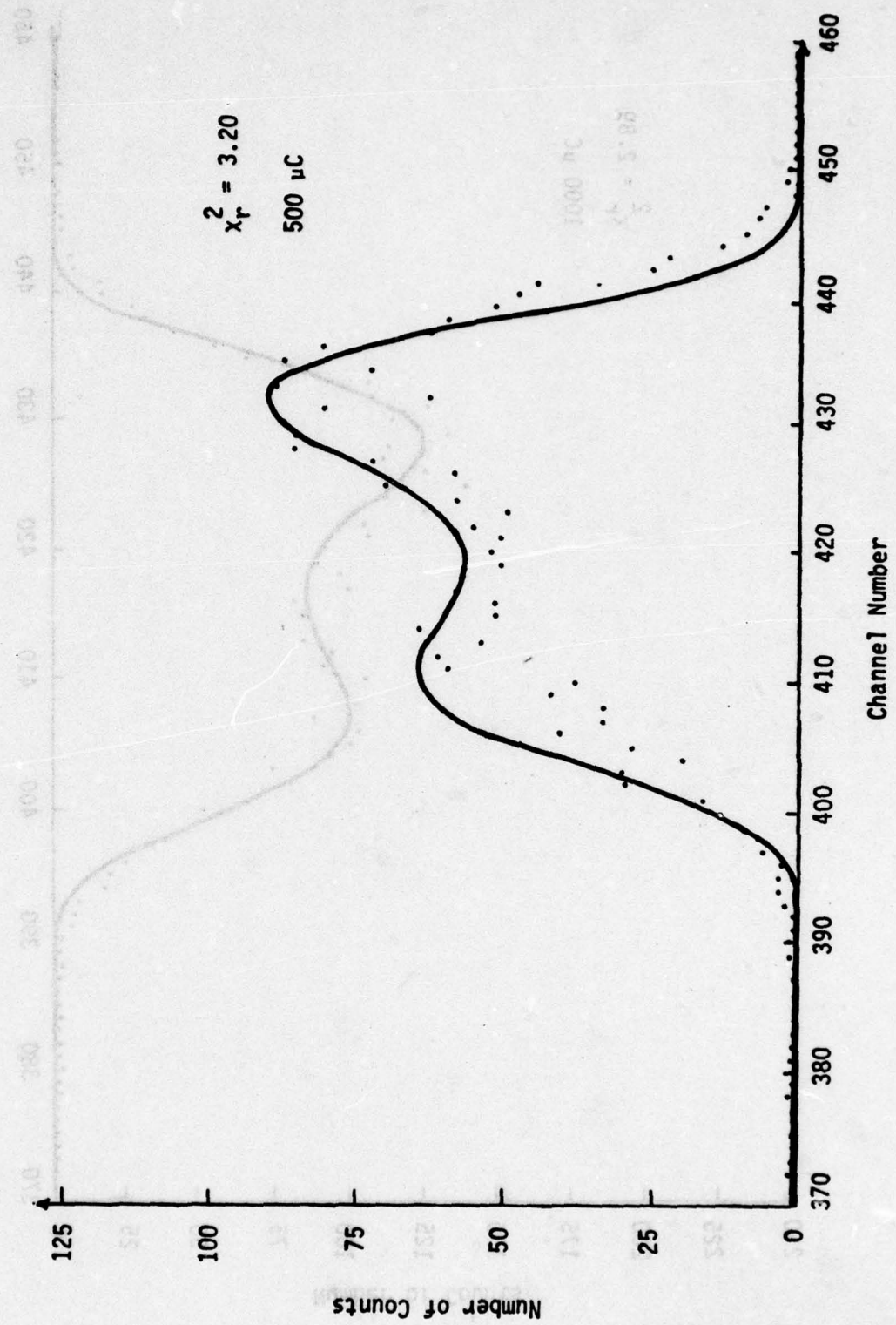


Figure B6 Comparison of experimental data with predicted spectra using assumed concentration profile 2 for sample S-5-3 at 800 KeV.

concentration profile 3 for sample 2-2-3 at 120 rev.
 2,300 200 counts per sec. 1000 MC

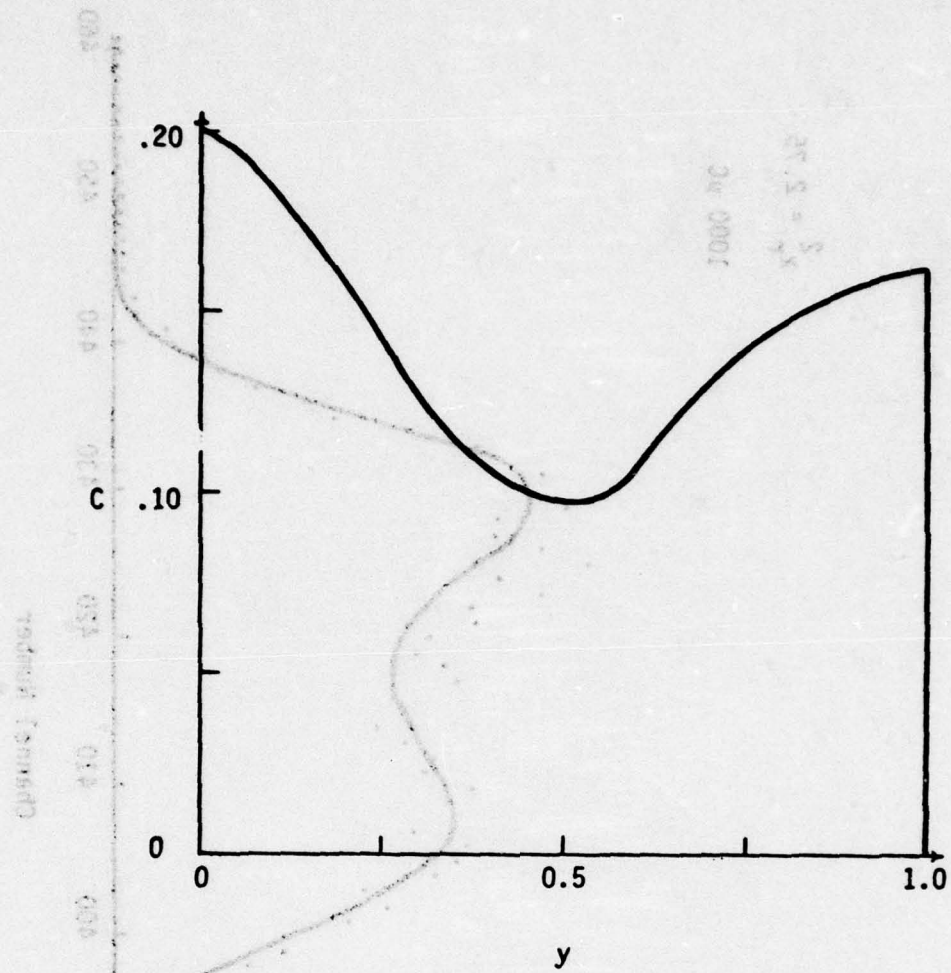
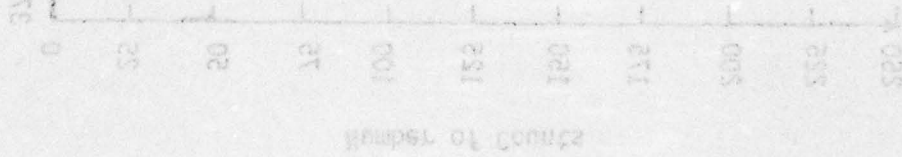


Figure B7 Assumed concentration profile
 3 for sample S-5-3.



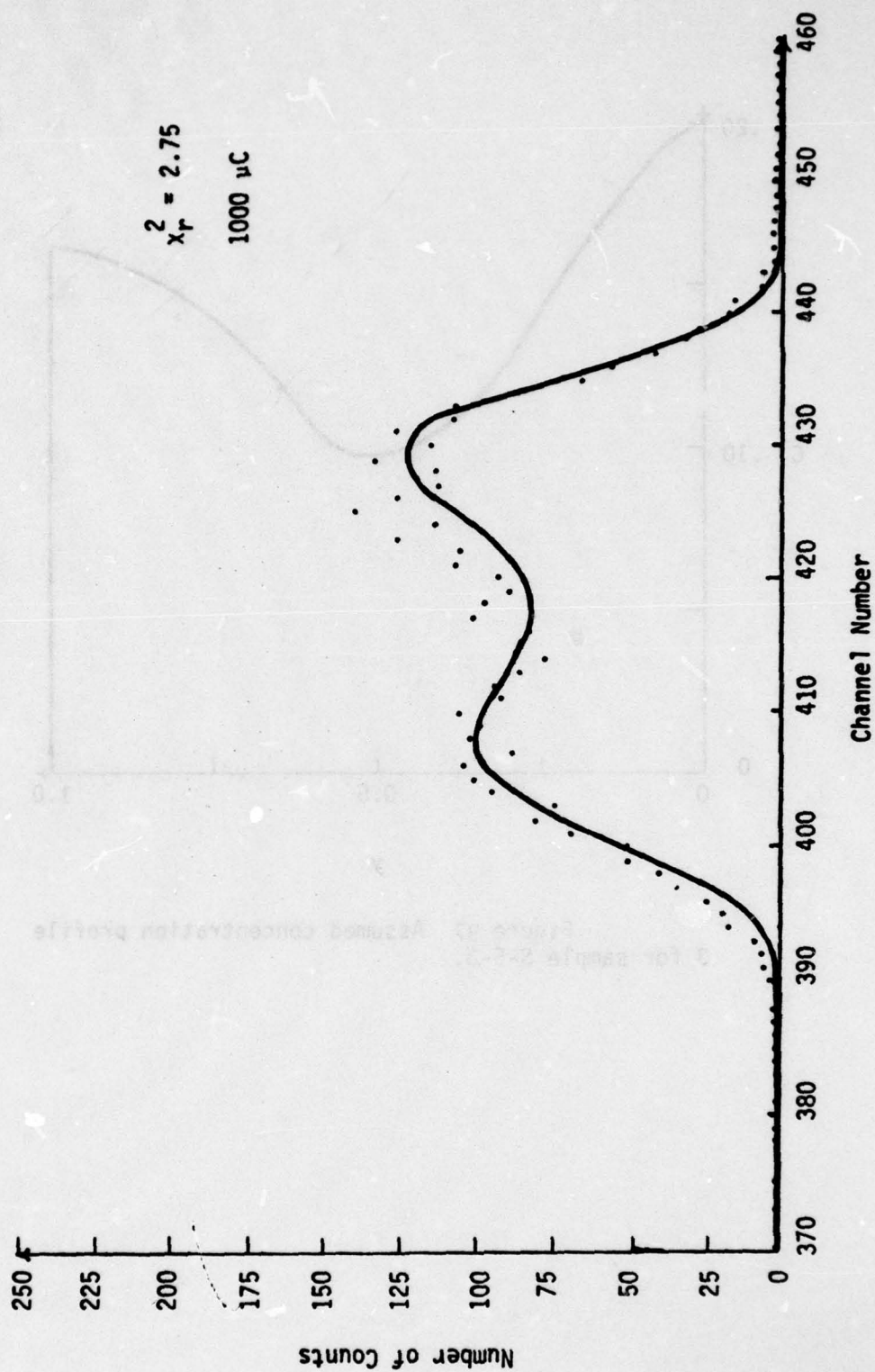


Figure 88 :Comparison of experimental data with predicted spectra using assumed concentration profile 3 for sample S-5-3 at 750 KeV.

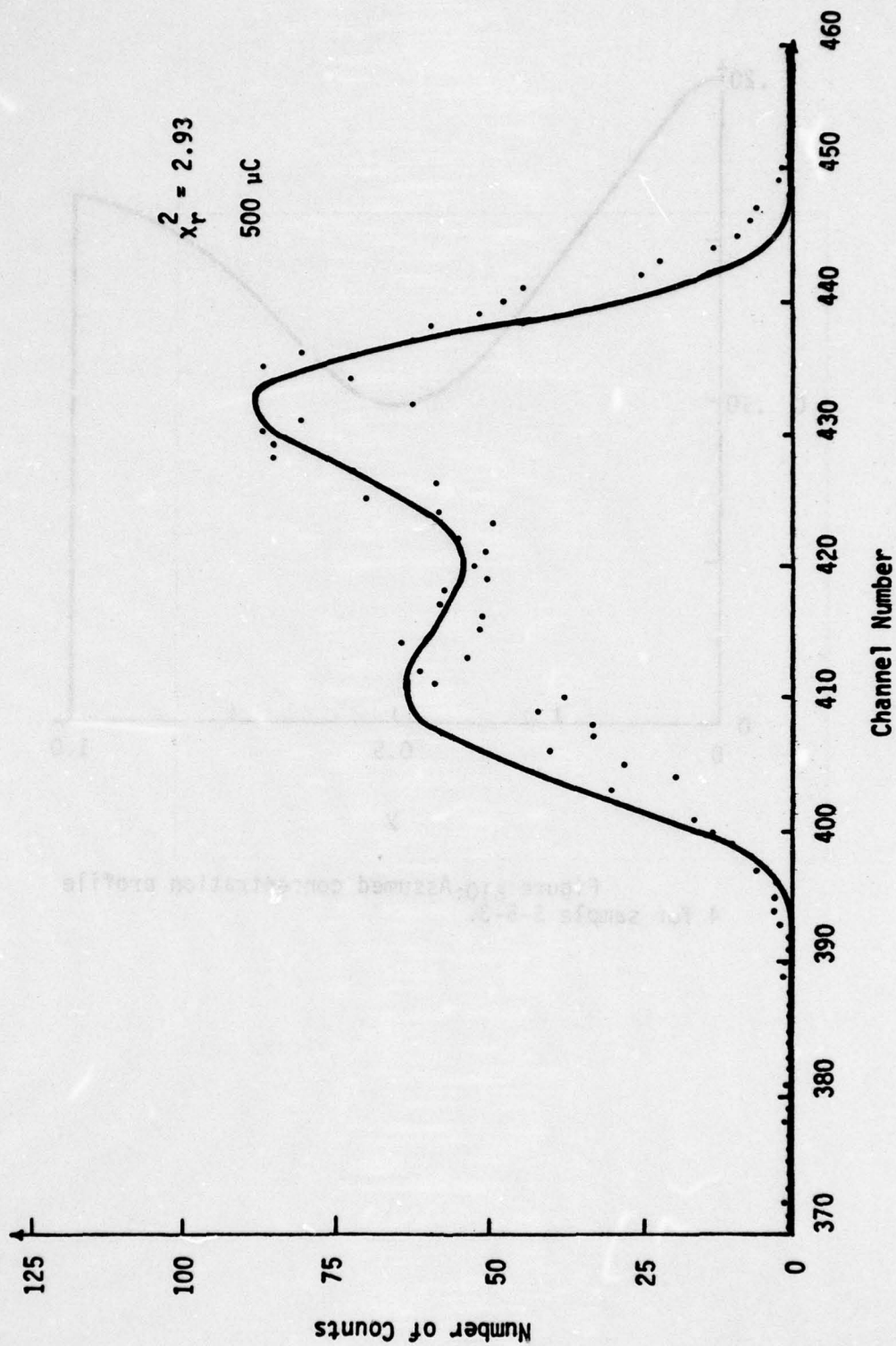


Figure B9 :Comparison of experimental data with predicted spectra using assumed concentration profile 3 for sample S-5-3 at 800 KeV.

CONCENTRATION PROFILE 3 FOR SAMPLE 2-2-3 AT 800 KPa
 1.0E+03 COUNTS/SEC OF 4000-10000, 0.010 WITH BACKGROUND SUBTRACTED

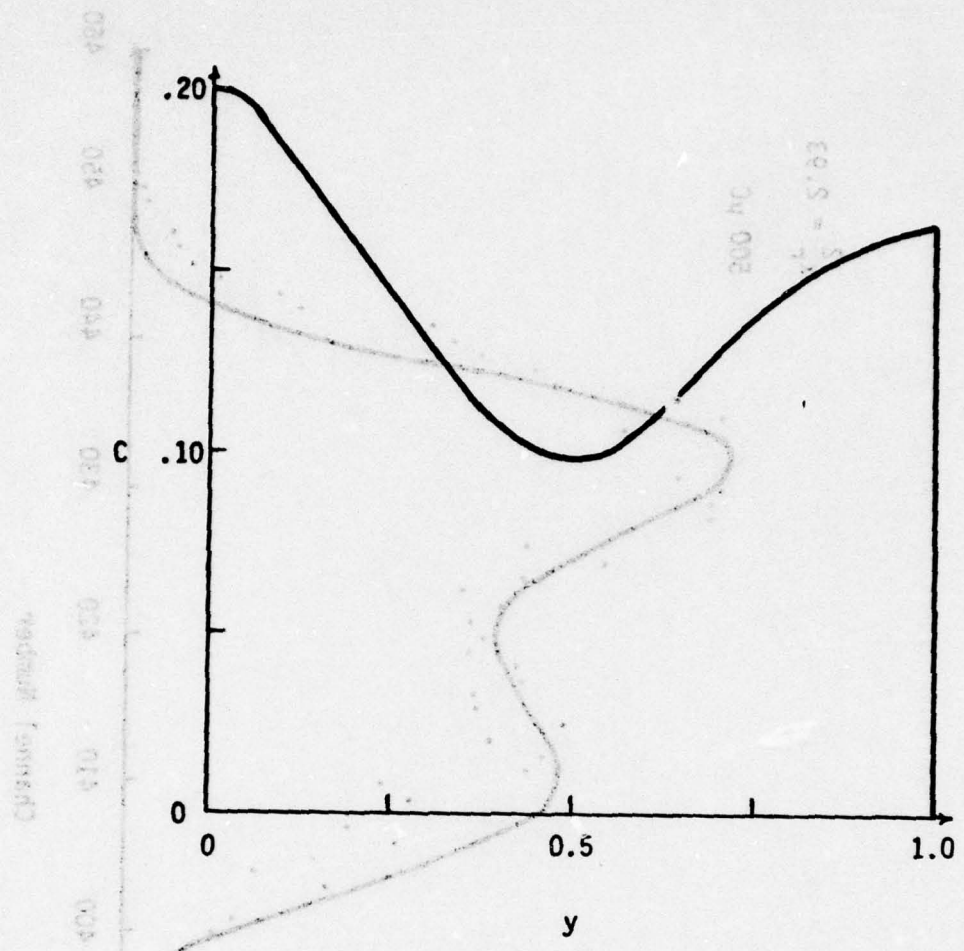
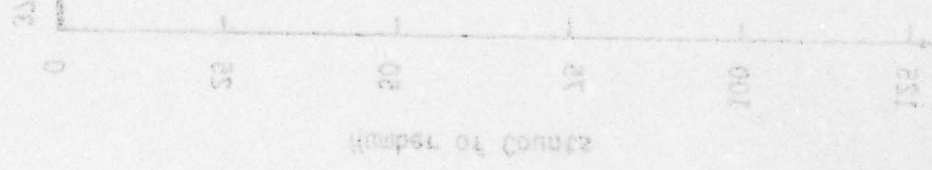


Figure B10: Assumed concentration profile 4 for sample S-5-3.



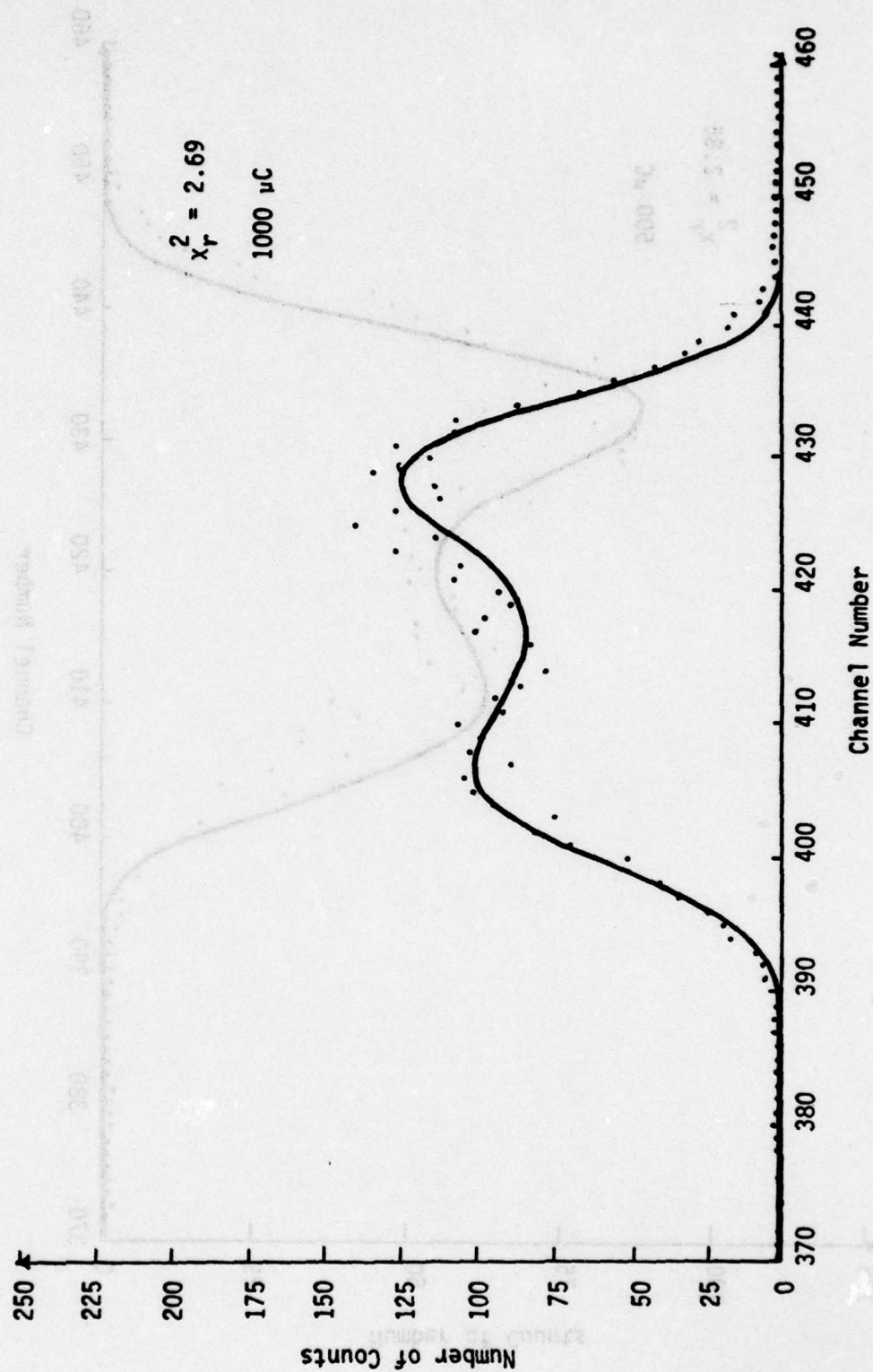


Figure B11: Comparison of experimental data with predicted spectra using assumed concentration profile 4 for sample S-5-3 at 750 KeV.

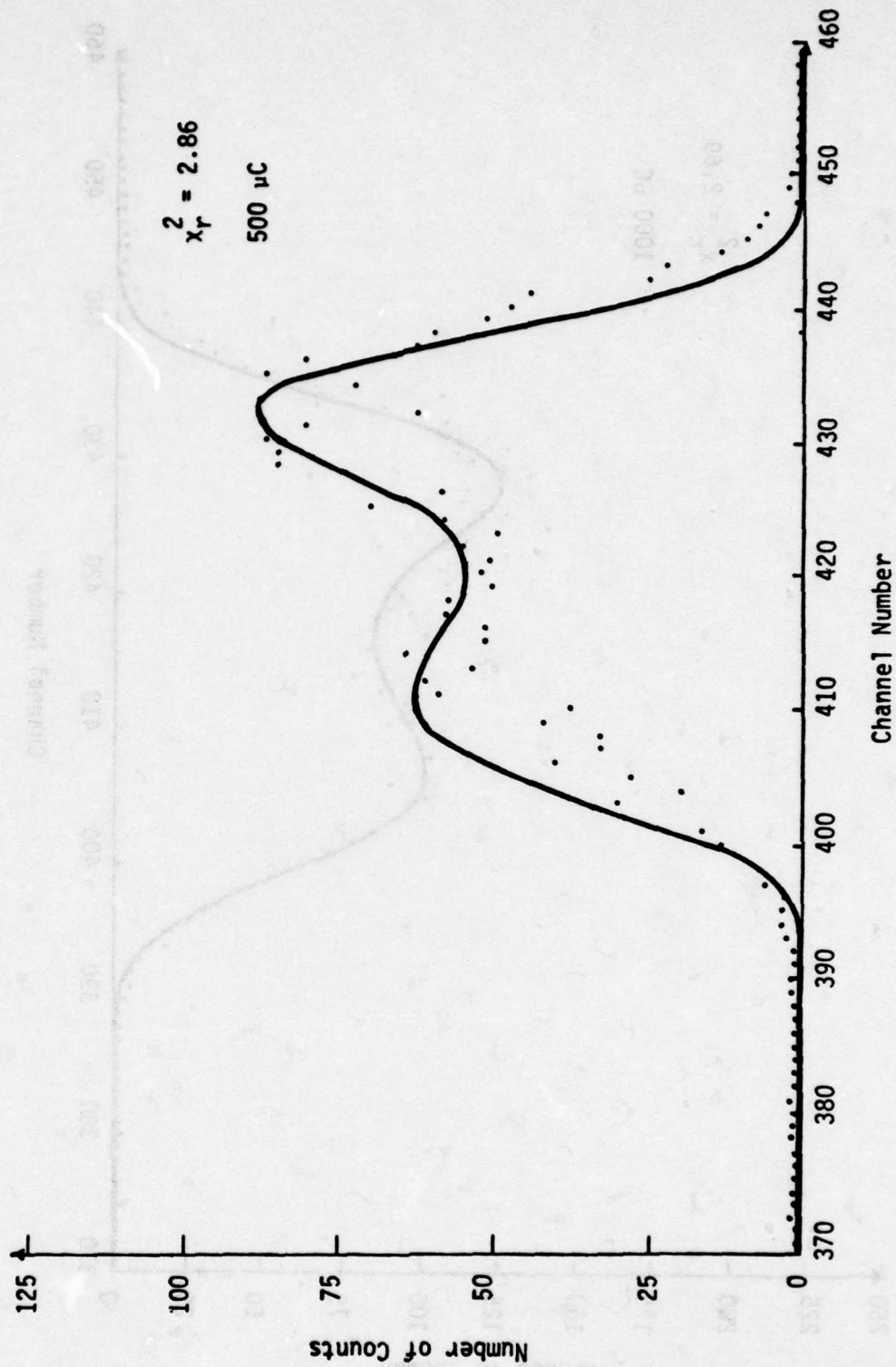


Figure B12: Comparison of experimental data with predicted spectra using assumed concentration profile 4 for sample S-5-3 at 800 KeV.

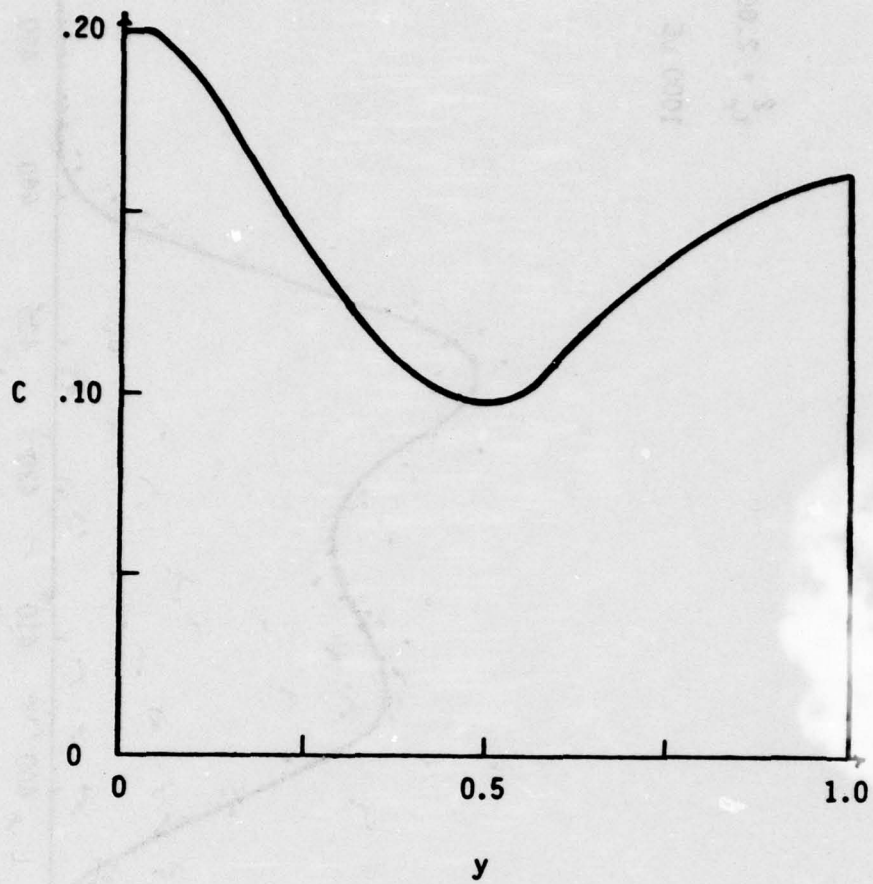


Figure B13: Assumed concentration profile
5 for sample S-5-3.

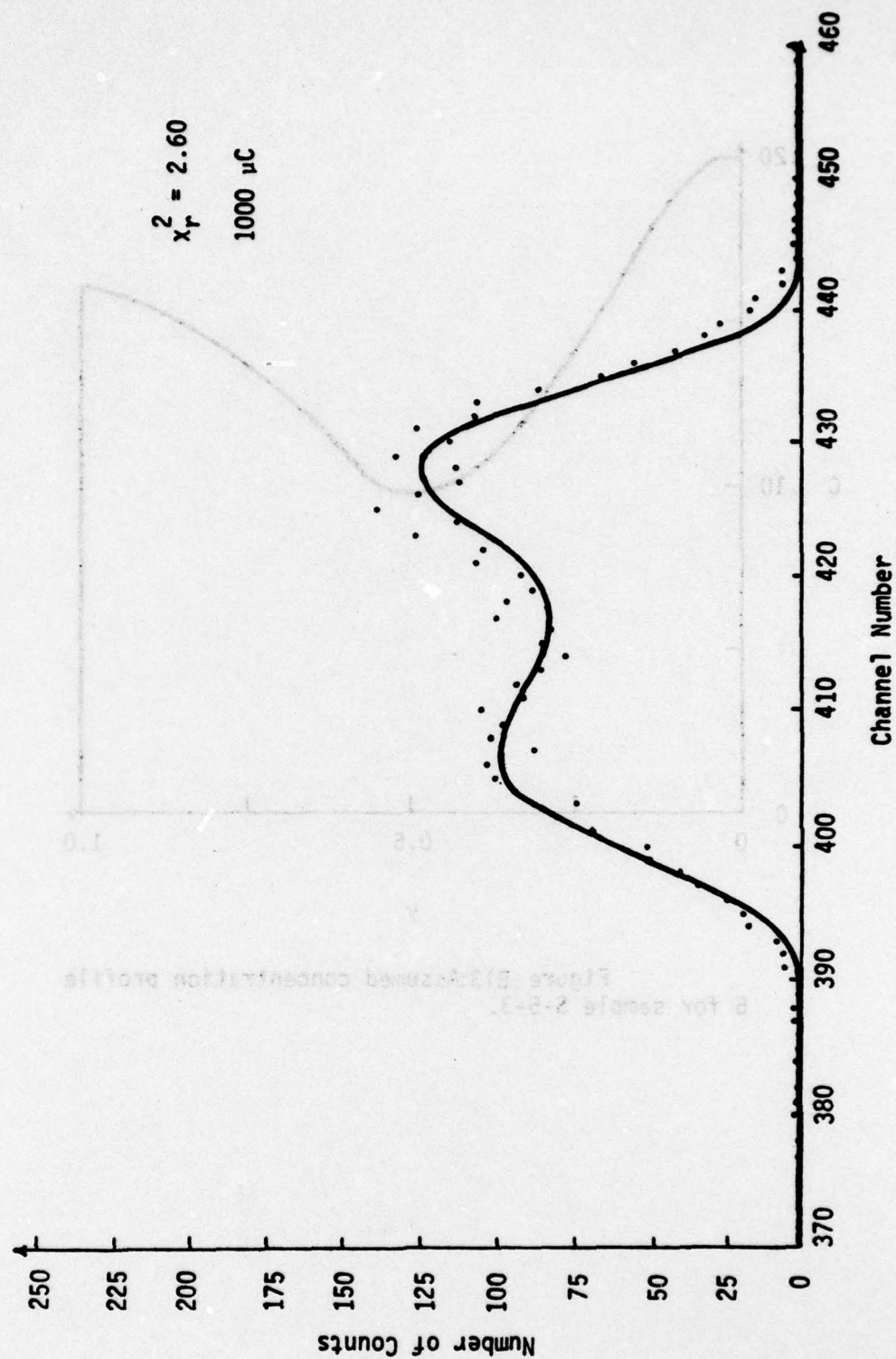


Figure B14: Comparison of experimental data with predicted spectra using assumed concentration profile 5 for sample S-5-3 at 750 KeV.

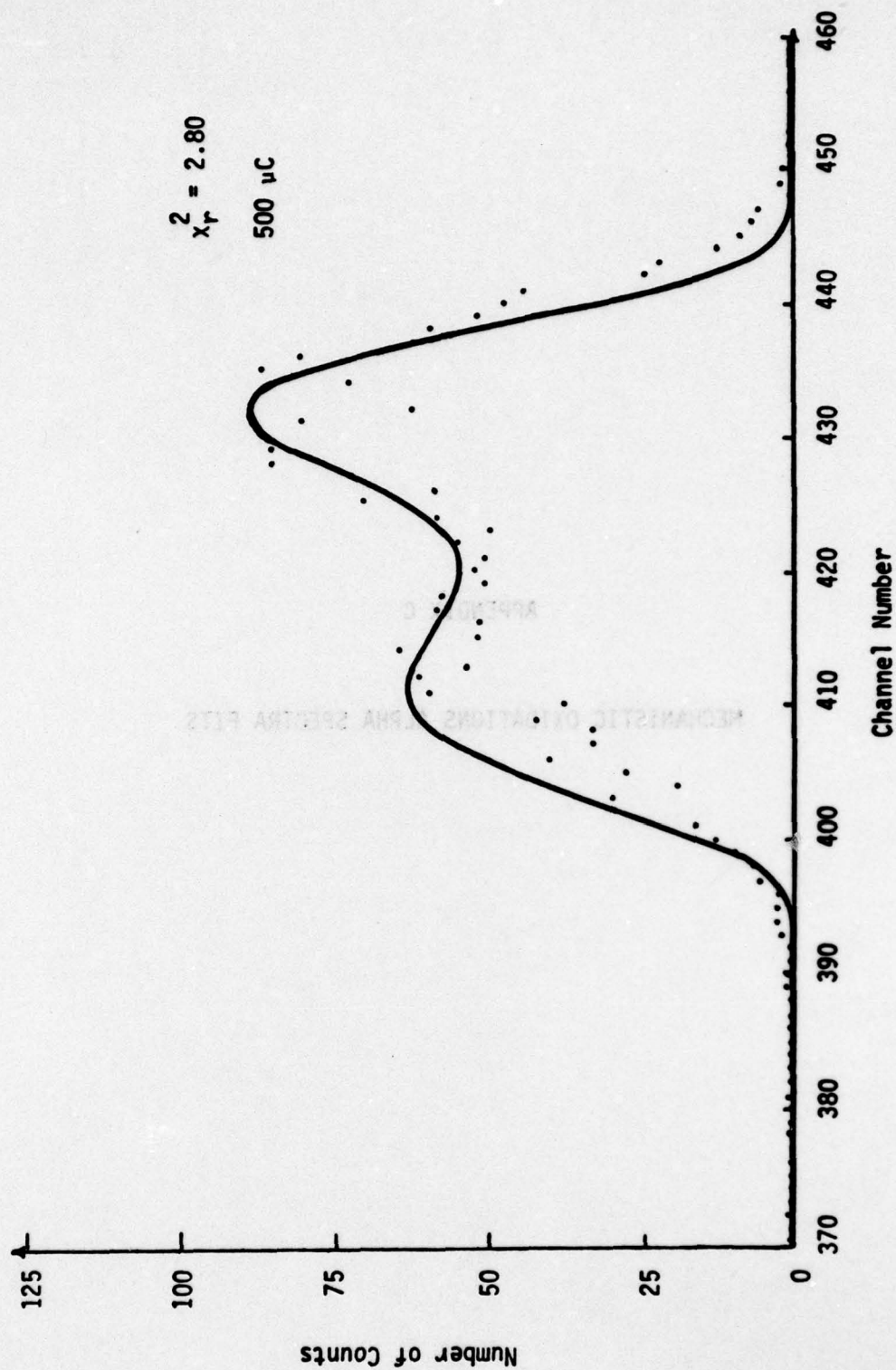
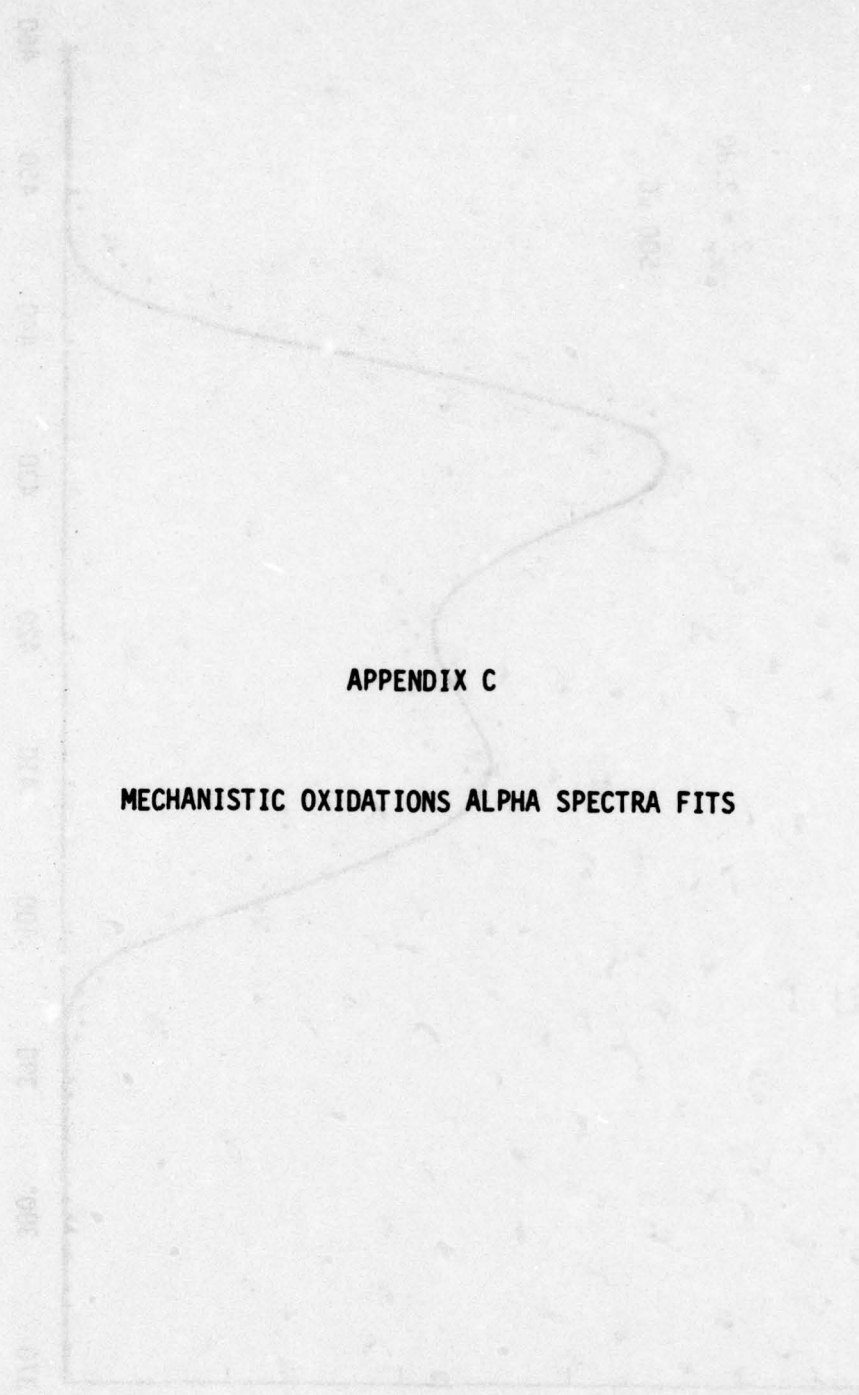


Figure B15: Comparison of experimental data with predicted spectra using assumed concentration profile 5 for sample S-5-3 at 800 KeV.

CONCENTRATION OF 10% 2000 2-2-2 AT 250 KPa
LARGE 112-CONCENTRATION OF 10% 2000 2-2-2 AT 250 KPa

Current (mA)



APPENDIX C

MECHANISTIC OXIDATIONS ALPHA SPECTRA FITS

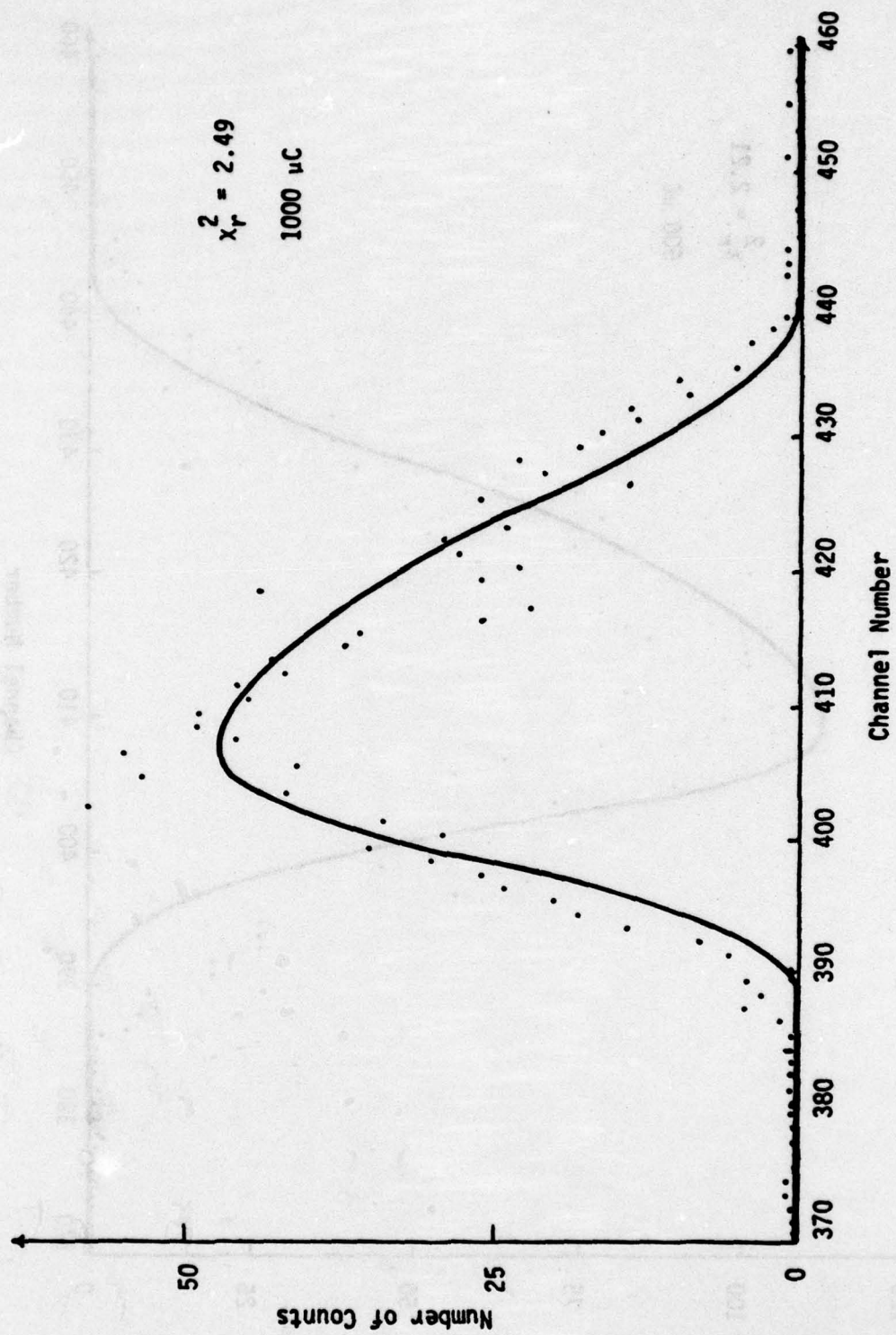


Figure C₁: Fit of Sample S-4-1 at an incident proton energy of 750 KeV.

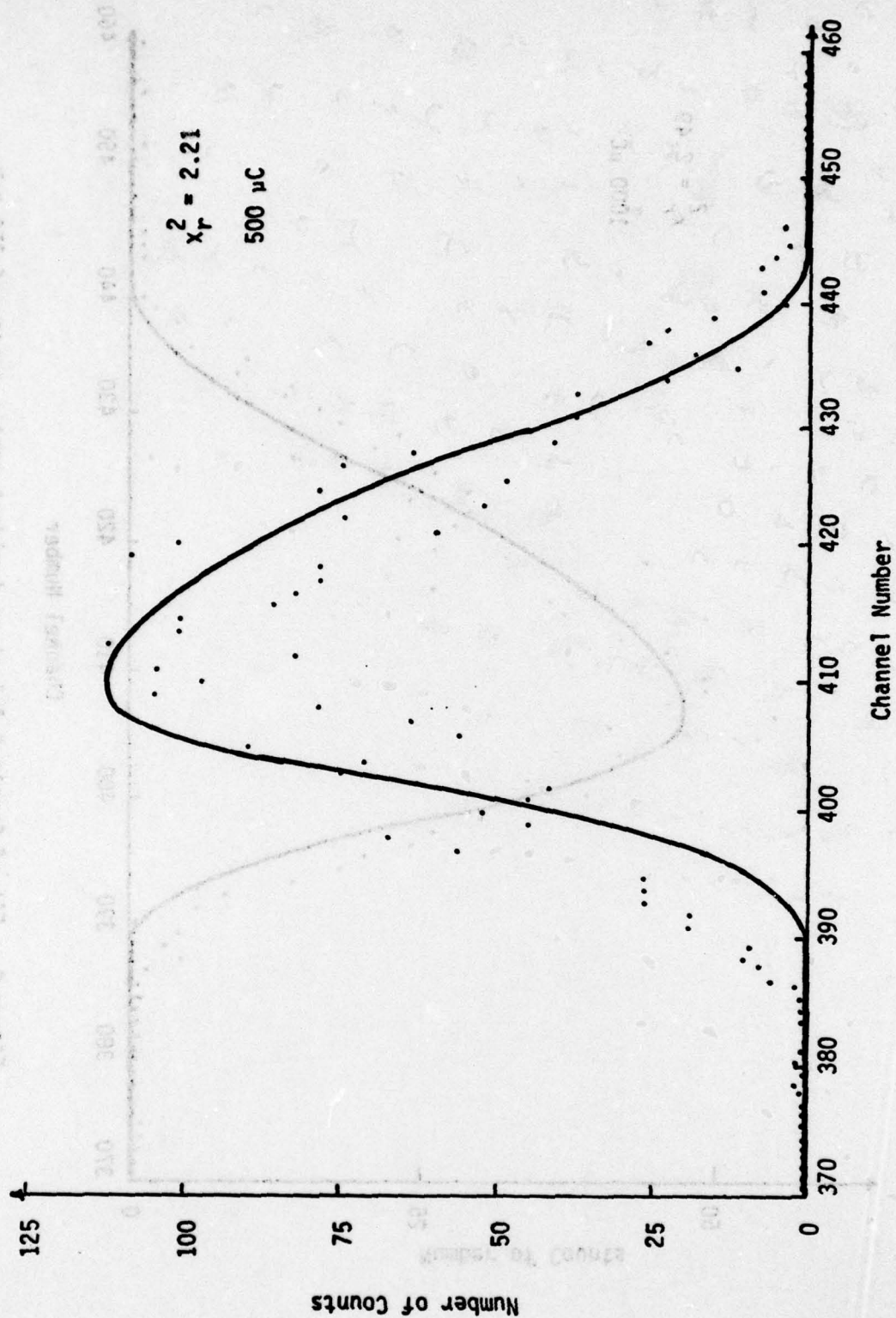


Figure C₂: Fit of Sample S-4-1 at an incident proton energy of 800 KeV.

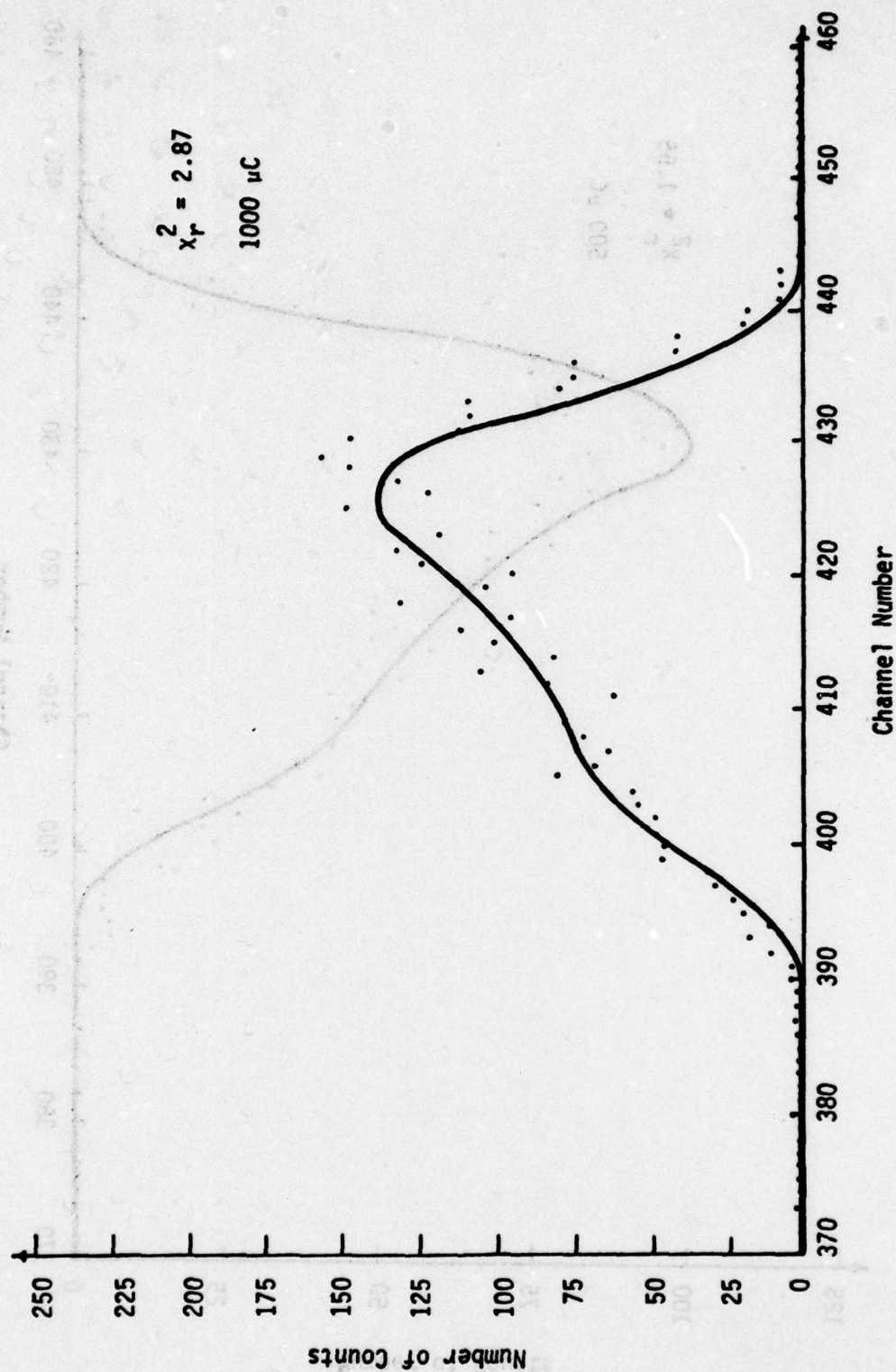


Figure C₃: Fit of Sample S-5-1 at an incident proton energy of 750 KeV.

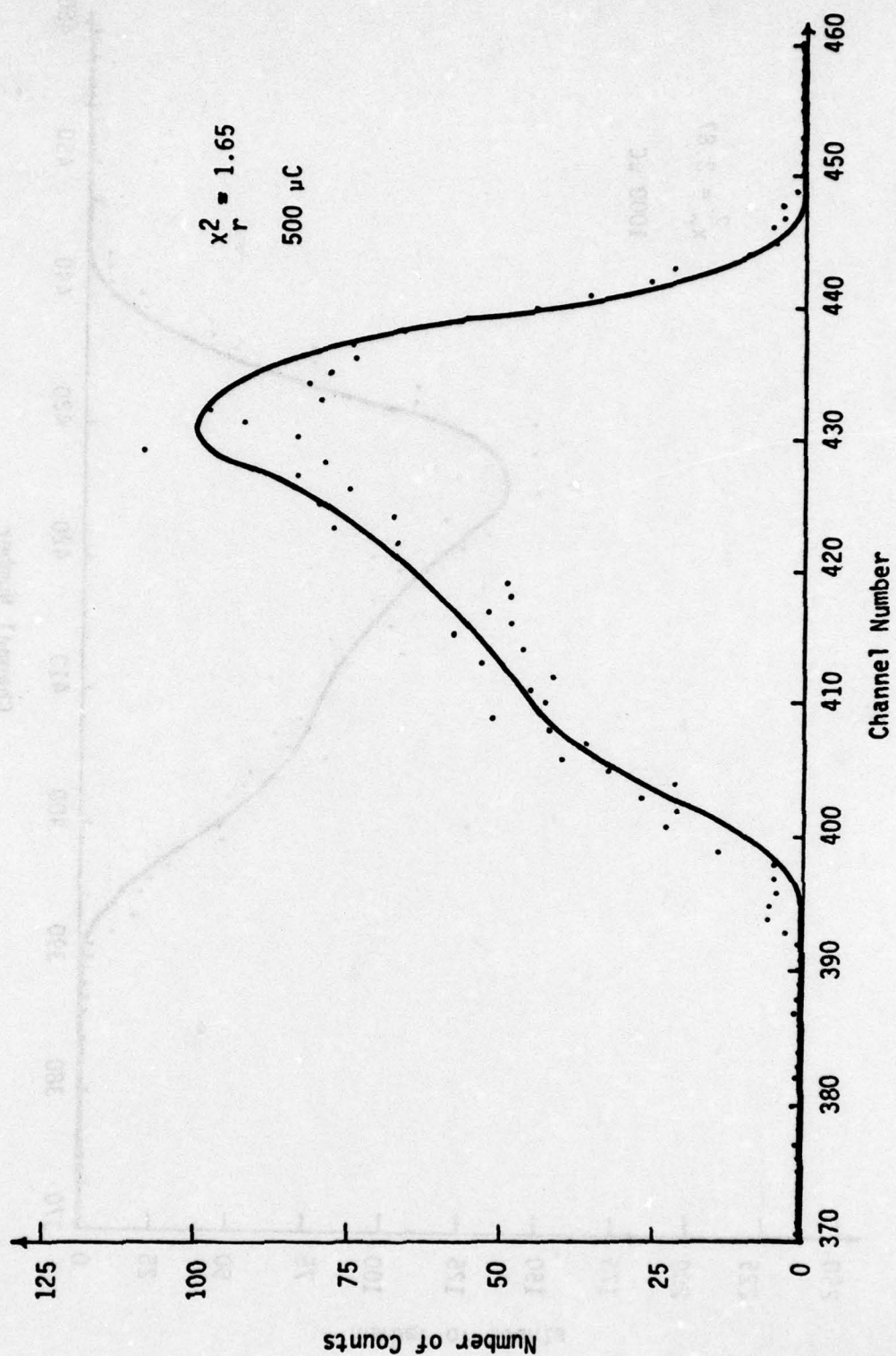


Figure C₄: Fit of Sample S-5-1 at an incident proton energy of 800 KeV.

REFERENCES

1. Robin, R.; Cooper, A. R. and Heuer, A. H.; Journal of Applied Physics, 44, 3770 (1973).
2. Uhlig, H. H.; Corrosion and Corrosion Control, John Wiley and Sons, Inc., New York (1971).
3. Grove, A. S.; Physics and Technology of Semiconductor Devices, John Wiley and Sons, Inc., New York (1971).
4. Deal, B. E. and Grove, A. S.; Journal of Applied Physics, 36, 3770 (1965).
5. Hauffe, K.; Oxidation of Metals, Plenum Press, New York (1965).
6. Kofstad, Per; Nonstoichiometry, Diffusion, and Electrical Conductivity in Binary Metal Oxides, Wiley-Interscience, New York (1972).
7. Wagner, C.; Atom Movements, American Society of Metals, Cleveland (1950).
8. Wagner, C.; High Temperature Properties of Metals, American Society of Metals, Cleveland (1950).
9. Wagner, C.; Journal of the Electrochemical Society, 99, 369 (1952).
10. Cabrera, N. and Mott, N. F.; Reports on Progress in Physics, 12, 163 (1948-49).
11. Mott, N. F.; Transaction of the Faraday Society, 43, 429 (1947).
12. Ghez, R.; The Journal of Chemical Physics, 58, 1838 (1973).
13. Jorgensen, P. J.; The Journal of Chemical Physics, 37, 874 (1962).
14. Research Triangle Institute; Integrated Silicon Device Technology, Volume VII, Oxidation; ASD-TDR-63-316 (1965).

15. Deal, B. E.; Journal of the Electrochemical Society, 110, 527 (1963).
16. Evitts, H. C.; Cooper, H. W. and Flaschen, S. S.; Journal of the Electrochemical Society, 111, 688 (1964).
17. Irene, E. A.; Journal of the Electrochemical Society, 121, 1613 (1974).
18. Atalla, M. M.; Semiconductor Surfaces and Films, Interscience Publishers, Inc., New York, Vol. V (1960).
19. Law, J. T.; Journal of Physical Chemistry, 61, 1200 (1957).
20. Williams, E. L.; Journal of the American Ceramic Society, 48, 190 (1965).
21. Norton, F. J.; Nature (London), 191, 701 (1961).
22. Ligenza, J. R. and Spitzer, W. G.; Journal of Physics and Chemistry of Solids, 14, 131 (1960).
23. Raleigh, D. O.; Journal of the Electrochemical Society, 113, 782 (1966).
24. Sucov, E. W.; Journal of the American Ceramic Society, 46, 14 (1963).
25. Schaeffer, H. A.; International Congress on Glass, Versailles (1971).
26. Meek, R. L.; Journal of the American Ceramic Society, 56, 341 (1973).
27. Doremus, R. H.; Glass Science, Wiley-Interscience, New York (1973).
28. Hutchison, D. A.; Journal of Physical Chemistry, 22, 758 (1954).
29. Condit, R. H. and Holt, J. B.; Journal of the Electrochemical Society, 111, 1192 (1964).
30. Chourhury, A.; Palmer, D. W.; Amsel, G.; Curien, H. and Baruch, P.; Solid State Communications, 3, 119 (1965).
31. Palmer, D. W.; Nuclear Instruments and Methods, 38, 187 (1965).
32. Calvert, J. M.; Lees, D. G.; Derry, D. J. and Barnes, D.; Journal of Radioanalytical Chemistry, 12, 271 (1972).

33. Hadari, Z.; Kroupp, M. and Wolfson, Y.; Journal of Applied Physics, 42, 534 (1971).
34. Gass, J. E.; Muller, H. H.; Schmied, H.; Jorissen, L. and Ziffermayer, G.; Nuclear Instruments and Methods, 106, 109 (1973).
35. Amsel, G.; Beranger, G.; deGelas, B. and Lacombe, P.; Journal of Applied Physics, 39, 2246 (1970).
36. Amsel, G. and Samuel, D.; Journal of Physics and Chemistry of Solids, 23, 1707 (1962).
37. Croset, M.; Peteanu, E.; Samuel, D.; Amsel, G. and Nadai, J. P.; Journal of the Electrochemical Society, 118, 717 (1971).
38. Siejka, J.; Nadai, J. P. and Amsel, G.; Journal of the Electrochemical Society, 118, 727 (1971).
39. Siejka, J.; Cherki, C. and Yahalom, J.; Journal of the Electrochemical Society, 119, 991 (1972).
40. Amsel, G.; Nadai, J. P.; D'Amrtemare, E.; David, D.; Girard, E. and Moulin, J.; Nuclear Instruments and Methods, 92, 481 (1971).
41. Whitton, J. L.; Mitchell, J. V. and Winterbon, K. B.; Canadian Journal of Physics, 49, 1225 (1971).
42. Neild, D. J.; Wise, P. J. and Barnes, D. G.; Journal of Physics D; Applied Physics, 5, 2292 (1972).
43. Turos, A.; Wielunski, L. and Jelinska, J.; Acta Physica Polonica, A43, 657 (1973).
44. Lindstrom, W. W. and Heuer, A. H.; Nuclear Instruments and Methods, 115, 1 (1974).
45. Evans, R. D.; The Atomic Nucleus, McGraw-Hill, New York (1955).
46. Smigelskas, A. D. and Kirkendall, E. O.; Transactions AIME, 171, 130 (1947).
47. Brown, F. and Mackintosh, W. D.; Journal of the Electrochemical Society, 120, 1096 (1973).
48. Pringle, J. P. S.; Journal of the Electrochemical Society, 120, 398 (1973).
49. Bardeen, J.; Brattain, W. H. and Shockley, W.; Journal of Chemical Physics, 14, 714 (1946).
50. Holt, J. B. and Himmel, L.; Journal of the Electrochemical Society, 116, 1569 (1969).

51. Shelby, J. and Mattern, P.; Fall Meeting, Glass Division,
American Ceramic Society, October 1974.
52. Morin, F.; Oxidation of Metals, 6, 65 (1973).
53. Bevington, P. P.; Data Reduction and Error Analysis for the
Physical Sciences, McGraw-Hill, New York (1969).
54. Pliskin, W. A. and Conrad, E. E.; IBM Journal, 43, (1964).
55. Williamson, C. F.; Boujot, J. P. and Picard, J.; CEA-R 3042
(1966).
56. Shewmon, P. G.; Diffusion in Solids, McGraw-Hill, New York
(1963).

BIBLIOGRAPHY

- Amsel, G.; Beranger, G.; DeGelas, B. and Lacombe, P.; Journal of Applied Physics, 39, 2246 (1970).
- Amsel, G.; Nadai, J. P.; D'Amrtemare, E.; David, D.; Girard, E. and Moulin, J.; Nuclear Instruments and Methods, 92, 481 (1971).
- Amsel, G. and Samuel, D.; Journal of Physics and Chemistry of Solids, 23, 1707 (1962).
- Atalla, M. M.; Semiconductor Surfaces and Films, Interscience Publishers, Inc., New York, Vol. V (1960).
- Bardeen, J.; Brattain, W. H. and Shockley, W.; Journal of Chemical Physics, 14, 714 (1946).
- Bevington, P. R.; Data Reduction and Error Analysis for the Physical Sciences, McGraw-Hill, New York (1969).
- Brown, F. and Mackintosh, W. D.; Journal of the Electrochemical Society, 120, 1096 (1973).
- Cabrera, N. and Mott, N. F.; Reports on Progress in Physics, 12, 163 (1948-49).
- Calvert, J. M.; Lees, D. G.; Derry, D. J. and Barnes, D.; Journal of Radioanalytical Chemistry, 12, 271 (1972).
- Chourhury, A.; Palmer, D. W.; Amsel, G.; Curien, H. and Baruch, P.; Solid State Communications, 3, 119 (1965).
- Condit, R. H. and Holt, J. B.; Journal of the Electrochemical Society, 111, 1192 (1964).
- Croset, M.; Peteanu, E.; Samuel, D.; Amsel, G. and Nadai, J. P.; Journal of the Electrochemical Society, 118, 717 (1971).
- Deal, B. E.; Journal of the Electrochemical Society, 111, 688 (1964).
- Deal, B. E. and Grove, A. S.; Journal of Applied Physics, 36, 3770 (1965).
- Doremus, R. H.; Glass Science, Wiley-Interscience, New York (1973).
- Evans, R. D.; The Atomic Nucleus, McGraw-Hill, New York (1955).
- Evitts, H. C.; Cooper, H. W. and Flaschen, S. S.; Journal of the Electrochemical Society, 111, 688 (1964).
- Gass, J. E.; Muller, H. H.; Schmied, H.; Jorissen, L. and Ziffermayer, G.; Nuclear Instruments and Methods, 106, 109 (1973).

- Ghez, R.; The Journal of Chemical Physics, 58, 1838 (1973).
- Grove, A. S.; Physics and Technology of Semiconductor Devices, John Wiley and Sons, Inc., New York (1971).
- Hadari, Z.; Kroupp, M. and Wolfson, Y.; Journal of Applied Physics, 42, 534 (1971).
- Hauffe, K.; Oxidation of Metals, Plenum Press, New York (1965).
- Holt, J. B. and Himmel, L.; Journal of the Electrochemical Society, 116, 1569 (1969).
- Hutchison, D. A.; Journal of Physical Chemistry, 22, 758 (1954).
- Irene, E. A.; Journal of the Electrochemical Society, 121, 1613 (1974).
- Jorgensen, P. J.; The Journal of Chemical Physics, 37, 874 (1962).
- Kofstad, Per; Nonstoichiometry, Diffusion, and Electrical Conductivity in Binary Metal Oxides, Wiley-Interscience, New York (1972).
- Law, J. T.; Journal of Physical Chemistry, 61, 1200 (1957).
- Ligenza, J. R. and Spitzer, W. G.; Journal of Physics and Chemistry of Solids, 14, 131 (1960).
- Lindstrom, W. W. and Heuer, A. H.; Nuclear Instruments and Methods, 115, 1 (1974).
- Meek, R. L.; Journal of the American Ceramic Society, 56, 341 (1973).
- Morin, F.; Oxidation of Metals, 6, 65 (1973).
- Mott, N. F.; Transaction of the Faraday Society, 43, 429 (1947).
- Neild, D. J.; Wise, P. J. and Barnes, D. G.; Journal of Physics D; Applied Physics, 5, 2292 (1972).
- Norton, F. J.; Nature (London), 191, 701 (1961).
- Palmer, D. W.; Nuclear Instruments and Methods, 38, 187 (1965).
- Pliskin, W. A. and Conrad, E. E.; IBM Journal, 43, (1964).
- Pringle, J. P. S.; Journal of the Electrochemical Society, 120, 398 (1973).
- Raleigh, D. O.; Journal of the Electrochemical Society, 113, 782 (1966).

Research Triangle Institute; Integrated Silicon Device Technology,
Volume VII, Oxidation; ASD-TDR-63-316 (1965).

Robin, R.; Cooper, A. R. and Heuer, A. H.; Journal of Applied
Physics, 44, 3770 (1973).

Schaeffer, H. A.; International Congress on Glass, Versailles (1971).

Shelby, J. and Mattern, P.; Fall Meeting, Glass Division, American
Ceramic Society, October 1974.

Shewmon, P. G.; Diffusion in Solids, McGraw-Hill, New York (1963).

Siejka, J.; Cherki, C. and Yahalom, J.; Journal of the Electrochemical
Society, 119, 991 (1972).

Siejka, J.; Nadai, J. P. and Amsel, G.; Journal of the Electrochemical
Society, 118, 727 (1971).

Smigelskas, A. D. and Kirkendall, E. O.; Transactions AIME, 171,
130 (1947).

Sucov, E. W.; Journal of the American Ceramic Society, 46, 14 (1963).

Turos, A.; Wielunski, L. and Jelinska, J.; Acta Physica Polonica, A43,
657 (1973).

Uhlig, H. H.; Corrosion and Corrosion Control, John Wiley and Sons, Inc.,
New York (1971).

Wagner, C.; Atom Movements, American Society of Metals, Cleveland (1950).

Wagner, C.; High Temperature Properties of Metals, American Society of
Metals, Cleveland (1950).

Wagner, C.; Journal of the Electrochemical Society, 99, 369 (1952).

Whitton, J. L.; Mitchell, J. V. and Winterbon, K. B.; Canadian Journal
of Physics, 49, 1225 (1971).

Williams, E. L.; Journal of the American Ceramic Society, 48, 190
(1965).

Williamson, C. F.; Boujot, J. P. and Picard, J.; CEA-R 3042 (1966).